



NTNU – Trondheim
Norwegian University of
Science and Technology

Use of CFD to Study Hydrodynamic Loads on Free-Fall Lifeboats in the Impact Phase.

A verification and validation study.

Stian Ripegutuh Johannessen

Marine Technology

Submission date: June 2012

Supervisor: Sverre Steen, IMT

Co-supervisor: Hans Jørgen Bjelke-Mørch, CFD Marin

Norwegian University of Science and Technology
Department of Marine Technology

ABSTRACT

In the past, testing of lifeboat design has been carried out solely by experimental means. However, due to the large number of factors which influence the loads on the lifeboat structure and its occupants, optimization studies by experimental means have become both time-consuming and expensive. In addition, many effects cannot be studied at laboratory scale due to the inability to match all similarity requirements.

Recent advances in computational fluid dynamics (CFD) have made it possible to analyze the lifeboats performance under realistic conditions. By not being dependent on a physical model, investigation of a larger range of hull shapes at a variety of launch conditions can be done more easily and cost-efficient.

This thesis explores the possibility of using the CD-adapco's CFD-software STAR-CCM+ (STAR) to predict the performance of free-fall lifeboats during the impact phase. The thesis focuses on verification and validation of the software by studying water impact of different two and three-dimensional rigid and elastic wedges.

For the two-dimensional case, 2-D rigid wedges with constant vertical velocity and varying deadrise angles (4 to 81 degrees) are studied with respect to various slamming parameters presented by Zhao and Faltinsen (1992). In the study, good agreement is found between the solution predicted in STAR and the presented numerical and analytical solutions. It is found that the slamming pressures are strongly dependent on the deadrise angle; from 300 Pa for the 81° wedge, to 275 000 Pa for the 4° wedge. It is seen that as the deadrise angle is decreased, better resolution in grid size and time step is required to capture the peak pressures.

The three-dimensional case includes both rigid and elastic wedges. For the rigid case, a 3-D wedge is modeled so to represent an experimental study conducted by Yettou et al. (2006). It is found that STAR predicts a lower impact velocity than what is found in the experimental study. Following, the pressures predicted are too low. The difference is however moderate, and STAR is able to predict the displacement and velocity-time histories of the wedge in a satisfactory manner. It is noted that the reason for the discrepancy lies in the prediction of motion through air - and not in the simulation of impact and motion in water. It is also noted that refinements in grid size and time step are not of great importance if only displacements and velocities are to be studied.

For the elastic wedge case, four different elastic wedges are studied to explore STAR's possibilities and limitations related to fluid-structure interaction (FSI). No verification or validation with existing theory or experimental data is performed. A qualitative assessment of the results is however carried out and it is found that STAR predicts displacements, velocities, accelerations, pressures, deflections and stresses in a satisfactory manner.

SAMMENDRAG

Tidligere har testing av frittfall-livbåt design blitt utført utelukkende ved bruk av eksperimentelle metoder. Optimaliseringsstudier på livbåt er imidlertid tidkrevende og dyrt grunnet de rekke faktorene som påvirker livbåtens prestasjoner. I tillegg er det mange effekter som ikke lar seg studere i laboratorieskala grunnet manglende evne til matche de ulike likhetskravene.

Nylige fremskritt innen Computational Fluid Dynamics (CFD) har gjort det mulig å analysere livbåtens prestasjoner under realistiske forhold. Ved å ikke være avhengig av en fysisk modell kan dermed en rekke ulike design av både livbåt og sliskesystem testes enklere og mer kostnadseffektivt.

Denne oppgaven utforsker bruken av CD-adapcos CFD-programvare STAR-CCM+ (STAR) til å forutsi prestasjonen til livbåter i fritt fall og ved "water impact". Opgaven fokuserer på verifikasjon av programvaren ved å studere ulike to- og tredimensjonale stive og elastisk kiler.

I det to-dimensjonale tilfellet studeres 2-D kiler med konstant vertikal hastighet og varierende angrepsvinkler (4 til 81 grader). Ulike parametere presentert av Zhao and Faltinsen (1992) benyttes for å verifisere løsningen. I studiet er det funnet godt samsvar mellom løsningen i STAR og løsningen fra de presenterte numeriske og analytiske metodene. Det er vist at slammingtrykket er sterkt avhengig av angrepsvinkel; fra 300 Pa for 81° kile, til 275 000 Pa for 4° kile. Videre er det funnet at man ved lavere angrepsvinkler må øke oppløsningen i grid og tidsskritt for å fange de høye trykktoppene.

Det tredimensjonale studiet omfatter både stive og elastisk kiler. I det stive tilfellet er en 3-D kile modellert for å gjenskape det eksperimentelle studiet utført av Yettou et al. (2006). Det er funnet at STAR gir lavere nedslagshastighet enn det som er funnet i den eksperimentelle studien, noe som igjen fører til at trykkfordelingen funnet i STAR blir for lav. Forskjellen er imidlertid moderat, og man kan konkludere med at STAR er i stand til forutsi bevegelsen og hastigheten til kilen på en tilfredsstillende måte. Det bemerkes at årsaken til avviket ligger i løsningen av bevegelse gjennom luften, og ikke i simulering av nedslaget og bevegelsen i vann. Det skal også bemerkes at oppløsningen av grid og tidsskritt er av liten betydning om kun bevegelse og hastighet er av interesse.

I det elastiske tilfellet er fire forskjellige elastiske kiler modellert for utforske STAR sine muligheter og begrensninger knyttet til fluid-struktur interaksjon (FSI). Ingen verifikasjon eller validering med eksisterende teori eller eksperimentelle data er utført. En kvalitativ vurdering av resultatene er imidlertid blitt gjort og det er funnet at STAR løser bevegelser, hastigheter, akselerasjoner, trykk, utbøyning og spenninger på en tilfredsstillende måte.

PREFACE

This thesis is a result of the individual work required for fulfillment of the degree Master of Science, Marine Hydrodynamics.

The thesis has been performed partly at CDF Marine, Tvedestrand, and partly at the Norwegian University of Science and Technology (NTNU), Department of Marine Technology, Trondheim.

The work is conducted with Professor Sverre Steen (NTNU) as supervisor and Hans Jørgen Bjelke-Mørch (CDF Marine) as advisor.

SCOPE OF WORK



NTNU Trondheim
Norwegian University of Science and Technology
Department of Marine Technology

MASTER THESIS IN MARINE TECHNOLOGY

SPRING 2012

FOR

Stian R. Johannessen

Use of CFD to study hydrodynamics loads on free-fall lifeboats in the impact-phase

During recent years there has been an intensive research in the performance of free-fall lifeboats, after full scale tests offshore revealed several safety-related issues, such as structural problems, extremely high acceleration levels during the impact phase, and insufficient capability to move away from the platform after launching. This work shall focus on the forces and motions of the lifeboat during the impact phase, which means from it first touches the water until it has finally reappeared on the surface and the motions induced by the impact have practically disappeared.

Current designs for free-fall lifeboats are characterized by severe limitations on weight, length and draught of the boats, leading to very full hull forms with blunt bows.

The aim of the master thesis is to:

- Explore the use of Star CCM+ to predict the performance of free-fall lifeboats during the impact phase.

It is recommended that the following topics shall be covered in the master thesis:

- Refine and improve the simulation of the 2-D wedge in order to verify the CFD simulations and select proper discretization in time and space.
- Advance the correlation study by also considering impact of a 3-D wedge
- Study the effect of fluid-structure interaction for a wedge, using CFD.
- Give recommendations for how CFD can be used to evaluate the performance of different free-fall lifeboat designs.

In the thesis the candidate shall present his personal contribution to the resolution of problem within the scope of the thesis work.

Theories and conclusions should be based on mathematical derivations and/or logic reasoning identifying the various steps in the deduction.

The candidate should utilize the existing possibilities for obtaining relevant literature.



NTNU Trondheim
Norwegian University of Science and Technology
Department of Marine Technology

The thesis should be organized in a rational manner to give a clear exposition of results, assessments, and conclusions. The text should be brief and to the point, with a clear language. Telegraphic language should be avoided.

The thesis shall contain the following elements: A text defining the scope, preface, list of contents, summary, main body of thesis, conclusions with recommendations for further work, list of symbols and acronyms, reference and (optional) appendices. All figures, tables and equations shall be numerated.

The supervisor may require that the candidate, in an early stage of the work, present a written plan for the completion of the work. The plan should include a budget for the use of computer and laboratory resources that will be charged to the department. Overruns shall be reported to the supervisor.

The original contribution of the candidate and material taken from other sources shall be clearly defined. Work from other sources shall be properly referenced using an acknowledged referencing system.

The thesis shall be submitted in two copies:

- Signed by the candidate
- The text defining the scope included
- In bound volume(s)
- Drawings and/or computer prints that cannot be bound should be organized in a separate folder.
- The bound volume shall be accompanied by a CD or DVD containing the written thesis in Word or PDF format. In case computer programs have been made as part of the thesis work, the source code shall be included. In case of experimental work, the experimental results shall be included in a suitable electronic format.

Supervisor : Professor Sverre Steen
Advisors : Hans Jørgen Bjelke-Mørch (CFD Marine)
Start : 16.01.2012
Deadline : 10.06.2012

Trondheim, 13.01.2012

Sverre Steen

ACKNOWLEDGMENTS

This thesis is a result of my work carried out in the Spring of 2012, January 16th to June 10th, required by the Norwegian University of Science and Technology in accordance with the 5th year in the Master in Marine Technology, specialization Hydrodynamics.

When I first undertook the task of this master thesis, I had no idea how many people would eventually contribute their time and talents. I am grateful to all of you, but I am especially grateful to those who went that extra step in offering their skills and expertise.

I would like to thank the people in CD-adapco, and especially Sven Enger for making the trip to CD-adapco's office in Nuremberg possible. Also, much gratitude is given to Christian Bodmer for answering all my questions regarding the STAR-CCM+ software.

In CD-adapco I will also like to thank Alan Mueller and Oleg Voronkov for guiding me through the use of STAR-CCM+ for Fluid-Structure Interaction studies.

To Milovan Peric, in CD-adapco, who has guided me throughout much of this thesis. In late and early hours, you have always answered my questions and provided me with the valuable information I have needed to push forward. Your experience in your field and dedication for my work has truly been an inspiration.

Special thanks goes to Hans Jørgen Bjelke-Mørch in CFD Marine, who has made the study in this thesis possible by allowing me access to his computer cluster and contributing with his enormous insight in experimental and numerical techniques. Without your guidance and expertise I would have been lost.

A second special thanks is given to Thomas Larsen, also in CFD Marine, who through numerous conversations has given me valuable insight in computational fluid dynamics and the use of STAR-CMM+. Your inspiration and efforts in helping me has truly made the difference.

Lastly, I would like to express a deep gratitude to my supervisor, Prof. Sverre Steen, who throughout my last two semesters has guided me, keeping my mind on the given task and pointing me in the right direction.

To my loved ones.

Your care and encouragement means the world.



Stian R. JOHANNESSEN
Trondheim, June 10th, 2012

Contents

ABSTRACT	iii
SAMMENDRAG	iv
PREFACE	vi
SCOPE OF WORK	viii
ACKNOWLEDGMENTS	xi
List of Figures	xiv
List of Tables	xvii
List of Symbols	xviii
List of Abbreviations	xxi
1 INTRODUCTION AND MOTIVATION	1
2 COMPUTATIONAL FLUID DYNAMICS (CFD)	3
2.1 INTRODUCTION TO CFD	4
THE CFD PROCESS	4
PRACTICAL ISSUES	7
2.2 STAR-CCM+	9
SOLUTION METHOD	10
MODELING	12
BOUNDARY CONDITIONS	13
MESH	14
PHYSICS	15
SOLVERS	17
POST PROCESSING	19
3 WATER ENTRY OF TWO-DIMENSIONAL WEDGES	21
3.1 SOLUTIONS USED FOR COMPARISON	22
BOUNDARY ELEMENT METHOD	22
SIMILARITY SOLUTION	23
ASYMPTOTIC SOLUTION	24
3.2 SOLUTION IN STAR-CCM+	25
DISCRETIZATION OF TIME AND SPACE	25
LAMINAR VERSUS TURBULENT FLOW	31

	INFLUENCE OF NUMERICAL PARAMETERS	32
	ANALYZING AND POST PROCESSING	33
3.3	RESULTS	36
4	WATER ENTRY OF A THREE-DIMENSIONAL WEDGE	45
4.1	DESCRIPTION OF THE EXPERIMENT	46
	SET-UP	46
	INSTRUMENTATION AND DATA ACQUISITION	46
4.2	SOLUTION IN STAR-CCM+	50
	MODELING	50
	DISCRETIZATION OF TIME AND SPACE	52
	LAMINAR VERSUS TURBULENT FLOW	56
	INFLUENCE OF NUMERICAL PARAMETERS	58
4.3	RESULTS	61
	RAW DATA ANALYZES	61
	NON-DIMENSIONAL STUDY	66
5	HYDROELASTIC IMPACT OF THREE-DIMENSIONAL WEDGES	71
5.1	FLUID-STRUCTURE INTERACTION IN STAR-CCM+	73
	FSI COUPLING	73
	MESH EVOLUTION	74
	FINITE VOLUME STRESS	74
	COMPRESSIBLE FLUID	75
5.2	SOLUTION IN STAR-CCM+	76
	MODELING	76
	DISCRETIZATION OF TIME AND SPACE	78
	CHOICE OF NUMERICAL PARAMETERS	80
	COMPRESSIBLE VERSUS INCOMPRESSIBLE FLUID	80
5.3	RESULTS	86
	RAW DATA ANALYZES	86
6	CONCLUSIONS	93
6.1	WATER ENTRY OF TWO-DIMENSIONAL WEDGES	93
6.2	WATER ENTRY OF A THREE-DIMENSIONAL WEDGE	93
6.3	HYDROELASTIC IMPACT OF THREE-DIMENSIONAL WEDGES	94
6.4	SUGGESTIONS FOR FURTHER STUDY	94
7	RECOMMENDATIONS FOR FURTHER WORK: LIFEBOAT WATER ENTRY	95
7.1	MODELING AND MESHING	95
7.2	PHYSICAL MODELS AND INITIAL CONDITIONS	96
7.3	SOLVER PARAMETERS AND SETTINGS	97
7.4	MISCELLANEOUS	98
	References	I

List of Figures

2.1	The pressure distribution around a ship hull.	4
2.2	Stages in CFD.	6
2.3	Workflow overview in STAR.	9
2.4	Flow chart of the iterative solution method for a coupled simulation. . .	12
2.5	A modeled half-wedge.	13
2.6	The trimmer meshing model applied on the modeled half-wedge.	15
2.7	Physics models to be chosen when studying water entry of a rigid wedge. .	16
2.8	Water rise-up at the half-wedge.	17
3.1	Definitions of coordinate system and control surfaces.	22
3.2	The medium size domain.	26
3.3	The effect of domain size on the total vertical hydrodynamic force. . . .	27
3.4	The effect of domain size on the pressure distribution along the wedge. .	28
3.5	A section of Grid 3 illustrating choice of local refinements and grid size.	28
3.6	The effect of grid size on the total vertical hydrodynamic force.	30
3.7	The effect of grid size on the pressure distribution along the wedge. . . .	30
3.8	The effect of choice of flow model on the pressure distribution.	31
3.9	Visualization of the water rise-up along the wedge section.	33
3.10	Pressure distribution and normalized pressure distribution along the wedge.	34
3.11	Visualization and plot of the velocity distribution along the wedge. . . .	34
3.12	Visualization and plot of the CFL-values along the wedge.	34
3.13	Total vertical hydrodynamic force on the wedge.	35
3.14	The residuals of water, continuity and x, y and z-momentum.	35
3.15	The free surface at $t = 0.06$ s after wedge impact.	36
3.16	Definition of parameters characterizing slamming pressure.	37
3.17	Pressure and normalized pressure distribution for the 4° wedge.	39
3.18	Pressure and normalized pressure distribution for the 7.5° wedge.	39
3.19	Pressure and normalized pressure distribution for the 10° wedge.	39
3.20	Pressure and normalized pressure distribution for the 15° wedge.	40
3.21	Pressure and normalized pressure distribution for the 20° wedge.	40
3.22	Pressure and normalized pressure distribution for the 25° wedge.	40
3.23	Pressure and normalized pressure distribution for the 30° wedge.	41
3.24	Pressure and normalized pressure distribution for the 40° wedge.	41
3.25	Pressure and normalized pressure distribution for the 45° wedge.	42
3.26	Pressure and normalized pressure distribution for the 60° wedge.	42
3.27	Pressure and normalized pressure distribution for the 81° wedge.	43
4.1	Diagram of the experimental set-up.	47
4.2	Image of the experimental set-up installed in the water channel.	48
4.3	Position of the twelve transducers along the wedge's median.	49

4.4	The symmetric conditions applied when modeling the geometry in STAR.	51
4.5	Front view of the quarter wedge and water basin modeled in STAR. . .	51
4.6	Top view of the quarter wedge and water basin modeled in STAR. . . .	52
4.7	Time history for the maximum pressure and averaged pressure.	52
4.8	The effect of grid size on the transducer geometry.	54
4.9	The effect of grid size on the maximum and averaged pressure.	55
4.10	The effect of grid size on the pressure coefficients.	55
4.11	The effect of time step on the maximum and averaged pressure.	56
4.12	The effect of time step on the pressure coefficients.	57
4.13	The effect of choice of flow model on the maximum and averaged pressure.	58
4.14	The effect of choice of flow model on the pressure coefficients.	59
4.15	The free surface mid-way through the simulation.	61
4.16	The wedge's displacement recorded by Yettou et al. (2006).	62
4.17	The wedge's velocity recorded by Yettou et al. (2006).	62
4.18	Pressure time variation for all 12 transducers for one drop.	64
4.19	The time variation of the peak pressures and quadratic velocities.	65
4.20	Comparison of deceleration data.	66
4.21	The parameters describing the impact of the wedge in water.	66
4.22	Comparison of the pressure coefficients at $t = 9.8$ ms after impact. . . .	69
4.23	Comparison of the pressure coefficients at $t = 17.6$ ms after impact. . .	69
4.24	Comparison of the pressure coefficients at $t = 22.8$ ms after impact. . .	70
5.1	The geometry for the wedge made of GRP modeled in STAR.	77
5.2	Front view of GRP wedge and water and air domain.	77
5.3	The grid used in the FSI study	79
5.4	Location of pressure probe and measured deflection in the FSI study. . .	82
5.5	The wedge displacement in a comp. and incomp. environment.	83
5.6	The wedge velocity in a comp. and incomp. environment.	83
5.7	The wedge acceleration in a comp. and incomp. environment.	84
5.8	The pressure predicted in a comp. and incomp. environment.	84
5.9	The deflection predicted in a comp. and incomp. environment.	85
5.10	The 4 mm thick steel wedge at $t = 0.8$ s after water impact.	86
5.11	The displacement predicted in STAR for the four different elastic wedges.	89
5.12	The velocity predicted in STAR for the four different elastic wedges. . .	89
5.13	The accelerations predicted in STAR for the four different elastic wedges.	90
5.14	The effect of air resistance on the wedge acceleration.	90
5.15	The pressure predicted in STAR for the four different elastic wedges. . .	91
5.16	The deflection predicted in STAR for the four wedges.	91
5.17	The von Mises stresses predicted in STAR for the four wedges.	92

List of Tables

2.1	The process of obtaining useful information about fluid motion problems.	5
3.1	The three different domains used in the domain size analysis.	26
3.2	The effect of domain size on the different slamming parameters.	27
3.3	The four different grids used in the grid size analysis.	29
3.4	The effect of grid size on the different slamming parameters.	29
3.5	The effect of choice of flow model on the different slamming parameters.	31
3.6	Parameters tested in the convergence study.	32
3.7	Estimation of slamming parameters by STAR.	37
3.8	Estimation of slamming parameters by the investigated solutions.	38
4.1	The domain used in the three-dimensional water entry study.	53
4.2	The four different grids used in the grid size analysis.	53
4.3	The effect of grid size on the maximum pressure and the averaged pressure.	54
4.4	The effect of time step on the maximum and averaged pressure.	56
4.5	The effect of choice of flow model on the maximum and averaged pressure.	58
4.6	Parameters tested in the convergence study.	60
4.7	Comparison of pressures from the experiment and STAR.	63
4.8	C_p and Z for the maximum and averaged pressure.	68
5.1	Properties of the four wedges modeled in the FSI study.	77
5.2	The domain used in the FSI study	78
5.3	The four different grids used in the grid size analysis.	80
5.4	Parameters chosen in the simulations for the FSI study.	81
5.5	The different properties defined in STAR to achieve compressibility. . .	81
5.6	Maximum values of displacement, velocity, acceleration, slamming pressure, deflection and Von Mises stresses for the four different elastic wedges.	87

List of Symbols

Greek

Γ	: diffusivity coefficient
Ω	: fluid domain
α	: deadrise angle
δ	: water jet thickness
ζ, η	: coordinates of points on the surface domain
μ	: viscosity
ρ_w	: mass density of water.
ρ_a	: mass density of air.
ϕ	: velocity potential
ϕ	: scalar variable (k , ε or ω)
ω_B	: angular velocity of the body's center of mass
ω_p	: under-relaxation factor for pressure
ω_u	: under-relaxation factor for velocity

Latin

A	: a $n \times n$ -matrix
a_p^V	: vector of central coefficients for the discretized linear system representing the velocity equation
b	: vector of body forces per unit mass
b_ϕ	: sources and sinks of ϕ
$C_{p_{ave}}$: pressure coefficient at averaged pressure
$C_{p_{max}}$: pressure coefficient at maximum pressure
c	: speed of sound
$c(t)$: wetted length
F_3	: total vertical hydrodynamic force
F_B	: force acting on the body
g	: gravity
I	: unit tensor
I_C	: moment of inertia of the body's center of mass

\mathbf{M}_C	: moment acting on the body
\dot{m}_f^*	: uncorrected mass fluxes
m_B	: the body mass
\mathbf{n}	: unit vector normal to the CV surface
\vec{n}	: normal vector of the surface S enclosing the domain
o	: volume fraction
$\nabla p'$: gradient of the pressure corrections
p	: pressure.
p_0	: atmospheric pressure
p_{ave}	: averaged pressure
p'_b	: pressure correction
p_{in}	: pressure in inner flow domain
p_{max}	: maximum pressure
p_{out}	: pressure in outer flow domain
\mathbf{r}	: position vector relative to a fixed reference frame
ΔS_s	: spatial extent of slamming pressure exceeding 50% of maximum pressure p_{max}
S	: surface enclosing the domain
s	: second
T	: stress tensor
T	: temperature
Δt	: time step
t	: time
U	: incoming velocity on a flat plate
u, v, w	: fluid velocities in direction x, y and z
V	: volume
V	: vertical velocity of the wedge
\mathbf{v}	: fluid velocity vector
\mathbf{v}^*	: intermediate velocity field
\mathbf{v}_b	: velocity of the CV surface
\mathbf{v}_C	: velocity of the body's center of mass
$\Delta x, \Delta y, \Delta z$: grid size in x, y and z-direction
y^+	: non-dimensional wall distance
Z	: dimensionless water entry depth
z_{max}	: z-coordinate of maximum pressure

List of Abbreviations

2-D	: Two-Dimensional
3-D	: Three-Dimensional
BEM	: Boundary Element Method
CAD	: Computer Aided Design
CAE	: Computer Aided Engineering
CAR	: Combined Acceleration Ratio
CFD	: Computational Fluid Dynamics
CFL	: Courant-Friedrichs-Levi
COG	: Center Of Gravity
CSE	: Co-Simulation Engine
CV	: Control Volume
DFBI	: Dynamic Fluid Body Interaction
DOF	: Degree Of Freedom
FS	: Finite Stress
FSI	: Fluid-Structure Interaction
FV	: Finite Volume
GRP	: Glass Reinforced Plastic
LES	: Large Eddy Simulation
MDRT	: Mesh Displacement in Real Time
MII	: Maximum Inner iterations
OLF	: Norwegian Oil Industry Association
PDE	: Partial Differential Equation
RANS	: Reynolds-Averaged Navier-Stokes
RST	: Reynold Stress Transport
SIMPLE	: Semi-Implicit Method for Pressure Linked Equations
STAR	: STAR-CCM+
URF	: Under-Relaxation Factor
USH	: Umoe Schat-Harding
VOF	: Volume Of Fluid

INTRODUCTION AND MOTIVATION

Free fall lifeboats are important for the safety of the passengers and crew of floating vessel and offshore platforms. The lifeboat needs to be designed such to efficiently evacuate the people on board in a safe manner. This implies that the lifeboat is not to be damaged during water entry and that the lifeboat will move sufficiently far away from its host structure after launch. It also sets requirements to the accelerations experienced by the occupants, as these can exert injury upon the occupant if experienced too large.

Offshore installation tests in spring 2005 revealed unacceptable structural deflection of roof and canopy on one of Umoe Schat-Harding's (USH) FF1000S at "Veslefrikkfeltet" which caused immediate actions to be initiated by the Norwegian Oil Industry Association (OLF). Their main goal was to study and document main performance factors for free fall lifeboats and following develop relevant criteria for in depth classification of performance. From this there were discovered structural weaknesses in the roof of several of the lifeboats used on the Norwegian shelf. In addition, the lifeboats ability to move away from the platform after water entry and the accelerations imposed on the passengers, became questioned. Through 2005-2009 a total of 250 lifeboats (16 different types) went through approval testing and documentation. All lifeboats which did not meet the requirements set, were re-built with new structural strength. In addition, implementation of weather dependent operational restrictions due to acceleration load protection and forward speed/distance limitations were carried out. In late 2009 OLF, Employee's Organization, Oil Companies and Authorities agreed upon the documentation standards and safety levels of the free fall lifeboats. OLF (2010)

From the development of the first free fall lifeboat in 1978, there has been an ongoing research directed to improvement of the free fall rescue system, both the lifeboat and the launching method. In the mission to optimize the lifeboat design and functionality, several new lifeboats have been developed, varying both in hull form and capacity.

For a free fall lifeboat, the most important properties are its structural strength, accelerations at water impact and forward motion after re-surfacing. These features are determined by a collection of parameters, such as length, beam, bow and cross-sectional shape (to mention a few) and will each have their impacts on the qualities of the free fall lifeboat system. Most of the different parameters are highly dependent on each other and must, by the designer, be combined with stringent limitations if the final design is to fulfill the main functional requirements for the lifeboat and launching system. As a minor change in one parameter may have significant impact on more vital functional qualities, all main parameters must be systematically dealt with throughout the whole design process. The launching system also has its requirements, deciding much

of the loads exerted upon the lifeboat. By a proper design, the launching system will therefore contribute to the optimal motion of the lifeboat. Today, two launching methods exist. One launches the lifeboat in a vertical drop while the other launches the lifeboat from a skid, causing it to have a forward motion at water impact. Of the two, the latter is found to be the most optimal and is therefore also the most used. Werenskiold (2011)

In the past, testing of lifeboat design has been carried out solely by experimental means. However, due to the large number of factors which influence the loads on the lifeboat structure and its occupants, optimization studies by experimental means have become both time-consuming and expensive. In addition, many effects cannot be studied at laboratory scale due to the inability to match all similarity requirements.

The use of experimental methods is suitable to determine the actual loads on structure and people inside lifeboat. However, data obtained from such experiments do not provide enough information necessary to propose new and improved design changes. For this purpose, the pressure and velocity distribution around the lifeboat's hull during water entry and the following diving and re-surfacing has to be known. Mørch et al. (2008)

Recent advances in computational fluid dynamics (CFD) have made it possible to analyze the lifeboat's performance under realistic conditions. By not being dependent on a physical model, investigation of a larger range of hull shapes at a variety of launch conditions can be done more easily and cost-efficiently. Today, different CFD-software such as OpenFoam, STAR-CCM+, Ansys, to mention some, exist. Each has their advantages and limitations, some being free (open source), others being licensed.

This thesis explores the possibility of using the CD-adapco's CFD-software STAR-CCM+ (STAR, v. 7.02.008) to predict the performance of free-fall lifeboats during the impact phase. The thesis focuses on verification of the software by studying water impact of different two and three-dimensional wedges. The numerical results predicted by the software are compared to already known solutions: both analytical and experimental.

The thesis consists of six more chapters containing, in short, the following:

- An introduction to Computational Fluid Dynamics (CFD) and basic knowledge for application of numerical methods when dealing with hydrodynamic problems. A presentation of the CFD-software STAR is also given (Chapter 2).
- Comparison of analytical and numerical solutions (STAR) for two-dimensional rigid wedges with constant velocity and varying deadrise angles. A refinement and improvement of the 2-D wedge impact study carried out by Johannessen (2011) (Chapter 3).
- Comparison of numerical (STAR) and experimental results for a free falling three-dimensional rigid wedge (Chapter 4).
- A study on the use of STAR when considering fluid-structure interaction (FSI), i.e. water impact of free falling three-dimensional elastic wedges (Chapter 5).
- Conclusions on the results predicted by STAR (Chapter 6).
- Recommendations on how STAR can be used to evaluate the performance of free-fall lifeboats (Chapter 7).

It is assumed that the reader possesses some basic understanding related to fluid flow and mechanics. Some experience in STAR is recommended, though not required.

COMPUTATIONAL FLUID DYNAMICS (CFD)

Computational Fluid Dynamics (CFD) is the science of describing fluid flows by producing numerical solutions to a system of partial differential equations (PDEs). By discrete methods, this is done with purpose to better understand, both qualitatively and quantitatively, physical phenomena present in different types of flows. Historically, the use of CFD was first applied for the airplane industry. However, due to the large economic advantage that may be obtained from being able to describe fluid flows, many other industries as the car and the oil industries, quickly followed in using CFD.

The extent to which the scientific and technological development of CFD is being used in marine applications is rather variable and their adaption by the designers of conventional merchant vessels has been disappointingly slow. This is due to the fact that ship construction has a long history of evolutionary design, over many centuries during which scientific methods were not available. Younger industries, such as the offshore industry, have been able to benefit rapidly from the application of science to technology development. This industry had no historical database to rely on and was forced to adopt a scientific approach. Rapid scientific and technological progress is nevertheless being made, driven in large measure by the offshore industry, and the recent interest in non-conventional merchant vessels, such as high-speed vessels (i.e. catamarans).

In marine CFD the main concern are the problems related to hydrodynamics. In most problems, the endeavor is to calculate global pressures and fluid velocity components in a three dimensional space surrounding the submerged portion of a marine vessel or other structure of interest (see Figure 2.1). From this, forces and moments acting on the marine vessel or offshore structure can be further calculated, whether steady or unsteady. For CFD in marine applications, the presence of the free surface provides a major departure from conventional CFD applications and the need to represent this fluid interface accurately presents a considerable challenge. For the most fundamental part of marine hydrodynamics, the ship resistance and propulsion, numerical calculations (CFD) have become increasingly important and have become an indispensable part of the design process. Today, a model of the final ship design is still tested in a towing tank, however, the testing sequence and content have changed significantly over the past years due to the use of CFD. Traditionally, unless the new ship which was to be designed was close to an experimental series or a known parent ship, the design process had to incorporate many model tests. Today, this is no longer feasible due to time-to-market requirements from ship-owners, and also, no longer necessary thanks to CFD developments. Combining computer-aided design (CAD) to generate new hull shapes, and following applying CFD to analyze these hull shapes, allows for rapid design explorations without model testing. By using CFD one can perform a pre-selection of

the most promising design and then hopefully only one or two model tests are needed to validate the intended performance features in the design. Gorski (2001), Dejhalla and Prpic-Orsic (2006), Ransau (2011)

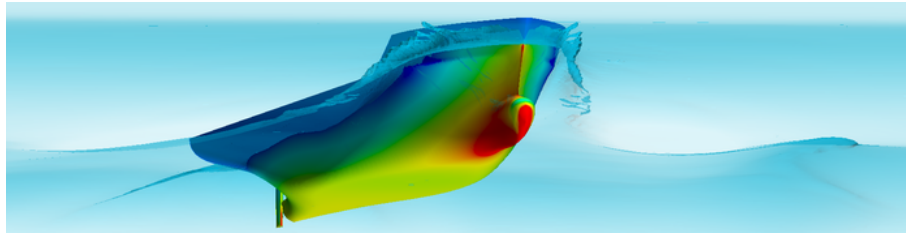


Figure 2.1: The pressure distribution that arises along a ship hull caused by forward motion of the ship in head sea predicted in STAR. CD-adapco (2012)

This chapter will introduce basic knowledge for the application of numerical methods in marine hydrodynamics. The CFD-software STAR-CCM+, developed by CD-adapco, will be discussed and brief comments on how to set up a simulation are presented.

2.1 INTRODUCTION TO CFD

This section is to provide the reader with insight in basic methods and physical models behind CFD. Much of the following presented material are a result of literature provided by Pettersen (2011) and Ransau (2011). It should be noted that only a brief introduction is given. Deduction of equations, such as the Navier-Stokes equations, will not be emphasized. Attention directed to complex flow phenomena such as turbulence is also not given here. For this, the reader is encouraged to study Johannessen (2011) and CD-adapco (2011).

THE CFD PROCESS

The motivation behind use of CFD is due to the fact that extensive studies of fluid flows using experiments are prohibitively expensive and time consuming. In addition, CFD allows the study of very small scales and time development (in slow motion) of phenomena that otherwise would not be visible. Because the equations governing fluid flows of practical importance are very complicated, computers have to be used to solve the partial differential equations (PDEs) describing the problem at hand. Also, analytical solution for these types of problems does not exist, only solutions for very few and simple physical cases.

In computational techniques the governing PDE's are replaced with systems of algebraic equations solvable by a computer. Table 2.1 shows the process of obtaining practical, useful information about problems involving fluid motion. In most general cases, the following quantities are needed in order to describe fluid flow phenomena:

- the velocity field: $\mathbf{u} = [u(x, y, z, t), v(x, y, z, t), w(x, y, z, t)]^T$
- the pressure field: $p(x, y, z, t)$
- Density distribution: $\rho(x, y, z, t)$
- Temperature distribution: $T(x, y, z, t)$

*Usually, in marine hydrodynamic applications, the density and temperature distribution are not of interest.

CFD draws on 4 disciplines:

- Fluid Mechanics
- Mathematics (classical and numerical analysis)
- Computer science
- Geometric modeling and meshing

To perform a good CFD calculation and obtain reasonable result, it is necessary to be aware of some aspects of each of these 4 disciplines.

Table 2.1: The process of obtaining practical, useful information about problems involving fluid motion. Ransau (2011)

Conservation of mass	\Rightarrow	Continuity equation
Newton's second law	\Rightarrow	Euler/Navier-Stokes equations
Conservation of energy	\Rightarrow	Energy equation
	\Downarrow	solve the equations (+ boundary conditions) using CFD
Velocity distribution	:	$u(x, y, z, t), v(x, y, z, t), w(x, y, z, t)$
Pressure distribution	:	$p(x, y, z, t)$
Density distribution	:	$\rho(x, y, z, t)$
Temperature distribution	:	$T(x, y, z, t)$

In CFD, the cornerstone is the fundamental governing equations of fluid dynamics: continuity, momentum and energy equations, as listed in Table 2.1. These equations are mathematical statements of physical principles upon which the whole fluid dynamics is based:

1. mass is conserved
2. Newton's second law
3. energy is conserved

The equations can be obtained in various forms, but for most hydrodynamics theory, the particular form of the equations used makes little difference. The equations are the same whether the flow is around a ship, over a submarine, through a platform, past a cylinder, past a car or an airplane. What separates the cases, are the flow fields determined by the boundary conditions. These conditions dictate the particular solution to be obtained from the governing equations.

When solving a flow problem using CFD it is common to follow a certain "recipe" or work flow. This recipe can be seen as "universal" regardless of the CFD-software at hand and its steps can be listed as follows (Ransau (2011)):

1. Study the physical flow:
 - \rightarrow identify main flow phenomena.
2. Construct a mathematical model:
 - \rightarrow analyze the partial differential equations.
 - \rightarrow define the (physical) boundary conditions.

3. Formulate the numerical problem:
 - construct a mesh.
 - choose a time differencing scheme.
 - choose a space differencing scheme.
 - choose initial conditions.
 - choose the (numerical) boundary conditions.
 - solve difference equations (check stability and consistency).
4. Implement the formulation in a computer code:
 - structured programming, environment.
5. Run code and obtain the solution:
 - computer system.
6. Analyze and interpret the obtained result:
 - flow visualization.
7. Draw conclusions:
 - answer practical hydrodynamic problems.

To obtain a numerical solution, two stages needs to be properly defined: the discretization and the equation solver (see Figure 2.2). In the first stage, the continuous PDEs, together with boundary conditions and initial conditions are converted into a discrete system of algebraic equations. The starting point for the discretization is the governing equations. Different forms of the equations can be applied: integral of differential form, conservative or non-conservative form.

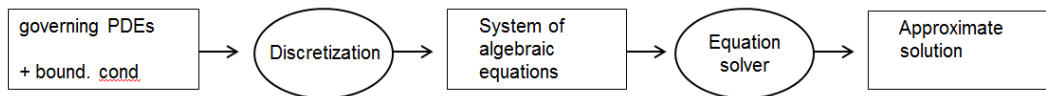


Figure 2.2: Stages in CFD. Ransau (2011)

To obtain a solution of the discretized equations an equation solver is needed to provide the solution for the system of algebraic equations. The system of algebraic equations is typically of the form:

$$\begin{aligned}
 a_{11}u_1 + a_{12}u_2 + \dots + a_{1n}u_n &= c_1 \\
 a_{21}u_1 + a_{22}u_2 + \dots + a_{2n}u_n &= c_2 \\
 &\vdots \\
 a_{n1}u_1 + a_{n2}u_2 + \dots + a_{nn}u_n &= c_n
 \end{aligned}$$

In a more compact form:

$$\mathbf{A}\mathbf{u} = \mathbf{b}$$

where \mathbf{A} is a $n \times n$ -matrix of know coefficients, \mathbf{u} is the column vector containing the unknowns and \mathbf{b} is a column vector of know quantities.

Two general types of solvers exist: direct solvers and iterative solvers. For a direct solver, the solution of the linear system can be obtained exactly in a "finite" time. For an iterative solver, the exact solution cannot be obtained in a finite time. However, as the number of iterations increases the approximations in an iterative solver will become closer and closer to the exact solution.

PRACTICAL ISSUES

In general, numerical methods must demonstrate a number of properties in order to be successful. Five important properties are:

1. consistency
2. stability
3. convergence
4. conservation
5. accuracy

A description of the various properties are presented in Day (2010). The description is summarized below.

Consistency

A numerical method is said to be *consistent* if the discretized equations converge to the "exact" (continuum) equations in the limit as the grid size tends to zero, i.e. $\Delta t \rightarrow 0$ and $\Delta x, \Delta y, \Delta z \rightarrow 0$.

There will always almost be a difference between the discretized and the exact equation and this error is referred to as the *truncation error*. As $\Delta t \rightarrow 0$ and $\Delta x, \Delta y, \Delta z \rightarrow 0$ one should expect the truncation error to approach zero.

Even if the approximations is consistent, there is no guarantee that the solution of the discretized equation system will become the exact solution of the differential equation in the limit of infinitesimal step size. In order to achieve this, the method applied needs also to be *stable*.

Stability

A numerical method is said to be *stable* if it does not amplify the errors that appear in the course of numerical solution process. For an unstable method, an error will cause the disturbance to either grow indefinitely, destroying numerical solution, or cause large-amplitude oscillations of the numerical results.

Characterization of the stability in a solution is usually described by the Courant-Friedrichs-Levi condition (CFL number):

$$CFL = u \frac{\Delta t}{\Delta x} \quad (2.1)$$

Here, u is the characterized velocity, Δt the time step and Δx the grid size. The higher the value of the CFL-number, the more likely it is that instability will occur. For an explicit CFD scheme to be stable, a CFL value less than 1 is desirable, while for implicit solutions, the methods are more stable and able to tolerate $CFL > 1$ ¹.

Convergence

One say that the solution is convergent if the solution of the discretized equations tends to the exact solution of the differential equations as the grid spacing tends to zero ($\Delta x, \Delta y, \Delta z \rightarrow 0$). It is noted that a method will only converge if it is both consistent and stable. Convergence is usually checked by solving the problem on a

¹An explicit scheme contra an implicit scheme differs in the number of unknowns when calculating the flow properties at the present time.

series of increasingly refined grids (and time steps). If the method is convergent (i.e. consistent and stable), the solution will converge to a *grid-independent solution*.

As a solution is always achieved through iterations, the rate which the results improve from one iteration to another (*convergence rate*) is important, and it is desirable that this rate is high.

Conservation

The equations to be solved are conservation laws and hence the discretized equations in the numerical solution should also obey these laws, throughout the whole computational domain. This property is usually fulfilled automatically for finite-volume methods up to the machine error (with some exceptions). If conservation is conserved (i.e. the relevant fluid properties are conserved), one can expect the errors to consist only of inaccurate distribution of fluid properties over the computational domain.

Accuracy

A numerical solution is only approximate, and its accuracy is dependent on the errors which are introduced in the course of the development of the solution algorithm, in programming the algorithms and in setting up the boundary conditions. In addition, a numerical solution is said to always include at least four types of systematic errors:

- ***modeling errors:***
the errors caused by the difference between the actual flow and the exact solution of the mathematical problem.
- ***discretization errors:***
the errors caused by the difference between the exact solution of the original differential equations and the exact solution of the discretized version of these equations.
- ***iteration errors:***
the errors caused by the difference between the achieved iterative solution and the exact solution of the discretized equations.
- ***round-off errors (machine errors):***
the errors caused by the limitations of the hardware.

Assumptions made when the transport equations for the variables (mass, momentum etc.) are derived gives rise to the ***modeling errors***. Modeling errors is often also introduced when simplification in geometries or boundary conditions are performed. Such type of errors are not known in advance and can only be evaluated by comparing solutions in which other errors are known to be negligible (with accurate experiment data or data obtained from more accurate models).

Due to the limitations of computational elements (control volumes) and computational domain, ***discretization errors*** arises.

The ***iteration errors*** are related to the quality of the numerical solution procedure on the given grid and with the given model. Iteration errors are sometimes also referred to as *convergence errors*. However, one should note that the errors are unrelated to grid convergence, but to the convergence of the iterative schemes for solving systems of matrix equations.

As of today, ***round-off errors*** are much reduced due to increased accuracy resulting from the ability to store real number with more accuracy (using more memory). A

poorly written code can, however, accumulate round-off errors rapidly, especially when numbers of very different sizes are handled.

2.2 STAR-CCM+

STAR-CCM+ (STAR) is a CFD-software developed by CD-Adapco with purpose to introduce an easy-to-use engineering tool not only reserved for experts within the CFD discipline. Besides being a CFD solver, STAR is an entire engineering process for solving problems involving flow, heat transfer and stress. This is made possible by developing a suite of integrated components, together producing a powerful package that can address a wide variety of modeling needs. These components include:

- 3D-CAD modeler
- CAD embedding
- Surface preparation tools
- Automatic meshing technology
- Physics modeling
- Turbulence modeling
- Post-processing
- CAE Integration

As for all CFD software, STAR follows a strict workflow when numerically solving a given CFD problem. Figure 2.3 below gives an overview of the workflow implemented in the STAR software.

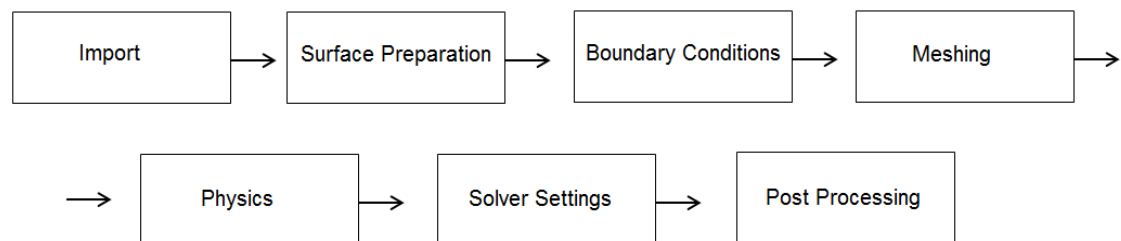


Figure 2.3: Workflow overview in STAR.

The STAR software is based on a finite volume method². This means, that by utilizing the divergence theorem, volume integrals in a partial differential equation (that contain a divergence term) are converted to surface integrals. With appropriate initial and boundary conditions and by means of a number of discrete approximations, an algebraic equation system solvable on a computer is obtained.

In the following, a basic description of the solution method, work flow and physics in STAR will be given. It should be noted that this is only a brief introduction and that the STAR-software contains a huge amount of additional features than what is described below. As this thesis is focusing on studying solid (wedge) - fluid (water) impact and interaction, description will be aimed at the concept of multiphase flow³.

²The finite volume method is a method for representing and evaluating partial differential equations in the form of algebraic equations.

³Multiphase flow is a term which refers to the flow and interaction of several phases within the same system where distinct interfaces exist between the phases.

The given description will therefore, to some extent, follow what is done when setting up the simulations described the later chapters.

The following is a summary of details found in CD-adapco (2011) (unless otherwise stated).

SOLUTION METHOD

In section 2.1 an outline of a general CFD process is given. Here, a description of the solution process in STAR is presented. The following is a summary of Mørch et al. (2008).

The CFD software STAR is based on a finite-volume (FV) method and starts from conservation equations in integral form. In the computations, an algebraic equation system solvable on a computer is obtained by means of discrete approximations with appropriate initial and boundary conditions. As a first step, the spatial solution domain is subdivided into a finite number of contiguous control volumes (CVs). These volumes can be of arbitrary polyhedral shape. The governing equations used contain surface and volume integrals, as well as time and space derivatives.

For a viscous three-dimensional flow, the flow is assumed to be governed by the Reynolds-averaged Navier-Stokes equations, in which the turbulence effects are included via an eddy-viscosity model. In this case, the continuity equation, three momentum components equations, and two equations for turbulence properties are solved. In addition, the space-conservation law must be satisfied as the CVs move as the solid moves. The equations are:

Mass conservation:

$$\frac{d}{dt} \int_V \rho \, dV + \int_S \rho(\mathbf{v} - \mathbf{v}_b) \cdot \mathbf{n} \, dS = 0 \quad (2.2)$$

Momentum conservation:

$$\frac{d}{dt} \int_V \rho \mathbf{v} \, dV + \int_S \rho \mathbf{v}(\mathbf{v} - \mathbf{v}_b) \cdot \mathbf{n} \, dS = \int_S (\mathbf{T} - p\mathbf{I}) \cdot \mathbf{n} \, dS + \int_V \rho \mathbf{b} \, dV \quad (2.3)$$

Generic transport equation for scalar quantities:

$$\frac{d}{dt} \int_V \rho \phi \, dV + \int_S \rho \phi(\mathbf{v} - \mathbf{v}_b) \cdot \mathbf{n} \, dS = \int_S \Gamma \nabla \phi \cdot \mathbf{n} \, dS + \int_V \rho b_\phi \, dV \quad (2.4)$$

Space conservation law:

$$\frac{d}{dt} \int_V \, dV - \int_S \mathbf{v}_b \cdot \mathbf{n} \, dS = 0 \quad (2.5)$$

In these equations, ρ stands for fluid density, \mathbf{v} is the fluid velocity vector and \mathbf{v}_b is the velocity of the CV surface; \mathbf{n} is the unit vector normal to the CV surface with area S and volume V . \mathbf{T} stands for the stress tensor (expressed in terms of velocity gradients and eddy viscosity), p is the pressure, \mathbf{I} is the unit tensor, ϕ stands for the scalar variable (k , ε or ω), Γ is the diffusivity coefficient, \mathbf{b} is the vector of body forces per unit mass and b_ϕ represents sources and sinks of ϕ .

To account for the free surface and allow for its arbitrary deformation, an additional equation needs to be solved for the volume fraction o of the liquid phase:

$$\frac{d}{dt} \int_V o \, dV + \int_S o(\mathbf{v} - \mathbf{v}_b) \cdot \mathbf{n} \, dS = 0 \quad (2.6)$$

The liquid (water) and gas (air) are considered as two immiscible components of a single effective fluid, whose properties are assumed to vary according to the volume fraction of each component as follows for the density ρ and viscosity μ :

$$\rho = \rho_1 c + \rho_2(1 - o), \quad \mu = \mu_1 c + \mu_2(1 - o)$$

Here, both components can be either compressible or incompressible.

The above equations close the mathematical model of fluid flow computed when using moving grids (as applied in Chapter 4 in this thesis). The grid movement is not prescribed by initial conditions, but depends on the motion of the solid and needs to be determined as part of the solution. This requires a coupled solution of the above mentioned equations and six equations describing the motion of a floating body. These six equations are in general:

Three component equations for the linear motion:

$$\frac{d(m_B \mathbf{v}_C)}{dt} = \mathbf{F}_B \quad (2.7)$$

Three component equations for the angular motion:

$$\frac{d(\mathbf{I}_C \cdot \omega_B)}{dt} = \mathbf{M}_C \quad (2.8)$$

Here m_B is the body mass, \mathbf{v}_C is the velocity of the body's center of mass, \mathbf{I}_C its moment of inertia, ω_B is its angular velocity, \mathbf{F}_B is the force and \mathbf{M}_C the moment acting on the body. The force typically consists of flow-induced forces (with shear stress and pressure contributions) and the body weight; the latter does not contribute to the moment about the center of mass:

$$\mathbf{F}_B = \int_S (\mathbf{T} - p\mathbf{I}) \cdot \mathbf{n} \, dS + m_B \mathbf{g} \quad (2.9)$$

$$\mathbf{M}_C = \int_S (\mathbf{r} - \mathbf{r}_C) \times ((\mathbf{T} - p\mathbf{I}) \cdot \mathbf{n}) \, dS \quad (2.10)$$

Here \mathbf{g} stands for gravity acceleration and \mathbf{r} for the position vector relative to a fixed reference frame; index "B" denotes body and "C" the center of body mass.

The integrals presented here are all approximated by midpoint rule, i.e. the value of the function to be integrated is first evaluated at the center of the integration domain and then multiplied by the integration range.

By a segregated iterative method, the solution of the Navier-Stokes equations is accomplished. Here, the linearized momentum component equations are solved first using prevailing pressure and mass fluxes through cell faces (inner iterations), followed by solving the pressure correction equation derived from the continuity equation (SIMPLE-algorithm; see Ferziger and Peric (2003) for more details). A flow chart of the iterative solution method is illustrated in Figure 2.4.

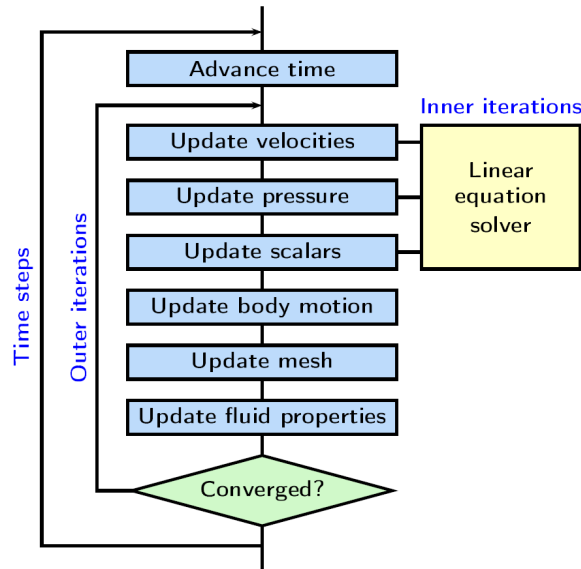


Figure 2.4: Flow chart of the iterative solution method for a coupled simulation of fluid flow and flow induced motion in a floating body. Mørch et al. (2008)

When computing the motion of a floating body, the outer iteration loop within each time step is extended to allow for an update of the body position. After each update of fluid velocity and pressure, forces and moments acting on the body are estimated and used to solve equations of body motion.

It is beyond the scope of this thesis to go further into all the details of the numerical solution method. The reader is encouraged to study details in Demirdzic and Muzaferija (1995), Ferziger and Peric (2003), Muzaferija and Peric (1999) and Xing-Kaeding (2006).

MODELING

For most simulations in STAR, a first step is to prepare the geometry for the case to be studied. The geometry that is to be considered can either be imported from external CAD-programs (Catia, SolidWorks etc.) or created directly using the 3-D-CAD module which exist within the STAR-software.

The 3-D-CAD module allows geometries to be built from scratch and can also be used to make modifications to the imported CAD model. Unique for the 3-D-CAD module is that the model can be modified outside the 3-D-CAD environment. This allows the possibility to change size on one or more components, and re-run the analyzes quickly. If a solution has already been computed it will be mapped across the modified geometry, thereby decreasing the overall run time. Figure 2.5 shows the geometry of the half-wedge used in the three-dimensional study in Chapter 4. The wedge is modeled entirely within STAR.

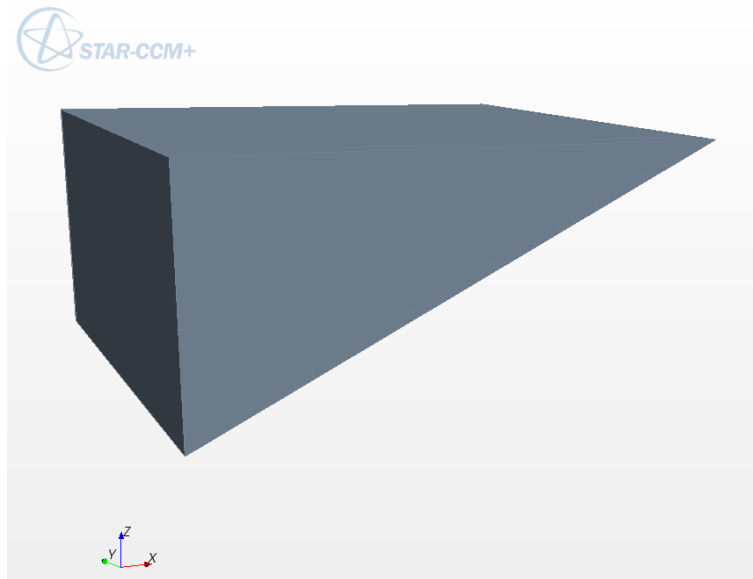


Figure 2.5: The modeled half-wedge used in the three-dimensional study in Chapter 4.

BOUNDARY CONDITIONS

To obtain a proper solution of the problem being solved, it is critical that the boundaries are appropriately separated and demarcated for specific conditions and values to be assigned. This holds for both meshing and analysis set-up.

In a multiphase flow, boundary conditions are usually set by defining an inlet, an outlet, a wall (referred to as the solid) and symmetry condition. A wall condition is set so to make the tangential velocity equal to 0. Physically, this implies that there will be no flow over the boundary, hence the wall makes out an impermeable surface. The symmetry condition is used such to simplify the problem and accordingly reduce computational time. A symmetry plane enforces no flow through the symmetry plane but allows the fluid to flow along the plane without being disturbed by shear forces. The symmetry plane boundary therefore represents an imaginary plane of symmetry in the simulation. The solution obtained with such a boundary plane is identical to the solution that would be obtained by mirroring the mesh about the symmetry plane.

The inlet and outlet represents ducts at which the flow properties are known. Depending on the problem being analyzed the inlet and outlet can be of following type:

- **Mass Flow Inlet**

Represents an inlet for which the mass flow rate is known.

- **Stagnation Inlet**

Refer to the condition in an imaginary plenum, far upstream, in which the flow is completely at rest.

- **Velocity Inlet**

Represents the inlet of a duct at which the flow velocity is known.

- **Pressure Outlet**

A flow outlet boundary at which the pressure is specified.

- Flow-Split Outlet

Used when multiple flow split outlets bound a fluid continuum. A fraction of the total mass flow through each of the outlet boundaries is specified.

MESH

A good mesh forms the basis for good results through the analysis, and a starting point for generating a mesh is a description of the geometry surface. From this description two cycles of meshing of the geometry needs to be done: surface meshing and volume meshing.

Surface mesh

STAR contains tools which can be used to help prepare the starting surface geometry so that a high-quality volume mesh can be created from it. Most used is the surface remeshing and the surface wrapper.

The surface remeshing is used to re-triangulate an existing surface in order to improve the overall quality of the surface and optimize it for the volume mesh models. Typically, the surface remeshing is used for remeshing surfaces produced by the surface wrapper.

To provide a closed, manifold, non-intersecting surface (a requirement for CFD analysis), the surface wrapper can be used. This feature is used when the imported geometry include problems such as surface mismatches, intersecting parts, double and internal surfaces and overly complex geometry with too much detail. As the resulting surface quality from the surface wrapper is not always optimal, the surface remeshing is often used afterward to provide a high-quality starting surface for the volume mesh.

Volume mesh

In STAR three different types of meshing models can be used to generate a volume mesh: tetrahedral, polyhedral, trimmed mesh.

The tetrahedral mesh is used to provide an efficient and simple solution for complex mesh generation problems. It is the fastest of the provided models and uses least amount of memory for a given number of cells.

Polyhedral meshes (used in Chapter 5) provide a balanced solution for complex mesh generation problems. They are relatively easy and efficient to build, requiring no more surface preparation than the equivalent tetrahedral mesh.

The trimmer meshing model utilize a template mesh constructed from hexahedral cells from which it cuts or trims the core mesh based on the starting input surface. Of the mentioned mesh models, the trimmer is expected to produce best results when working with multiphase flow and free surface (due to its ability to describe the smooth free surface). This is therefore used in the simulations of the water entry of rigid wedges (Chapter 3 and 4). Figure 2.6 shows the trimmer meshing model applied in the simulation domain.

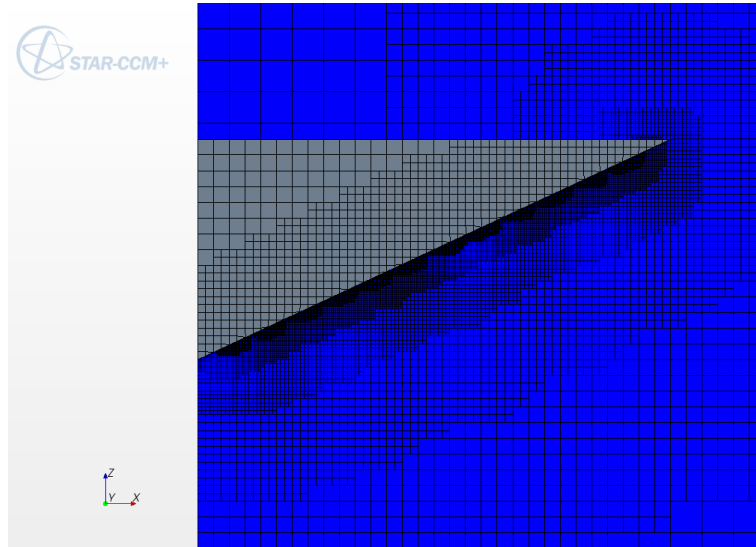


Figure 2.6: The trimmer meshing model applied on the modeled half-wedge and domain used in the three-dimensional study in Chapter 4.

PHYSICS

Depending on what is to be analyzed, different physics models need to be applied. In STAR the following models exist:

- Space, time and motion
- Materials
- Flow and energy
- Species
- Turbulence and transition
- Radiation
- Aeroacoustics
- Combustion
- Multiphase flow
- Solid stress
- Electromagnetism

As this thesis is aimed at studying solid-fluid impact and interaction, multiphase Volume Of Fluid (VOF) and VOF wave models, together with motion and time models, will be further discussed.

Volume Of Fluid (VOF)

VOF is a simple multiphase model that is well suited when simulating flows of several immiscible fluids on numerical grids capable of resolving the interface between the mixture's phases. Due to its numerical efficiency, the model is well suited for simulations of flows where each phase constitutes a large structure, with a relatively small total contact area between phases (as for water and air). The spatial distribution of each phase at a given time is defined in terms of a variable called the volume fraction⁴. A method of calculating such distributions is to solve a transport equation for the phase volume fraction. For this, the method uses the STAR segregated flow model. The

⁴The volume fraction of a phase is the ratio of the volume occupied by the phase over the computational cell volume.

segregated flow model solves the flow equations (one for each component of velocity, and one for pressure) in a segregated, or uncoupled, manner.

To set up a proper VOF multiphase simulation corresponding physics models has to be chosen. Figure 2.7 show an example of choice of models when studying water entry of a rigid wedge. Notice that turbulence in the flow is accounted for.

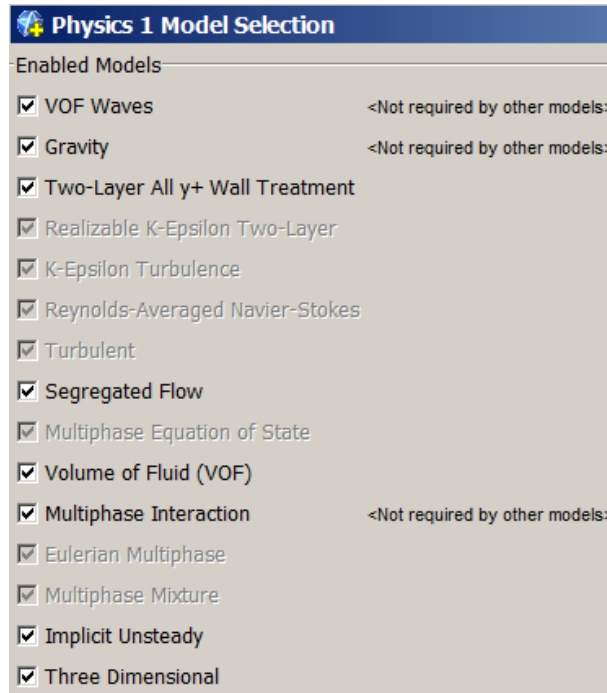


Figure 2.7: Physics models to be chosen when studying water entry of a rigid wedge in STAR.

VOF wave

To simulate surface gravity waves on a light fluid-heavy fluid interface, VOF Waves, together with the VOF multiphase model, needs to be applied. These models are typically used with the 6-DOF DFBI⁵ motion model for marine applications (this is done in Chapter 4, though only with vertical translational motion of a three-dimensional wedge). When created, VOF Waves provide *field functions*. Field functions provide a mechanism by which fields (raw data from the simulation stored in the cells and/or on the boundaries) may be viewed and defined in STAR. The field functions can be used to initialize the VOF calculations and to provide suitable profiles at boundaries. Figure 2.8 illustrate how the VOF wave model in STAR simulates the water rise-up around the wedge at water entry.

Motion

In STAR there are three broad categories for defining motion: mesh displacement in real time (MDRT), moving reference frame in steady-state and harmonic balance flutter⁶. The methods that involve actual displacement of the mesh vertices in real time is found in the first category. These methods must be used in conjunction with a transient analysis, as is the case for this thesis.

⁵Dynamic Fluid Body Interaction.

⁶Harmonic Balance Flutter motion is used in simulations that involve the Harmonic Balance method with blade vibration.

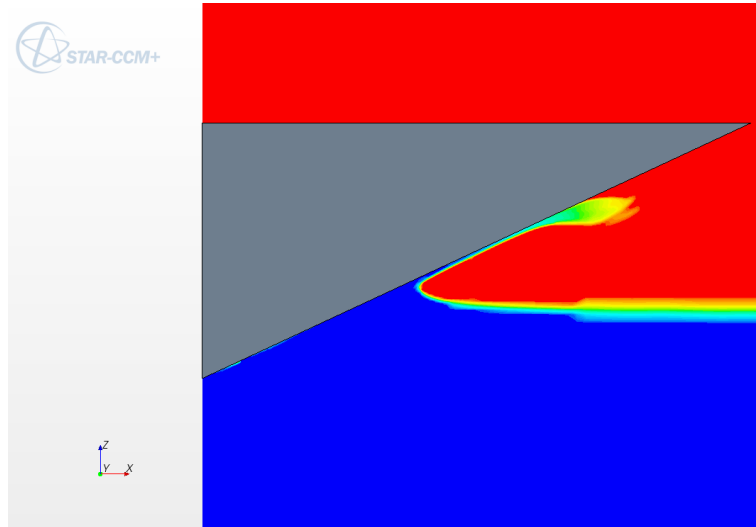


Figure 2.8: Water rise-up at the half-wedge used in the three-dimensional study in Chapter 4.

In the MDRT category four main methods are available:

- Dynamic Fluid Body Interaction.
- Rigid Motion.
- Morphing (deforming mesh).
- Solid Displacement.

In this thesis, all of the four methods (with some modification) are applied. Dynamic Fluid Body Interaction for the constant velocity two-dimensional case in Chapter 3, Rigid Motion for the free-falling three-dimensional case in Chapter 4 and Morphing together with Solid Displacement for the FSI study in Chapter 5.

Time

In STAR there exist three ways of modeling time. The function of the time models is to provide solvers (see next section) that control the iteration and/or unsteady time-stepping. The three time models are:

- Steady.
- Implicit unsteady.
- Explicit unsteady.

When studying segregated flow (as done in this thesis) only the implicit unsteady model can be applied. This is due to the fact that the VOF wave model is unable to solve the pressures and velocity components in a coupled manner.

SOLVERS

The solvers feature is to control the solution. It is activated once per iteration or once per time-step for implicit unsteady simulations. Usually, when setting up a physics model, the needed solver will be chosen automatically.

For a multiphase VOF problem, a segregated VOF solver is chosen. The solver controls the solution update for the phase volume fractions. This means that for each phase present in the flow, the discretized volume-fraction conservation equation (2.6) is solved.

In several of the studies in this thesis, the segregated VOF solver is the one used. This solver controls the solution update for the segregated flow model according to the SIMPLE algorithm. It also controls the velocity solver and the pressure solver. The velocity solver solves the discretized momentum equation to obtain the intermediate velocity field, while the pressure solver solves the discrete equation for pressure correction, updating the pressure field.

By the SIMPLE algorithm the overall solution is controlled. The algorithm may be summarized as follows and is done for every time step (ref. Figure 2.4).

1. Set the boundary conditions.
2. Compute the reconstruction gradients of velocity and pressure.
3. Compute the velocity and pressure gradients.
4. Solve the discretized momentum equation to create the intermediate velocity field \mathbf{v}^* .
5. Compute the uncorrected mass fluxes at faces \dot{m}_f^* .
6. Solve the pressure correction equation to produce cell values of the pressure correction p'_b .
7. Update the pressure field:

$$p^{n+1} = p^n + \omega p'$$
 where ω is the under-relaxation factor for pressure.
8. Update the boundary pressure corrections p'_b .
9. Correct the face mass fluxes:

$$\dot{m}_f^{n+1} = \dot{m}_f^* + \dot{m}'_f.$$
10. Correct the cell velocities:

$$\mathbf{v}^{n+1} = \mathbf{v}^* - \frac{V \nabla p'}{\mathbf{a}_p^V}$$
 where $\nabla p'$ is the gradient of the pressure corrections, \mathbf{a}_p^V is the vector of central coefficients for the discretized linear system representing the velocity equation and V is the cell volume.
11. Update density due to the pressure changes.
12. Free all temporary storage.

To ensure convergence in the solution at each time step, a certain number of iterations is required. The optimal number of iterations can be found by analyzing the residuals⁷. The most important residual when studying the free surface is the residual for water and air. Here it is recommended that the residual drops in the order 10^2 . However, it is proven that a drop of residual in the order 10^1 is sufficient (giving a converging solution), Kopperstad (2011).

⁷The residual represents the degree to which the discretized solution is not satisfied.

POST PROCESSING

After the solver (and the initial conditions) are set, the simulation can be run. By the use of field functions, STAR allows for the possibility to analyze the solution while the simulation is running, as well as when it completes. The field functions can be analyzed either/or by creating reports, plotting sets of data and/or by visualizing the solution data. To sample and save the solution data while the simulation is running, monitors are used. Usually, the needed monitor is chosen automatically when choosing a solver.

Some of the different representation methods that can be utilized during a simulations can be studied under **ANALYZING AND POST PROCESSING** in Chapter 3.

WATER ENTRY OF TWO-DIMENSIONAL WEDGES

Determination of slamming loads on a body at water impact is considered complex and difficult to describe with simple expressions or simulations. Computational Fluid Dynamics (CFD) has become a well-known and suitable tool when analyzing fluid-body interaction and the physical problems that arises during an impact. By the use of CFD and the Volume of Fluid (VOF) method, water entry problems can be simulated and solved, even for complex three-dimensional geometries.

Using CFD-software to simulate complex three-dimensional problems are extremely time consuming and can take days to perform, depending on the computer cluster at hand. Two-dimensional problems, on the other hand, are generally much faster and can be used as a guideline to results one would expect to get in 3-D. This approach is especially used in situations where the flow is approximately two-dimensional, e.g. for ship stern slamming in head or following sea. As an aid in understanding planing and slamming of marine vessels, constant velocity water entry of wedge shaped sections is therefore important.

This chapter will study the slamming phenomena for a two-dimensional wedge with a forced downward velocity. Parameters characterizing the slamming loads for such a case are the position and value of the maximum pressure, the time duration and the spatial extent of the high slamming pressure. (The definitions of the slamming parameters are presented in Figure 3.16 in section 3.3.)

In the following study, these parameters, together with the total hydrodynamic force F_3 on the wedge, is used to characterize the slamming problem for wedges with varying deadrise angles. The parameters are found using the CFD software STAR-CCM+ and comparison of the parameters are made with a similarity solution, an asymptotic solution and a nonlinear boundary element method.

3.1 SOLUTIONS USED FOR COMPARISON

STAR-CCM+ is used to study the water entry of two-dimensional wedges with deadrise angles varying from 4° to 81° . To validate the solution, results are compared with numerical results found in Zhao and Faltinsen (1992). In this paper - *Water entry of two-dimensional bodies*, Zhao and Faltinsen presents a numerical boundary method (BEM) for studying water entry of a two-dimensional body with an arbitrary cross-section. They also present a similarity and an asymptotic solution. The three solution methods are summarized in the following.

BOUNDARY ELEMENT METHOD

The boundary element method (BEM) solution by Zhao and Faltinsen is a nonlinear BEM with a jet flow approximation. A brief introduction to the theory is given here but the reader is encouraged to study Zhao and Faltinsen (1992) for further details.

A two-dimensional body that is forced with vertical constant velocity through the initially calm free surface is considered. It is assumed that no air pocket between the body and the free surface is formed during the impact. Hence the deadrise angle α is larger than 2-3 degrees. The water is assumed to be incompressible and the flow irrotational such that a velocity potential ϕ satisfies the Laplace equation in the fluid domain:

$$\frac{\partial^2 \phi}{\partial y^2} + \frac{\partial^2 \phi}{\partial z^2} = 0 \quad (3.1)$$

Due to the large fluid accelerations that occur on impact the effect of gravity is neglected. The kinematic free-surface condition is that a fluid particle remains on the free surface. Hence the motion of the free surface may be found by integrating the fluid velocity.

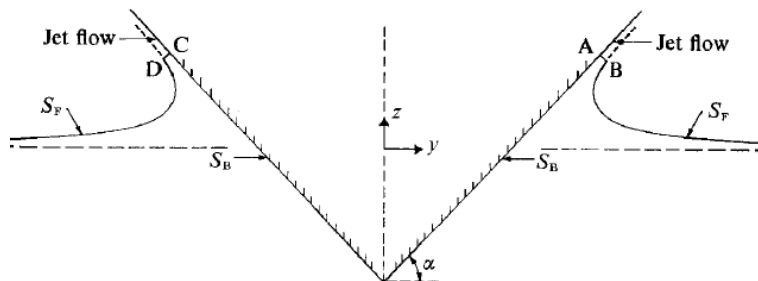


Figure 3.1: Definitions of coordinate system and control surfaces used in the numerical solution of water entry of a wedge; α = deadrise angle. Zhao and Faltinsen (1992)

A jet flow is assumed created at the intersection between the free surface and the body surface. In the upper part of the jet the pressure is set equal to the atmospheric pressure p_0 . The solution is simplified by defining an instantaneous fluid domain Ω that does not contain the whole jet flow. By Green's second identity the velocity potential ϕ for the flow inside the fluid domain is represented:

$$2\pi\phi(y, z) = \int_S \left[\frac{\partial\phi(\eta, \zeta)}{\partial n(\eta, \zeta)} \log r - \phi(\eta, \zeta) \frac{\partial \log r}{\partial n(\eta, \zeta)} \right] ds(\eta, \zeta), \quad (3.2)$$

where $r = [(y - \eta)^2 + (z - \zeta)^2]^{\frac{1}{2}}$, S is the surface enclosing the domain, \vec{n} is the normal vector of the surface enclosing the domain, (y, z) are the coordinates of points inside

the fluid domain and (η, ζ) are the coordinates of points on the surface domain. Further deduction of 3.2 used in this BEM solution will not be presented here. Details are found in Zhao and Faltinsen (1992).

The BEM problem is solved as an initial value problem where the velocity potential ϕ and the free-surface elevation are set equal to zero at the initial time. At each time instant an integral equation resulting from 3.2 is solved. The pressure on the body is found by Bernoulli's equation.

In the numerical solution conducted by Zhao and Faltinsen conservation of mass, momentum and energy are satisfied. The solution has also been checked against the similarity solution for wedges and asymptotic formula for small deadrise angles. The latter solutions are described in the following sections.

SIMILARITY SOLUTION

Similarity solutions for flow around symmetric wedges with constant vertical velocity V through a calm free surface is presented by Dobrovol'skaya (1969). In the flow the fluid velocity can be written as

$$\nabla\phi = VF \left(\frac{y}{Vt}, \frac{z}{Vt} \right), \quad (3.3)$$

where F is a function that Dobrovol'skaya finds by first solving the following integral equation

$$f(t) = \frac{1}{\pi} \frac{c_0^2}{c^2} \int_0^t \frac{(1-t)^{-1-\gamma} \exp \left[t \int_0^1 \frac{f(\tau)}{\tau(\tau-t)} d\tau \right] dt}{\int_t^1 t^{-\frac{3}{2}} (1-t)^{-\frac{1}{2}+\gamma} \exp \left[-t \int_0^1 \frac{f(\tau)}{\tau(\tau-t)} d\tau \right] dt}, \quad (3.4)$$

where

$$\frac{c_0^2}{c^2} = \frac{\int_{0.5}^1 r^{-\frac{3}{2}} (1-r)^{-\frac{1}{2}+\gamma} (2r-1)^{-\gamma} \exp \left\{ - \int_0^1 \frac{f(\tau) d\tau}{\tau[\tau\{2-(1/r)\}-1]} \right\} dr}{\int_{0.5}^1 (1-r)^{-1-\gamma} (2r-1)^{-1+\gamma} \exp \left\{ \int_0^1 \frac{f(\tau) d\tau}{\tau[\tau\{2-(1/r)\}-1]} \right\} dr}. \quad (3.5)$$

In the above equation $\gamma = 0.5 - \alpha/\pi$. The unknown function $f(t)$ is defined for t between 0 and 1. The parameter t does not mean time in this context: $f(t)$ is bounded and is proportional to the angle of inclination of the free surface along the y -axis. $t = 1$ corresponds to the intersection point between the free surface and the body surface and $t = 0$ to the point of infinity along the free surface.

Dobrovol'skaya (1969) solves (3.4) by iteration for deadrise angles 30° , 60° and higher. A different approach has been presented by Hughes (1972) for a deadrise angle equal to 45° . The accuracy needed in the numerical computations increases with decreasing deadrise angle and Zhao and Faltinsen presented a different numerical scheme capable of calculating results for deadrise angles down to 4° . In the solution proposed, ratios of mass, energy and force ratios are shown to be within 1.0 ± 0.01 , except for $\alpha = 4^\circ$. Asymptotic results presented by Cointe (1991) are in agreement with those found in the similarity solution by Zhao and Faltinsen (1992).

ASYMPTOTIC SOLUTION

For small deadrise angles it is possible to use matched asymptotic expansions to solve the 2-D wedge flow. In the solution the flow is divided into an inner and outer flow domain. The inner flow is studied with respect to the jet flow between the free surface and the body and is shown by Armand and Cointe (1986), Cointe (1991) and Howison et al. (1991). The matching will not be described there. Following, a composite solution for the pressure distribution on the body will be presented.

The wetted length $c(t)$ is dependent on the cross-sectional geometry of the wedge and can for a given deadrise angle α be found from Wagner (1932) as

$$c(t) = 0.5\pi V t \cot \alpha. \quad (3.6)$$

In the outer flow region the pressure p_{out} on the body is approximated as

$$p_{out} - p_0 = \rho V c \frac{dc}{dt} (c^2 - y^2)^{-\frac{1}{2}} \quad \text{for } |y| < c(t). \quad (3.7)$$

The pressure on the body surface in the inner flow region p_{in} around $y = c(t)$ is found in Wagner (1932) as

$$p_{in} - p_o = 2\rho \left(\frac{dc}{dt} \right)^2 |\tau|^{\frac{1}{2}} (1 + |\tau|^{\frac{1}{2}})^{-2}, \quad (3.8)$$

where $|\tau|$ is related to y by

$$y - c = \frac{\delta}{\pi} (-\ln |\tau| - 4|\tau|^{\frac{1}{2}} - |\tau| + 5). \quad (3.9)$$

Here, δ expresses the jet thickness $\delta = \pi V^2 2c (4dc/dt)^{-2}$ and is obtained by matching the inner and outer solutions. The parameter $|\tau|$ varies from 0 to ∞ on the body surface and the maximum value of p_{in} occurs when $|\tau| = 1$, i.e. $y = c$. When $|\tau| \rightarrow 0$, $y \rightarrow \infty$ along the body on the upper side of the jet. When $|\tau| \rightarrow \infty$, $y \rightarrow -\infty$ along the body. For large values of $|\tau|$ we can then write $p_{in} - p_{out} \sim 2\rho (dc/dt)^2 |\tau|^{-\frac{1}{2}}$ and $y - c \sim -(\delta/\pi) |\tau|$. For large positive values of $c - y$ (3.8) can then be approximated as

$$p_{in} - p_{out} \sim \rho V c \frac{dc}{dt} [2c(c - y)]^{-\frac{1}{2}}. \quad (3.10)$$

By noting that p_{out} has the same asymptotic behavior when $y \rightarrow c$ as 3.10, a composite solution for the pressure distribution on the body surface for positive y values is obtained. p_{out} and p_{in} are added and the common asymptotic term is subtracted resulting in the following composite solution for $0 \leq y \leq c(t)$:

$$p - p_0 = \rho V c \frac{dc}{dt} (c^2 - y^2)^{-\frac{1}{2}} - \rho V c \frac{dc}{dt} [2c(c - y)]^{-\frac{1}{2}} + 2\rho \left(\frac{dc}{dt} \right)^2 |\tau|^{\frac{1}{2}} (1 + |\tau|^{\frac{1}{2}})^{-2}. \quad (3.11)$$

This solution has no singular behavior at $y = c(t)$. For $y > c(t)$ equation 3.8 is used.

Another solution based on matched asymptotic expansions and local jet flow analysis is provided by Watanabe (1986). However, the analysis of the jet flow and the final results provided by Watanabe (1986) are not the same as presented here by Zhao and Faltinsen (1992).

3.2 SOLUTION IN STAR-CCM+

The water entry of two-dimensional rigid wedges with constant velocity is simulated and studied in STAR. Eleven (11) different wedges with deadrise angles ranging from 4 to 81 degrees are modeled. The wedges are forced with a constant vertical velocity of 1 m/s through a calm free surface where the effect of gravity is neglected (as in Zhao and Faltinsen (1992)). A laminar flow model is considered sufficient as the water entry of a two-dimensional wedge is characterized by high local slamming pressures¹. Because the water entry is symmetric, one can assume that the fluid velocities, and thus the pressure on one side of the wedge, will be the same whether the half or the whole wedge is modeled. A half-wedge is therefore considered. Further, a body-fixed mesh is used and the vertical motion of the body is achieved by altering the level of the free surface. This is done by defining the lower boundary of the computational domain as a water inlet where the velocity inflow is set as the instantaneous wedge vertical velocity, 1 m/s. This method of simulating wedge impact has the advantage of requiring only one mesh, which can be refined in areas of interest, such as the apex of the wedge and the wall water jets expected as the wedge penetrates the water level. A high density mesh is also required at the wall region just below the water jet as this region experiences the highest slamming pressures during impact. To ensure stability in the solution a time step is chosen such that the maximum Courant number at critical regions are approximately equal to 0.5.

All simulations, with exception of the 4° wedge, are run on 2 Intel(R) Core(TM) i5 processors at 2.30 GHz. The water entry is studied for 0.06 seconds (real time), and time of each simulation varies from 20 minutes to 1 hour (depending on grid refinements and time step). The 4° wedge is run on an AMD computer cluster with a total of 12 cores, each at 2.40 Ghz. Extra computational power is needed for the 4° wedge due to the high requirements to grid size and time step. Computational time for this wedge is at 5 hours.

DISCRETIZATION OF TIME AND SPACE

When modeling the wedge water entry in STAR one needs to make some approximations. The solutions mentioned in Section 3.1 assume infinitely deep and wide fluid domain. In STAR the domain has the shape of a box, hence the effect of domain size on the results needs to be considered. Another important aspect is the effect of grid size and time step on the solution.

Domain size

Three different domain sizes are studied. The grids used are dense in the vicinity of the wedge, and stretched out farther away from the wedge (see Figure 3.5). All of the three grids have the same local refinement at the wedge apex and wall similar to that of Grid 1 in Table 3.3. The three different domain are shown in Table 3.1 below. Figure 3.2 shows the wedge in the medium size domain at the start of the simulation. For each domain the simulation is run for 0.06 s with a constant water entry velocity of 1 m/s. A wedge with deadrise angle $\alpha = 20^\circ$ is used in each simulation.

As seen from the Figure 3.3 there is minimal change in the vertical force on the wedge for the medium and large domain. For the small domain however, the vertical deviates from the other two - the deviation increasing in time. When comparing the results with

¹A turbulent versus a laminar analysis is shown later in this section.

Table 3.1: The three different domains used in the domain size analysis. The coordinates are seen in connection with Figure 3.2.

	x_{\min}	x_{\max}	z_{\min}	z_{\max}	<i>Cells</i>
Small domain	0.0	1.2	-0.3	0.7	12 994
Medium domain	0.0	3.0	-2.0	1.5	15 093
Large domain	0.0	6.0	-4.0	3.0	17 478

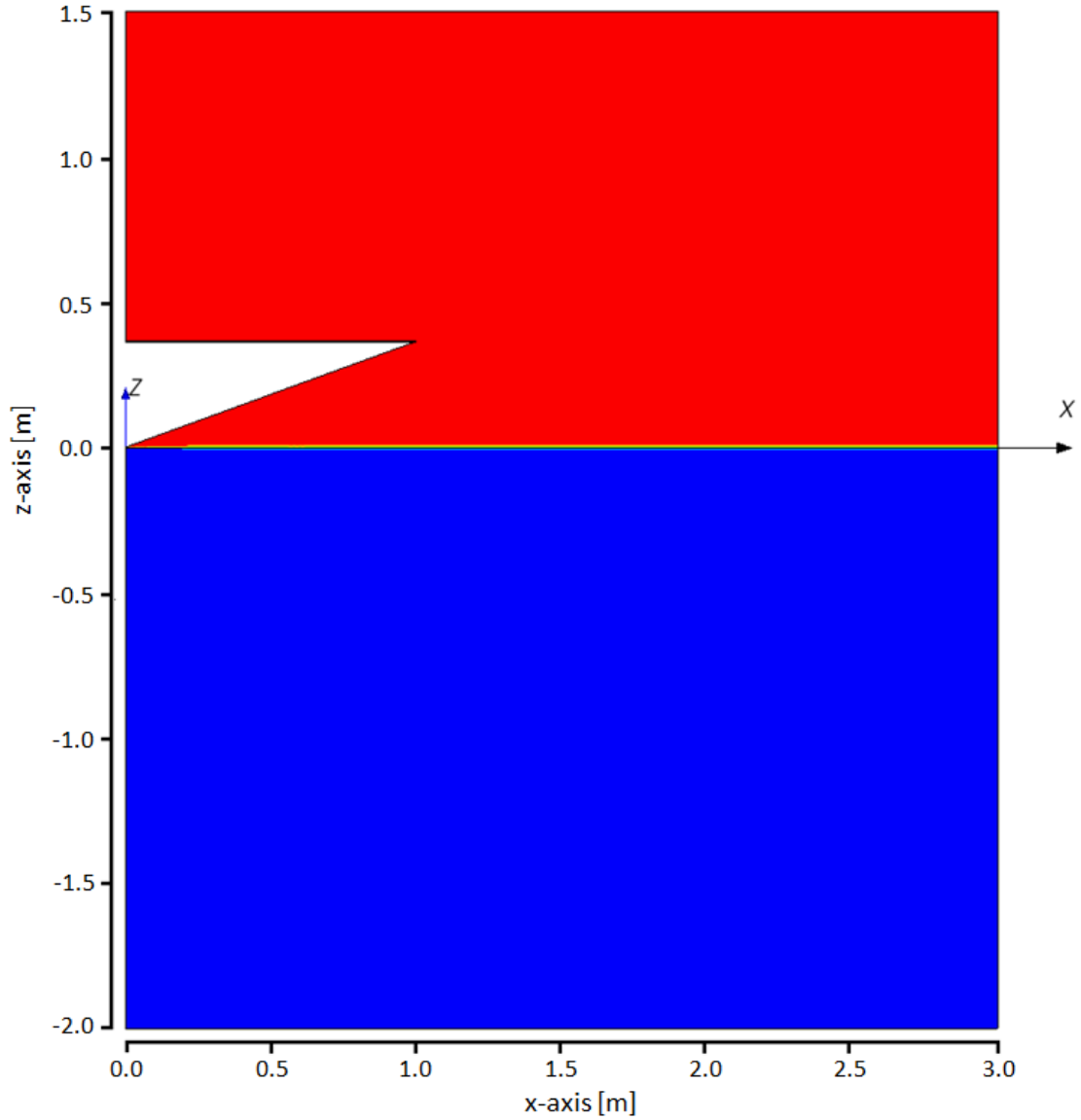


Figure 3.2: The medium size domain.

the similarity solution it is found that the small domain gives a too high value of the pressure coefficient all along the wedge bottom, as seen in Figure 3.4. The medium and large domain gives acceptable results compared to the similarity solution. A comparison of slamming parameters, the Courant number and computational time is shown in Table 3.2.

Table 3.2: The effect of domain size on the different slamming parameters: $C_{p_{\max}}$ = pressure coefficient at maximum pressure; z_{\max}/Vt = z -coordinate of maximum pressure; $\Delta S_s/c$ = spatial extent of slamming pressure; $c = 0.5\pi Vt \cot \alpha$; F_3 = total vertical hydrodynamic force on the wedge. The Courant number (CFL) and the computational time is also tabulated.

	$C_{p_{\max}}$	z_{\max}/Vt	$\Delta S_s/c$	$F_3/(\rho V^3 t)$	CFL_{\max}	Time [min]
Small domain	21.35	0.5298	0.6408	55.123	1.0865	7.4
Medium domain	18.37	0.4841	0.3834	41.799	1.0526	8.4
Large domain	18.29	0.4990	0.3738	41.317	1.0435	9.0
Similarity solution	17.77	0.5087	0.4418	42.485	-	-

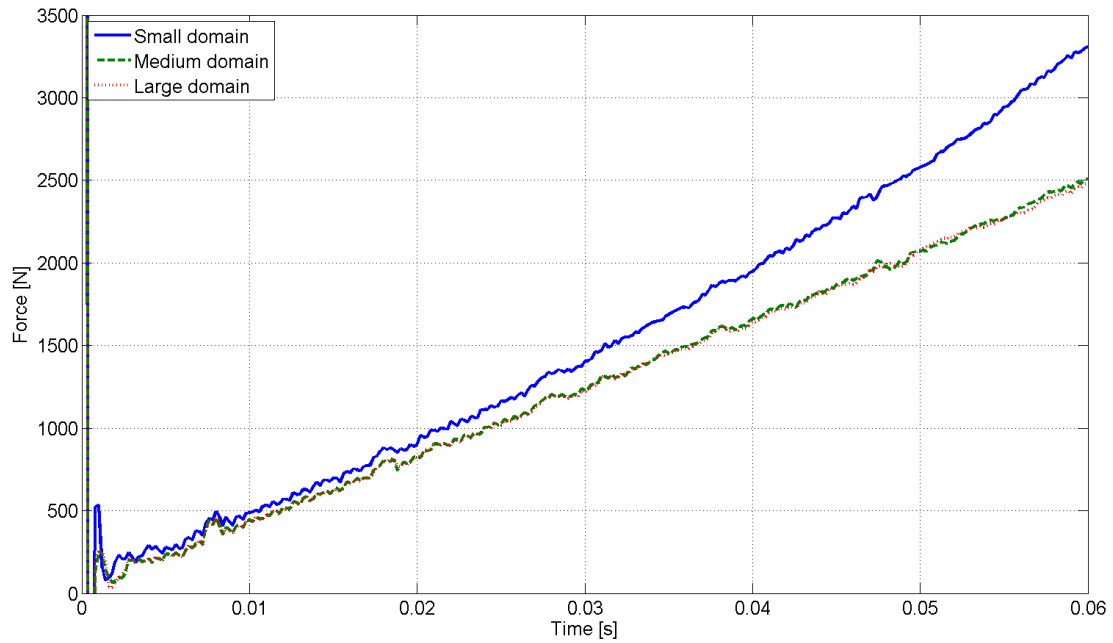


Figure 3.3: The effect of domain size on the total vertical hydrodynamic force on the wedge.

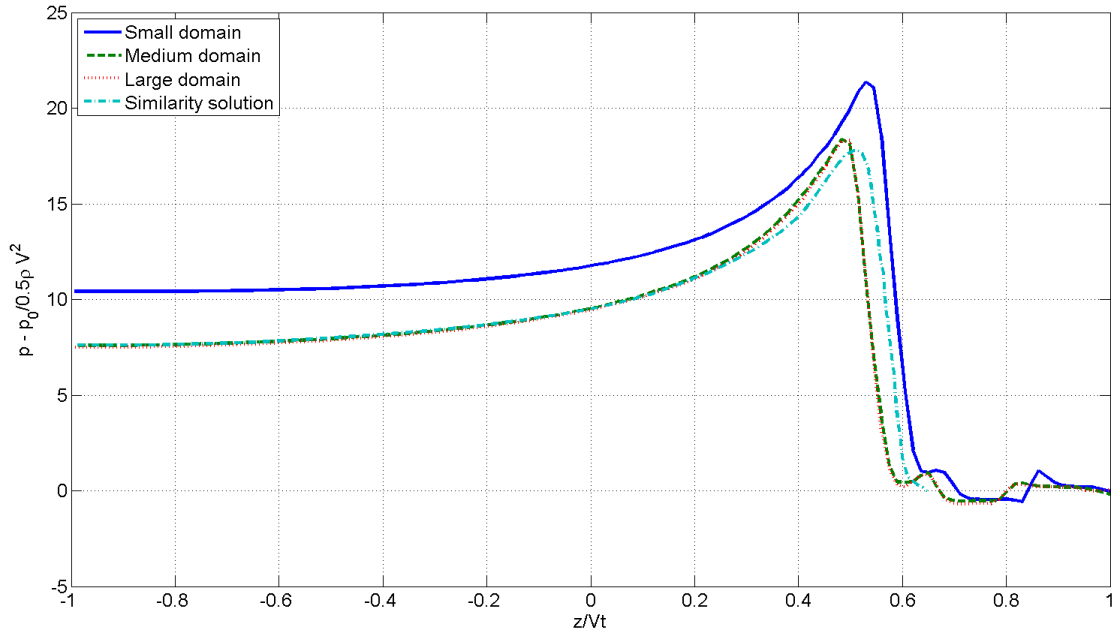


Figure 3.4: The effect of domain size on the pressure distribution along the wedge.

Grid size

When conducting CFD simulations special care must be shown when choosing the grid size. In wedge water entry analysis, slamming pressures occur short in time and space. To capture the peak pressures the grid size therefore needs to be small in the critical regions. Figure 3.5 shows a section of Grid 3 from Table 3.3. Local refinements are applied along the wedge bottom and a dense grid is chosen all along the free surface in the vertical direction.

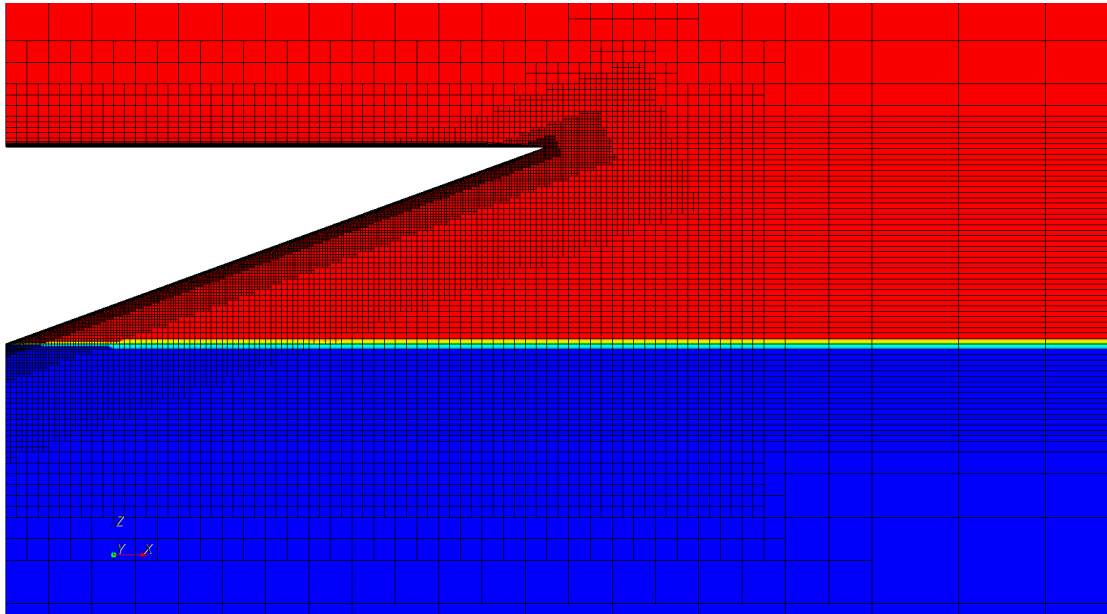


Figure 3.5: A section of Grid 3 illustrating choice of local refinements and grid size.

Four different grid sizes are studied for the wedge with deadrise angle $\alpha = 20^\circ$. The large domain from Table 3.1 is used in all simulations. For each grid size the simulation

is run for 0.06 s with a constant water entry velocity of 1 m/s. Time step is altered such to achieve stability. The properties of the four different grids are shown in Table 3.3.

Table 3.3: The four different grids used in the grid size analysis. Δx_{\min} and Δz_{\min} are dimensions of the smallest cell.

	Cells	Δx_{\min} [m]	Δz_{\min} [m]	$\frac{\Delta x_{\min}}{\Delta z_{\min}}$
Grid 1	4 404	0.00500	0.005000	1.00
Grid 2	7 379	0.00375	0.003750	1.00
Grid 3	17 478	0.00250	0.000540	4.63
Grid 4	61 751	0.00125	0.000274	4.56

As the number of cells in the grid is increased, the accuracy of the prediction of pressure along the wedge increase. It must be noted that this increase in accuracy is accompanied by an increase in computational time. By studying Figure 3.7 it is seen that all grids, with exception of Grid 1, gives reasonable values of the pressure distribution along the wedge bottom. It is noticed that Grid 2 is only able to capture a few data points at the peak pressure, and should therefore not be used in further analysis. Grid 3, giving a smooth pressure distribution including a conservative value of $C_{p_{\max}}$, is concluded sufficient for further studies. By studying Figure 3.6 it is also seen that Grid 3 has the grid resolution resulting in the most stable force signal. A comparison of slamming parameters, the Courant number and computational time from the grid size study is shown in Table 3.4

Table 3.4: The effect of grid size on the different slamming parameters: $C_{p_{\max}}$ = pressure coefficient at maximum pressure; z_{\max}/Vt = z -coordinate of maximum pressure; $\Delta S_s/c$ = spatial extent of slamming pressure; $c = 0.5\pi Vt \cot \alpha$; F_3 = total vertical hydrodynamic force on the wedge. The Courant number (CFL) and the computational time is also tabulated.

	$C_{p_{\max}}$	z_{\max}/Vt	$\Delta S_s/c$	$F_3/(\rho V^3 t)$	CFL_{\max}	Time [min]
Grid 1	14.47	0.4865	-	40.426	1.2117	1.0
Grid 2	18.29	0.4786	0.4345	43.485	0.9726	2.3
Grid 3	18.54	0.4841	0.3546	41.933	1.0556	10
Grid 4	17.16	0.4835	0.5824	43.887	0.7496	40
Similarity solution	17.77	0.5087	0.4418	42.485	-	-

Time step

When changing the grid size one must also make sure that the time step is chosen such that stability is conserved. A too high time step will make the solver "jump" cells, causing an unstable solution.

For the two-dimensional case, no systematic study on choice of time step is performed. The time step is in all simulations chosen such that the Courant-condition is satisfied. A study on the time step's effect on predicted slamming pressures are shown in section 4.2 in Chapter 4.

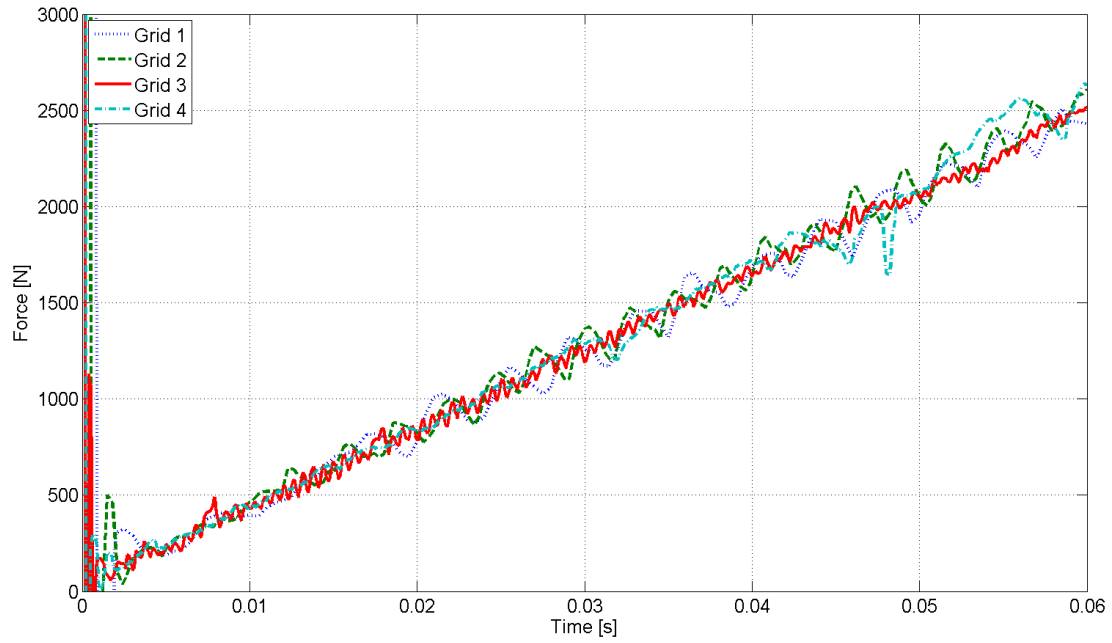


Figure 3.6: The effect of grid size on the total vertical hydrodynamic force on the wedge.

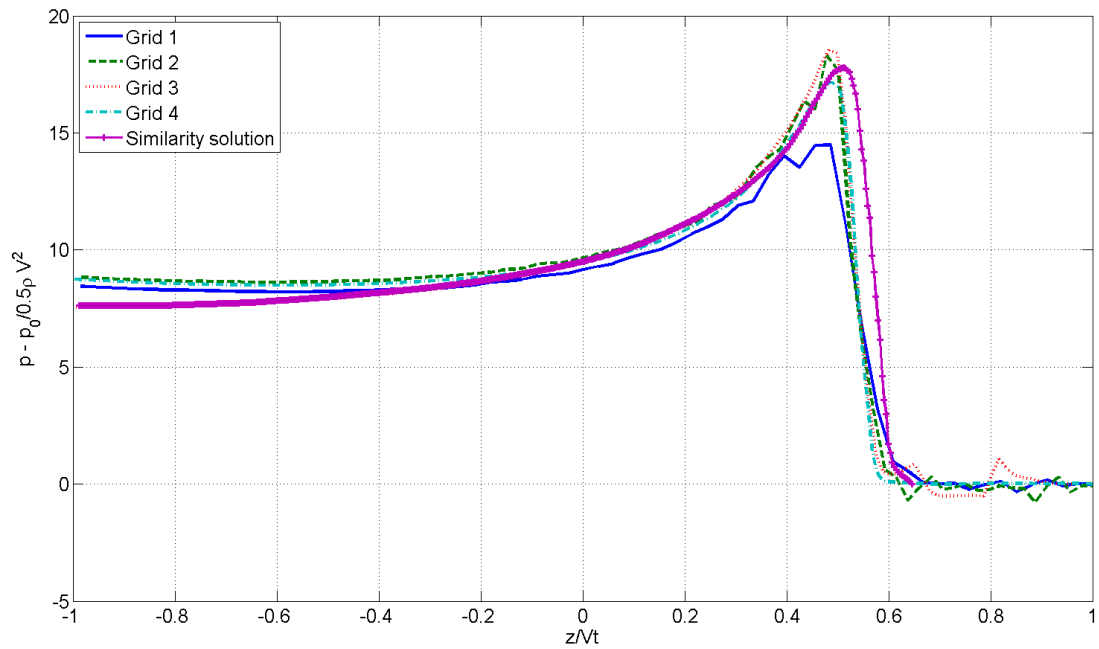


Figure 3.7: The effect of grid size on the pressure distribution along the wedge.

LAMINAR VERSUS TURBULENT FLOW

When studying fluid-body interaction one needs to determine the type of flow around the body. For a typical small wedge slam the flow along the wedge will be viscous. The typical Reynolds number for wedge entry, calculated from data presented by Yettou et al. (2006), is $6E^6$. This implies that the effect of turbulence on the wedge has to be taken into account, hence a suitable turbulence model has to be used when performing CFD calculations. However, forces imposed on the wedge at impact is mainly due to the high slamming pressure and it is therefore discussed whether or not a laminar model can be applied when studying these types of water entry problems.

To investigate the dependence of flow model on the solution two different turbulence models are chosen to close the Navier-Stokes equations: the $k-\varepsilon$ model and the $k-\omega$ model. The two approaches are compared with the similarity solution and the laminar solution from Grid 3 in Table 3.4. All three solutions have the same domain size, grid size and time step, and each simulation is run for 0.06 s with a constant water entry velocity of 1 m/s. A wedge with deadrise angle $\alpha = 20^\circ$ is used. A comparison of slamming parameters, the Courant number, the Wall $y+$ value and computational time from flow model study is shown in Table 3.5.

Table 3.5: The effect of choice of flow model on the different slamming parameters: $C_{p_{\max}}$ = pressure coefficient at maximum pressure; z_{\max}/Vt = z -coordinate of maximum pressure; $\Delta S_s/c$ = spatial extent of slamming pressure; $c = 0.5\pi Vt \cot \alpha$; F_3 = total vertical hydrodynamic force on the wedge. The Courant number (CFL), the Wall $y+$ value and the computational time is also tabulated.

	$C_{p_{\max}}$	z_{\max}/Vt	$\Delta S_s/c$	$F_3/(\rho V^3 t)$	CFL_{\max}	Wall $y+$	Time [min]
$k-\varepsilon$ model	18.50	0.4990	0.3547	41.3698	1.0384	109.85	12.5
$k-\omega$ model	18.74	0.4990	0.3451	41.3912	1.1543	109.72	18.5
Laminar model	18.54	0.4841	0.3546	41.933	1.0556	-	10.0
Simil. solution	17.77	0.5087	0.4418	42.485	-	-	-

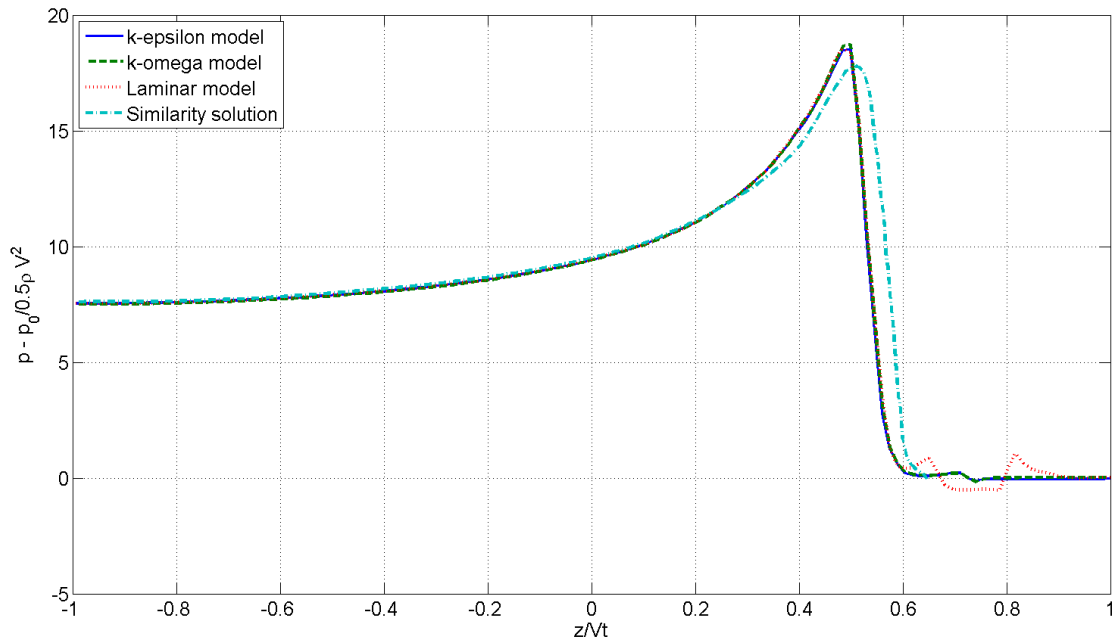


Figure 3.8: The effect of choice of flow model on the pressure distribution along the wedge.

By studying Figure 3.8 it is noticed that for the two-dimensional water entry problem a laminar or turbulent flow model gives fairly the exact same solution on the pressure distribution along the wedge. A laminar flow model is therefore applied in all simulation studied in this chapter.

INFLUENCE OF NUMERICAL PARAMETERS

When setting up a CFD simulation in STAR a number of input parameters needs to be chosen. The default values are not always the most fitting, and a study has to be performed to obtain the most satisfactory result. Satisfactory results are in this context referred to results which coincides as much as possible to those of Zhao and Faltinsen (1992) presented in section 3.1.

It is difficult to determine the effect of varying the input parameters if several input parameters are varied at the same time. The study is performed by altering different parameters, one at a time, and noting the effect on the result. In each simulation the wedge with deadrise angle $\alpha = 20^\circ$ is run for 0.06 s with a constant water entry velocity of 1 m/s. The large domain together with Grid 3 are applied. The study is ended when the input parameters which provided the most satisfactory results are found. These values are then applied to all wedges in all the simulations.

One of the input parameters which is seen to influence the solution is the *Under-Relaxation Factor* (URF). This parameter is discussed in further detail for the three-dimensional case in Chapter 4. For the two-dimensional case, however, it should be noted that the under-relaxation for velocities and pressure are set to 0.9 and 0.4, respectively; the default values are too conservative for steady-state flow. In Table 3.6, a selection of parameters tested in the convergence study are listed. Further study of the set-up and simulations can be done on the *.sim* files found in the folder *wedge2D_constvel* found in the attached ZIP-file. Peric (2012)

Table 3.6: Parameters tested in the convergence study for the two-dimensional wedge. The final chosen values are also included.

	Parameter	Tested	Chosen
<i>Physics</i>			
Segregated Flow	Convection	1st-/2nd-order	2nd-order
<i>Solver</i>			
Implicit Unsteady	Temporal Discretization	1st-/2nd-order	2nd-order
Segregated Flow	Under-Relaxation: Velocity	0.6, 0.7, 0.8, 0.9	0.9
Segregated Flow	Under-Relaxation: Pressure	0.1, 0.2, 0.3, 0.4	0.4
<i>Stopping Criteria</i>			
Iterations	Number of Inner Iterations	5,8,10,15,20	20

ANALYZING AND POST PROCESSING

By the use of *field functions* in STAR-CCM+, raw simulation data can be accessed making it possible to analyze the solution while the simulation is running. The analysis is performed by creating reports, plotting sets of data and visualizing the solution data. This is used to easily confirm that the simulation is set up correctly and that values of interest are within reasonable limits. In the wedge water entry analysis, all of the three tools were used to monitor the following:

- **VOF:** used to visualize the fluid-body interaction to confirm that the physical model is realistic. Figure 3.9.
- **Pressure:** to confirm that the pressure values are within reasonable limits and that the pressure distribution is realistic. Figure 3.10.
- **Velocity:** as with pressure. From equation 2.1 in section 2.1 (Chapter 2), velocities are also used to calculate the CFL-value. By this, the time step in the simulation is adjusted. Figure 3.11.
- **CFL-value:** STAR's own *convective courant number* is used to verify the CFL-value. Figure 3.12.
- **Force:** to determine the total vertical hydrodynamic force on the wedge. Figure 3.13.
- **Residuals:** to study the convergence and stability of the solution and to set the time step and inner iterations accordingly. Figure 3.14.

Figure 3.9 to 3.14 shows plots and visualization for the water entry 0.06 s after wedge impact for the wedge with deadrise angle $\alpha = 20^\circ$ and velocity equal to 1 m/s.

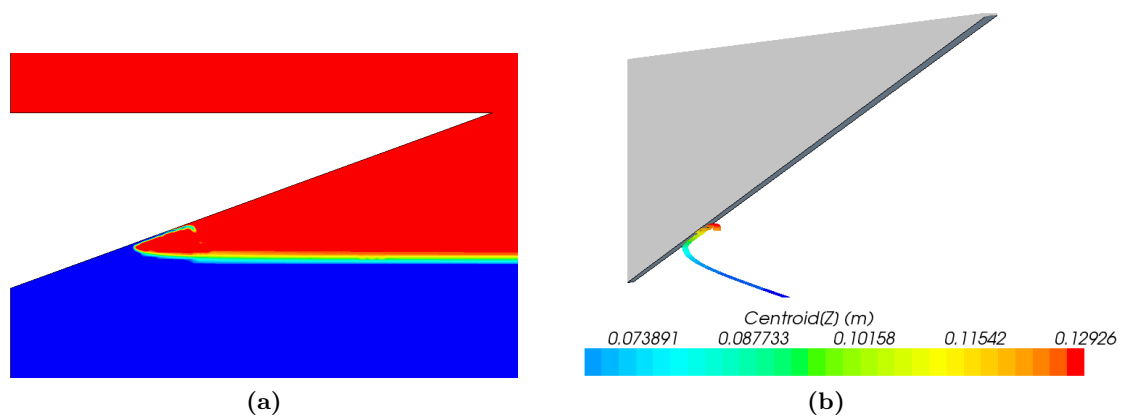


Figure 3.9: Visualization (a)-(b) of the water rise-up along the wedge section at $t = 0.06s$.

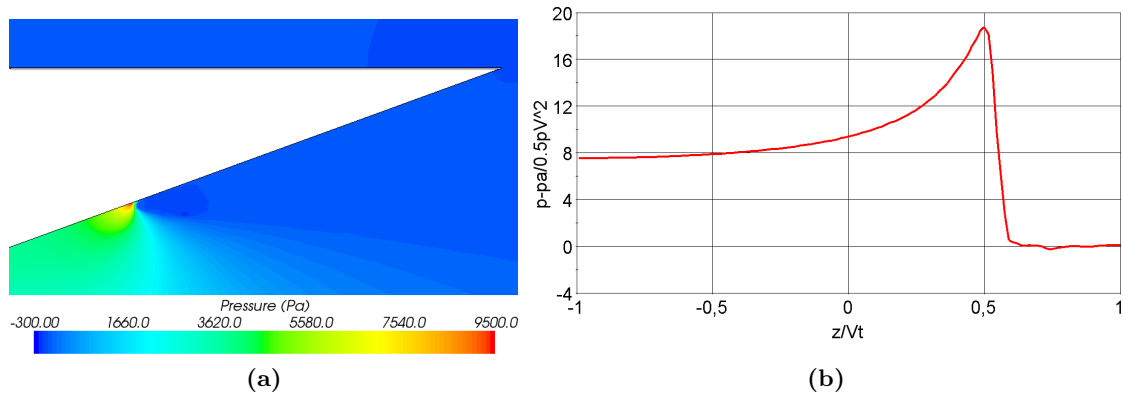


Figure 3.10: Pressure distribution (a) and normalized pressure distribution (b) along the wedge at $t = 0.06s$.

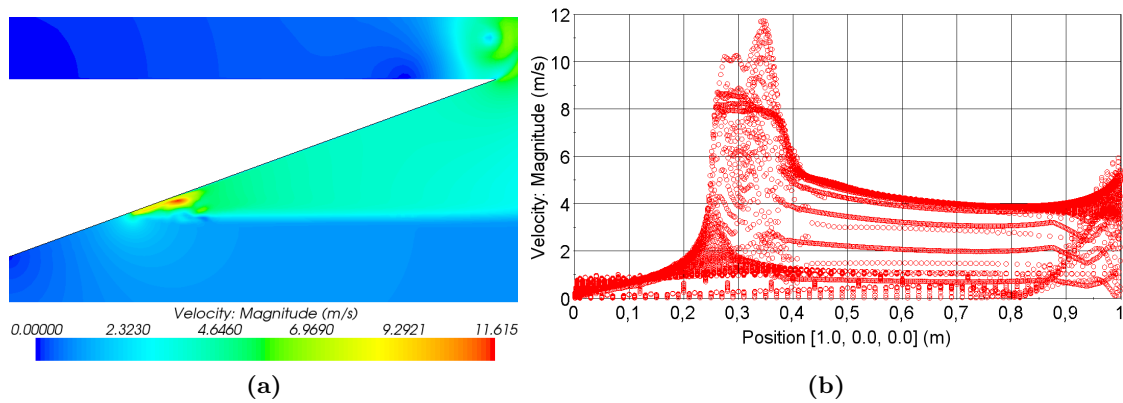


Figure 3.11: Visualization (a) and plot (b) of the velocity distribution along the wedge at $t = 0.06s$.

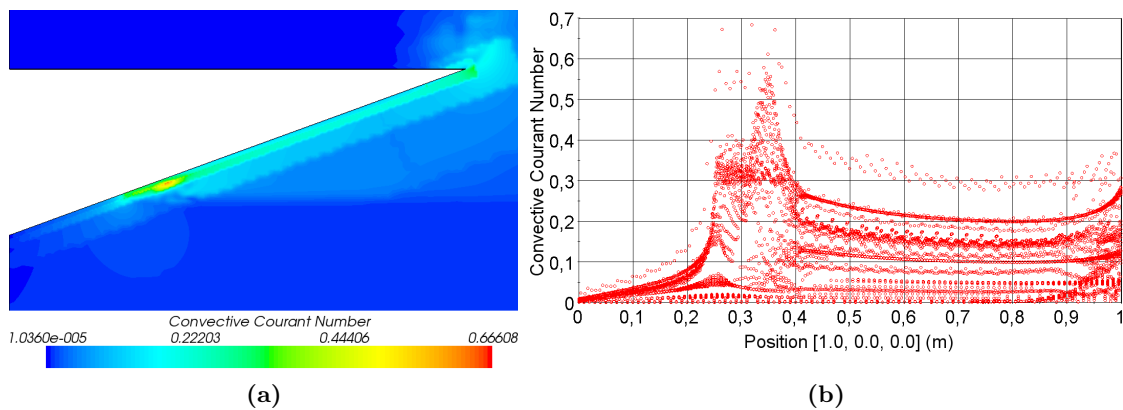


Figure 3.12: Visualization (a) and plot (b) of the CFL-values along the wedge at $t = 0.06s$.

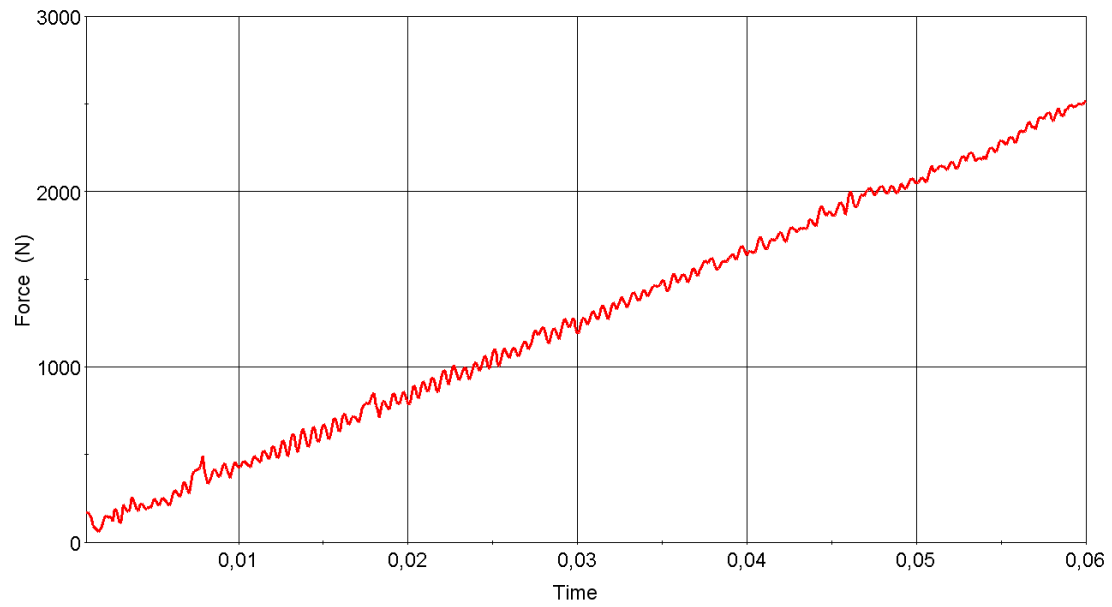


Figure 3.13: Total vertical hydrodynamic force on the wedge.

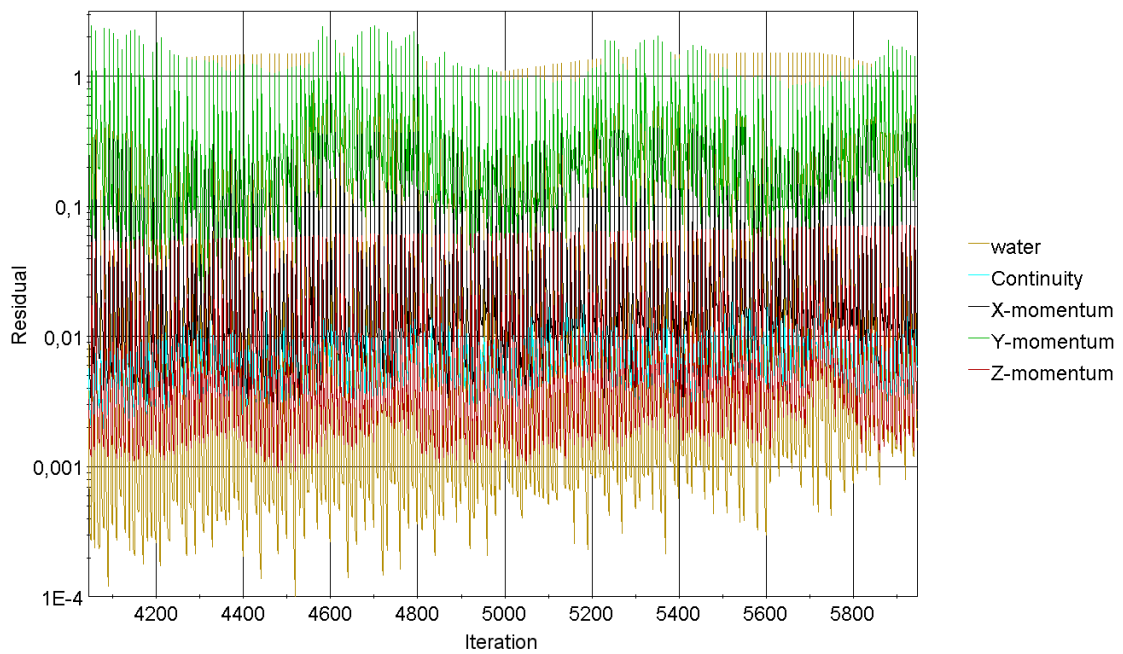


Figure 3.14: The residuals of water, continuity and x, y and z-momentum at the end of the simulation.

3.3 RESULTS

From the domain size study it is found that both the medium and the large domain gives steady results for the force signal. The computational time is approximately the same and the large domain is therefore chosen for all the simulations. Grid 3 proves to give the most favorable solution for the wedge with deadrise angle $\alpha = 20^\circ$ and is chosen for all simulations with exception of the wedge with deadrise angle $\alpha = 4^\circ$. Here a finer grid is used to capture the pressure peak. As there is found little difference in the results by use of flow model, a laminar model is applied to simplify the solution. A time step ranging from $1E^{-4}$ to $2E^{-4}$ is used depending on the CFL condition. The free surface at $t = 0.06$ is inspected to ensure that a reasonable sharp interface is predicted with a rapid variation of volume fraction across 2-3 cells only (see Figure 3.15).

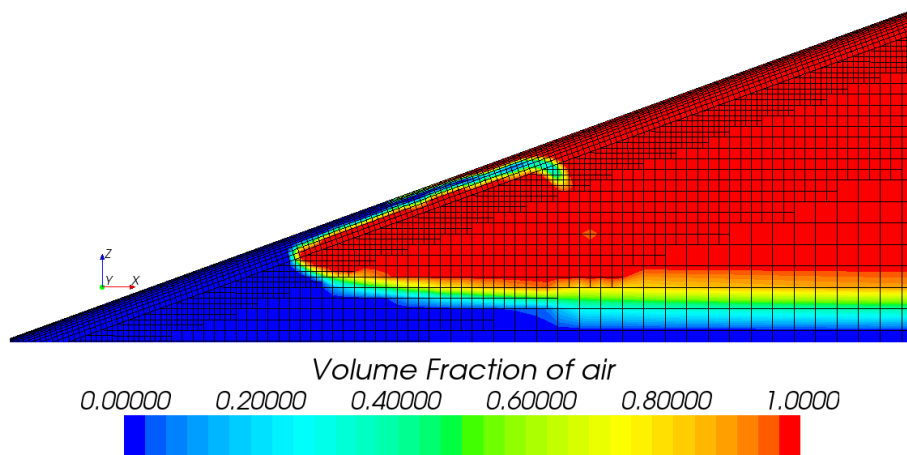


Figure 3.15: The free surface at $t = 0.06$ s after wedge impact showing an acceptable prediction of the volume fraction between water and air.

In the analysis, four different slamming parameters are studied at $t = 0.06$ s after impact: the maximum pressure coefficient $C_{p_{\max}} = (p_{\max} - p_a) / (0.5\rho V^2)$, describing the pressure along the wedge; z_{\max}/Vt , a dimensionless expression for the position on the wedge of the maximum pressure; $\Delta S_s/c$, the dimensionless spatial extent of the slamming pressure; $F_3/(\rho V^3 t)$, dimensionless total hydrodynamic force on the wedge. The definitions of the slamming parameters are presented in Figure 3.16.

The spatial extent ΔS_s of the slamming pressure peak can only be calculated for small deadrise angles where there is a significant peak in the pressure. In this case for $\alpha \leq 20^\circ$. The total hydrodynamic force is calculated for the half-wedge and the result is multiplied by a factor of 2 to obtain the force on the whole wedge. Results obtained by STAR-CCM+ are presented in Table 3.7 and 3.8 and Figures 3.18 to 3.27.

By studying Table 3.8 and Figures 3.17 to 3.27 a good agreement is seen between the STAR results and the results presented by Zhao and Faltinsen. Some deviation in the STAR solution is seen in the plots in the Figures 3.17 to 3.27 for $z/Vt \approx 0.6$ (especially for $\alpha = 4^\circ$ seen in Figure 3.17). These deviations are due to the flapping of the jet of water that moves along the wedge wall. In 2-D, there is no flow in the third direction so when the jet tends to move away from the wall an under pressure is created. These oscillations, however, do not affect the rest of the solution and can therefore be ignored. Further, by studying Figure 3.20 to Figure 3.23, a discrepancy between the asymptotic solution and the other three solutions are seen.

This discrepancy follows from the fact that the asymptotic solution assumes small deadrise angles, $\alpha < 10^\circ$. Faltinsen (2012), Peric (2012)

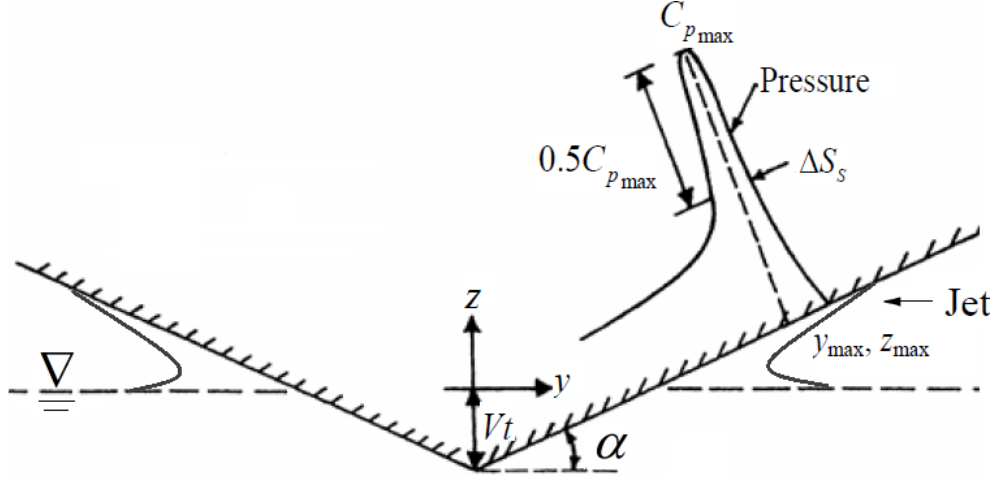


Figure 3.16: Definition of parameters characterizing slamming pressure during water entry of a blunt two-dimensional body: α = deadrise angle; $C_{p_{\max}}$ = pressure coefficient at maximum pressure; z_{\max} = z -coordinate of maximum pressure; ΔS_s = spatial extent of slamming pressure exceeding 50% of maximum pressure; t = time; V = water entry velocity. Zhao and Faltinsen (1992)

Table 3.7: Estimation of slamming parameters by STAR-CCM+ during water entry of a wedge with constant vertical velocity V : α = deadrise angle; $C_{p_{\max}}$ = pressure coefficient at maximum pressure; z_{\max}/Vt = z -coordinate of maximum pressure; $\Delta S_s/c$ = spatial extent of slamming pressure; $c = 0.5\pi Vt \cot \alpha$; F_3 = total vertical hydrodynamic force on the wedge.

α (deg.)	$C_{p_{\max}}$	z_{\max}/Vt	$\Delta S_s/c$	$F_3/(\rho V^3 t)$
4	546.300	0.5792	0.0158	1508.33
7.5	137.651	0.5440	0.0524	382.64
10	80.253	0.5378	0.0842	207.12
15	34.831	0.5190	0.1701	83.33
20	18.761	0.4990	0.3451	41.93
25	11.031	0.4735	-	23.88
30	6.842	0.4378	-	13.81
40	3.397	0.2576	-	5.54
45	2.637	-0.9867	-	3.50
60	1.655	-0.9774	-	0.91
81	0.593	-0.9796	-	0.033

Table 3.8: Estimation of slamming parameters by the similarity solution, the asymptotic method, the nonlinear boundary element method and STAR-CCM+ during water entry of a wedge with constant vertical velocity V : α = deadrise angle; $C_{p_{\max}}$ = pressure coefficient at maximum pressure; z_{\max}/Vt = z -coordinate of maximum pressure; $\Delta S_s/c$ = spatial extent of slamming pressure; $c = 0.5\pi Vt \cot \alpha$; F_3 = total vertical hydrodynamic force on the wedge.

α (deg.)	$C_{p_{\max}}$				z_{\max}/Vt			
	Simil.	Asymp.	BEM	STAR	Simil.	Asymp.	BEM	STAR
4	503.030	504.61	521.4	546.300	0.5695	0.5708	0.571	0.5792
7.5	140.587	142.36	148.3	137.651	0.5623	0.5708	0.558	0.5440
10	77.847	79.36	80.2	80.253	0.5556	0.5708	0.555	0.5378
15	33.271	34.37	32.8	34.831	0.5361	0.5708	0.533	0.5190
20	17.774	18.63	18.2	18.761	0.5087	0.5708	0.488	0.4990
25	10.691	11.35	10.9	11.031	0.4709	0.5708	0.443	0.4735
30	6.927	7.40	6.94	6.842	0.4243	0.5708	0.400	0.4378
40	3.266	3.50	3.26	3.397	0.2866	0.5708	0.245	0.2576

α (deg.)	$\Delta S_s/c$				$F_3/(\rho V^3 t)$			
	Simil.	Asymp.	BEM	STAR	Simil.	Asymp.	BEM	STAR
4	0.01499	0.01576	0.0156	0.0158	1503.638	1540.506	1491.8	1508.33
7.5	0.05129	0.05586	0.0526	0.0524	399.816	423.735	417.9	382.64
10	0.09088	0.1002	0.0941	0.0842	213.980	231.973	220.8	207.12
15	0.2136	0.2314	0.226	0.1701	85.522	96.879	85.5	83.33
20	0.4418	0.4270	0.434	0.3451	42.485	50.639	43.0	41.93
25	-	-	-	-	23.657	29.765	23.7	23.88
30	-	-	-	-	14.139	18.747	13.9	13.81
40	-	-	-	-	5.477	8.322	5.31	5.54

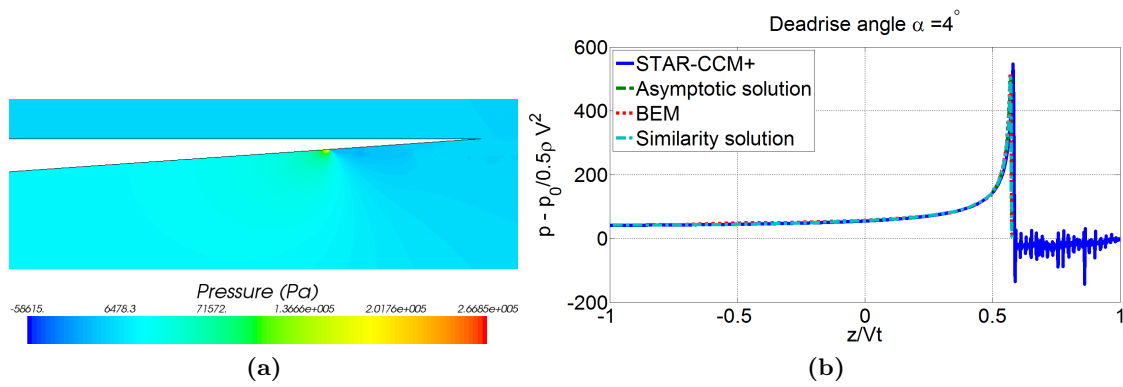


Figure 3.17: Pressure distribution (a) and normalized pressure distribution (b) along the wedge at $t = 0.06s$; deadrise angle $\alpha = 4^\circ$; $V = 1 m/s$.

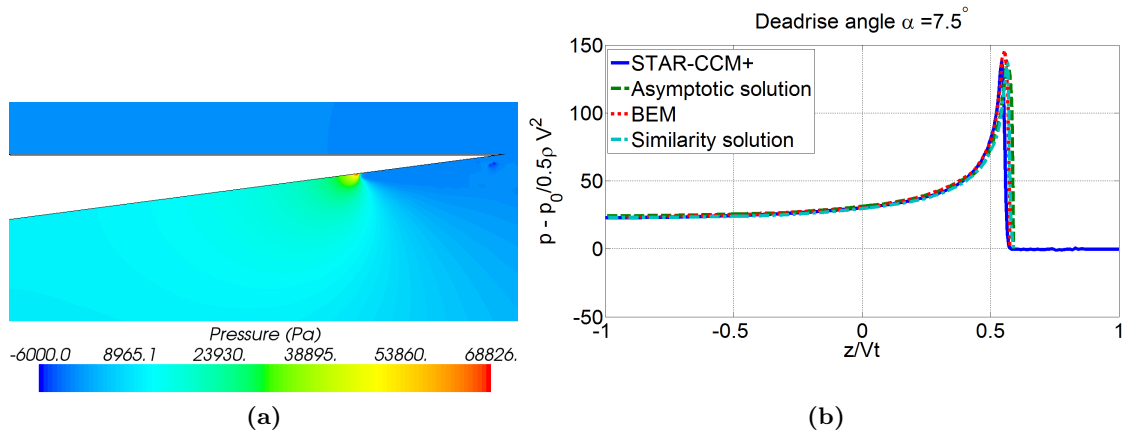


Figure 3.18: Pressure distribution (a) and normalized pressure distribution (b) along the wedge at $t = 0.06s$; deadrise angle $\alpha = 7.5^\circ$; $V = 1 m/s$.

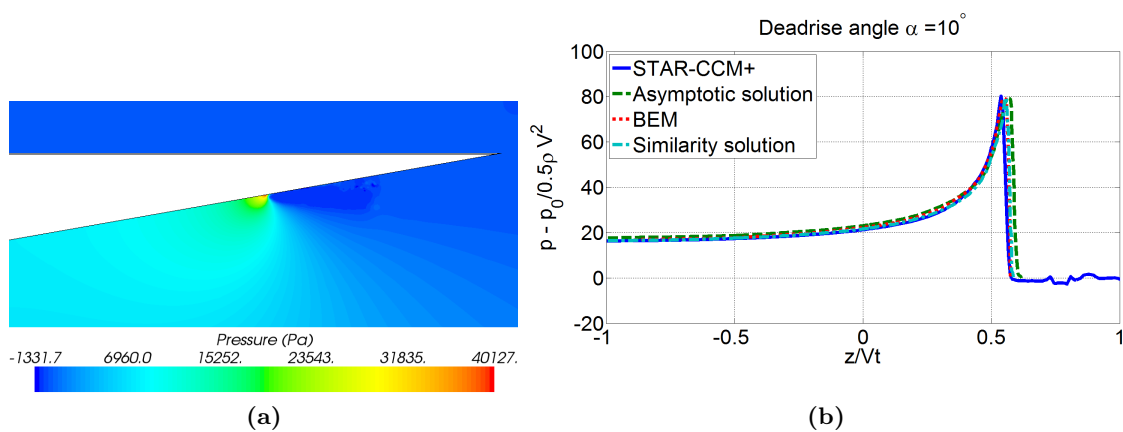


Figure 3.19: Pressure distribution (a) and normalized pressure distribution (b) along the wedge at $t = 0.06s$; deadrise angle $\alpha = 10^\circ$; $V = 1 m/s$.

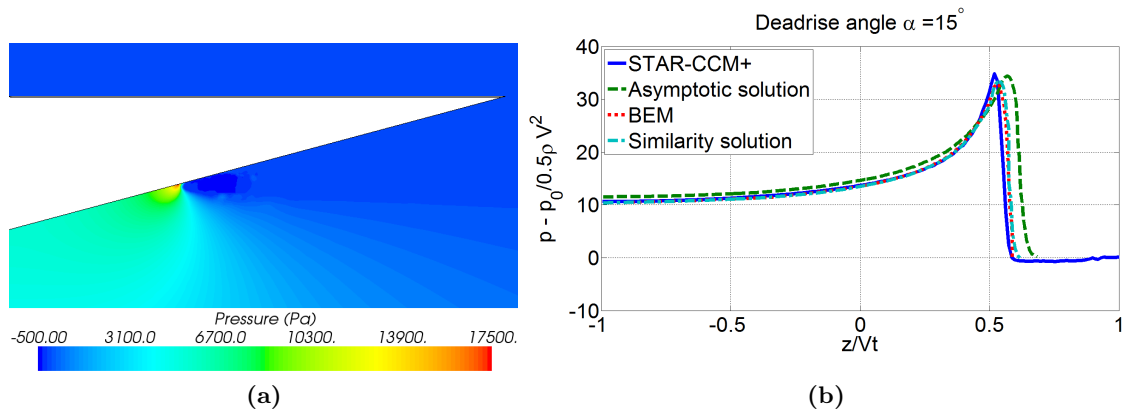


Figure 3.20: Pressure distribution (a) and normalized pressure distribution (b) along the wedge at $t = 0.06s$; deadrise angle $\alpha = 15^\circ$; $V = 1 m/s$.

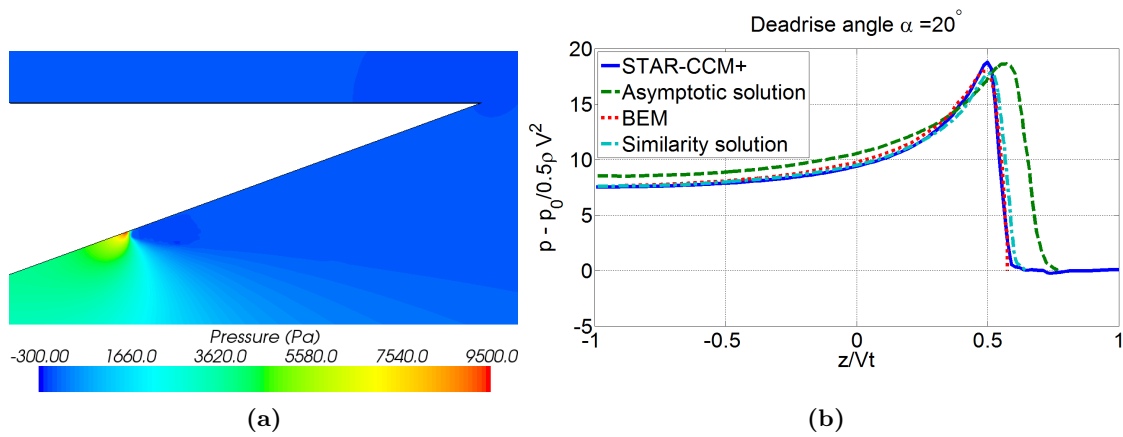


Figure 3.21: Pressure distribution (a) and normalized pressure distribution (b) along the wedge at $t = 0.06s$; deadrise angle $\alpha = 20^\circ$; $V = 1 m/s$.

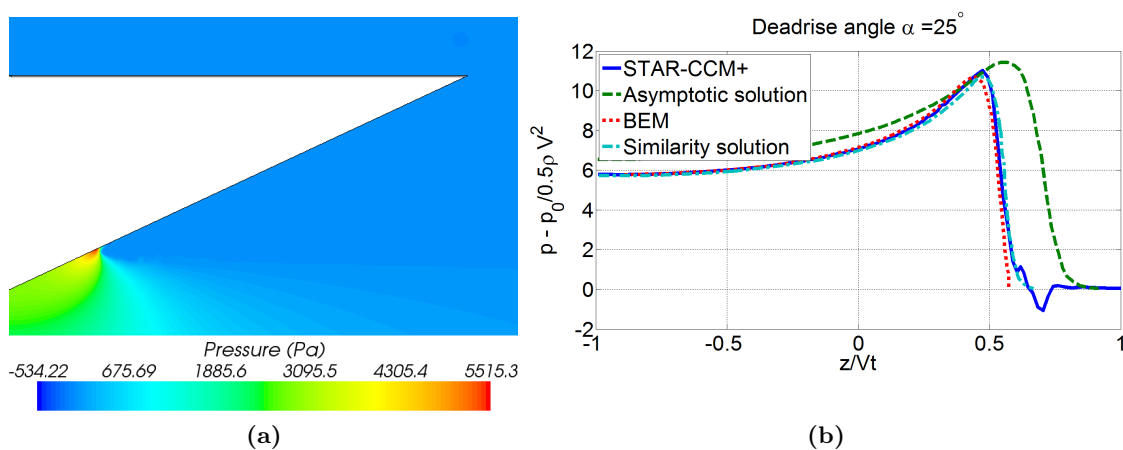


Figure 3.22: Pressure distribution (a) and normalized pressure distribution (b) along the wedge at $t = 0.06s$; deadrise angle $\alpha = 25^\circ$; $V = 1 m/s$.

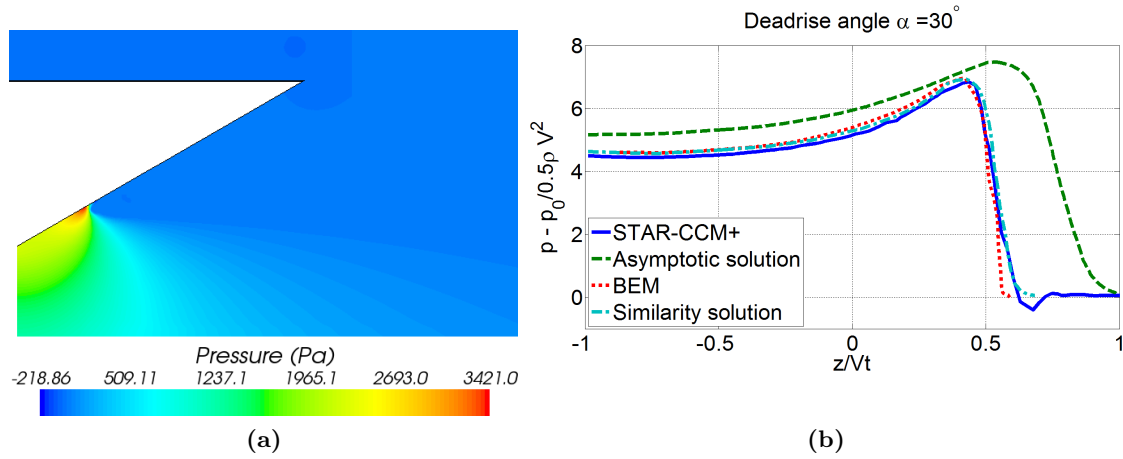


Figure 3.23: Pressure distribution (a) and normalized pressure distribution (b) along the wedge at $t = 0.06s$; deadrise angle $\alpha = 30^\circ$; $V = 1 m/s$.

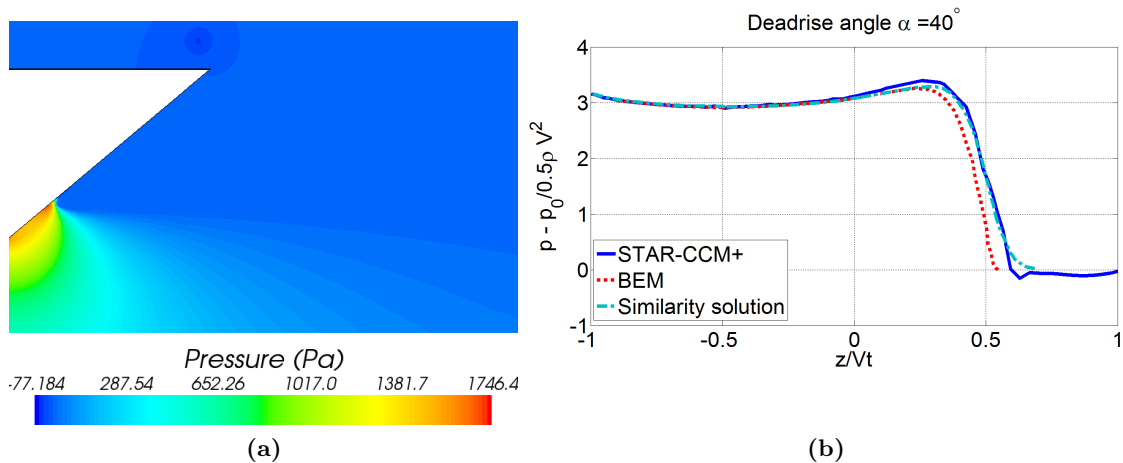


Figure 3.24: Pressure distribution (a) and normalized pressure distribution (b) along the wedge at $t = 0.06s$; deadrise angle $\alpha = 40^\circ$; $V = 1 m/s$.

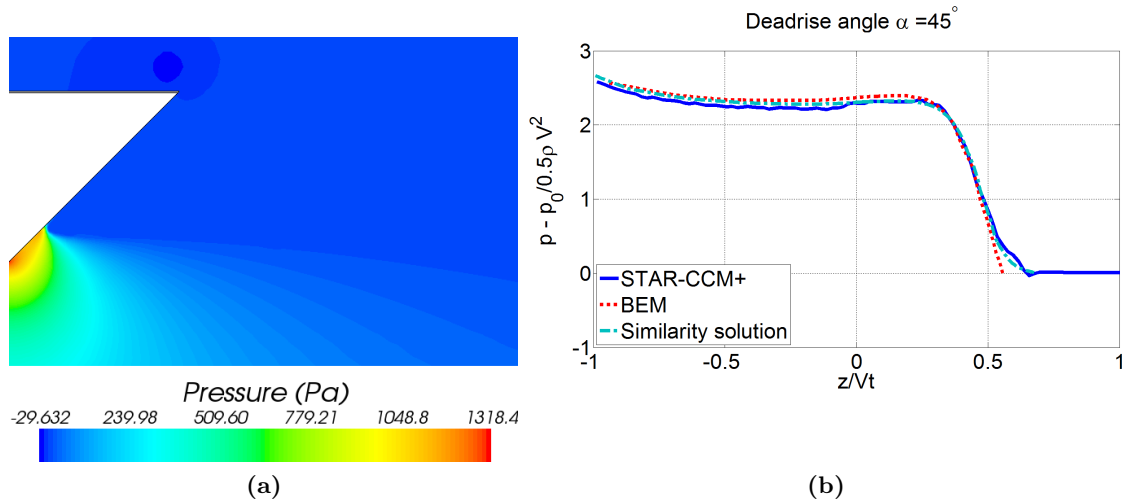


Figure 3.25: Pressure distribution (a) and normalized pressure distribution (b) along the wedge at $t = 0.06s$; deadrise angle $\alpha = 45^\circ$: $V = 1 m/s$.

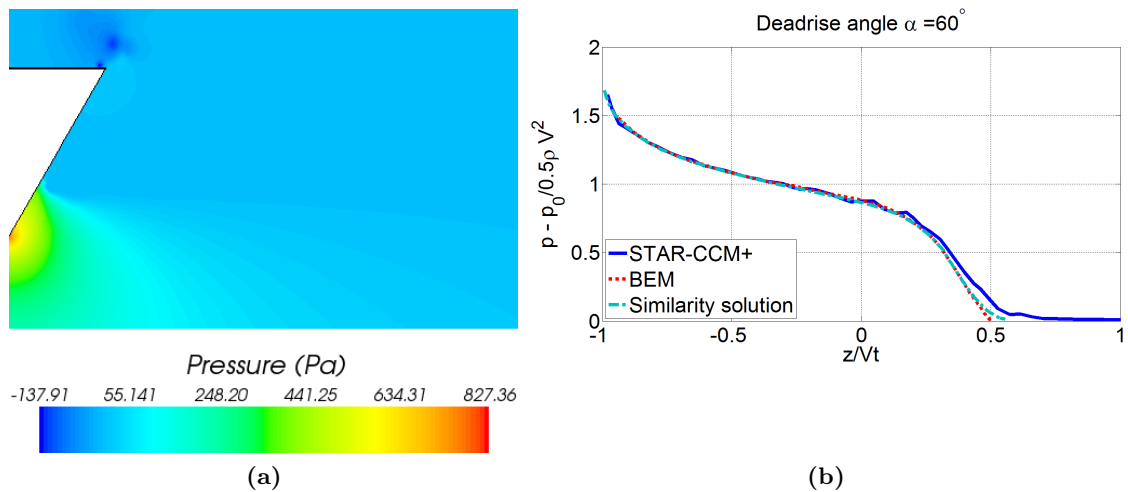


Figure 3.26: Pressure distribution (a) and normalized pressure distribution (b) along the wedge at $t = 0.06s$; deadrise angle $\alpha = 60^\circ$: $V = 1 m/s$.

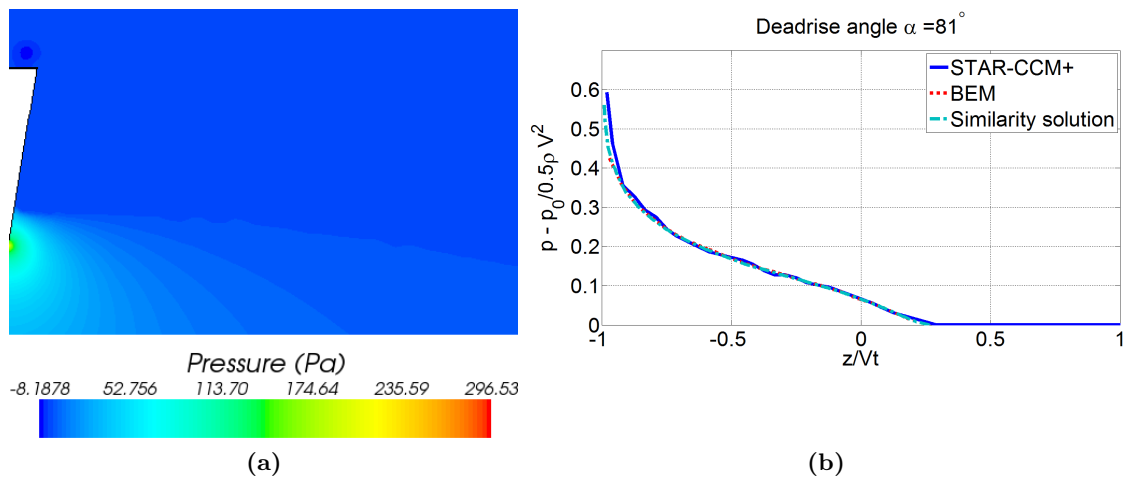


Figure 3.27: Pressure distribution (a) and normalized pressure distribution (b) along the wedge at $t = 0.06s$; deadrise angle $\alpha = 81^\circ$; $V = 1 m/s$.

WATER ENTRY OF A THREE-DIMENSIONAL WEDGE

Fluid - structure impact problems associated with water entry have important applications in various aspects of naval architecture and ocean engineering, including slamming of a ship, green water on deck and wave impact on offshore platforms and coastal structures. Ships that navigate through rough waters suffer various structural damages that are generally related to waves rapidly slamming into the ship's bow, side or/and stern. Recently, recreational boats and high speed watercrafts have been introduced to the market and have become extremely popular. When these boats repeatedly jump waves, the impact loads creates significant pressure on the hull.

As a consequence of the above mentioned scenarios, manufactures all over the world are searching for simple and accurate approaches to estimate the pressure loading that occur due to the effect of slamming. Von Karman (1929) was one of the pioneer researchers in this field. In his study, he developed a theoretical model based on the momentum theorem and the water-added mass.

Besides Von Karman (1929), several other individuals have spent much time studying the fluid - structure slamming phenomena. Worth mentioning are Wagner (1932), Dobrovolskaya (1969), Payne (1988), Korobkin and Pokhnachov (1988) and Zhao and Faltinsen (1992). (Dobrovolskaya (1969) and Zhao and Faltinsen (1992) are described in section 3.1 in Chapter 3.)

This chapter will focus on the use of STAR-CCM+ to study the water entry of a free-falling three-dimensional rigid wedge, much resembling the hull cross-section of a high-speed watercraft. The numerical results produced in STAR are compared with an experimental study conducted by Yettou et al. (2006), together with constant water entry velocity models by Wagner (1932), Von Karman (1929), Mei (1998) and Zhao et al. (1996).

4.1 DESCRIPTION OF THE EXPERIMENT

Yettou et al. (2006) performed experimental studies on free-falling three-dimensional wedges with deadrise angles α varying from 15° to 35° . Each wedge was dropped from two different drop heights, 1 m and 1.3 m, and for each deadrise angle four different masses were applied. For comparison to the numerical solution in STAR, only one of these configurations is modeled: a wedge dropping from 1.3 m with a total mass of 94 kg and deadrise angle α equal 25° .

SET-UP

Figure 4.1 illustrates the experimental set-up. A vertical mast is fixed to bottom of a water channel 1 m deep, 2 m wide and 30 m long. The wedge is attached to a steel guiding structure that slides downwards along the mast. As seen in Figure 4.1 and 4.2, the wedge apex is aligned perpendicular to the longitudinal axis of the basin.

The wedge is constructed by 19 mm thick plywood with a square top section of 1.2 m \times 1.2 m, shown in Figure 4.2. The walls are waterproof and assumed rigid.

INSTRUMENTATION AND DATA ACQUISITION

The time-varying pressure distribution on one side of the three-dimensional wedge is captured by using twelve Wheatstone bridge AB/HP Data Instruments pressure transducers. Each transducer has a diameter of 19 mm and a pressure range of 0-3.45E6 Pa. As seen in Figure 4.3, the transducers are distributed along the median of one side of the wedge and the distance between the center of each transducer is 50 mm. Their numbers are 1-12, number 1 being located closest to the wedge apex. The first natural frequency of the transducer is 10 kHz.

To measure the instantaneous position and velocity of the wedge, a potentiometric cable extension transducer Celesco model PT5A100S47FR1KM6 is used. The transducer position raw data is low-pass filtered using a cut-off 45 Hz to remove spurious noise generated by slight vibrations of the cable. The velocity is calculated by a numerical differentiation of the position signal.

Data acquisition is performed using a 16-channel data acquisition system model eDAQ manufactured by Somat Inc. Two 8-channel low-level boards dedicated to the measurement of Wheatstone bridges are used. Full bridge configuration is used and sampling frequency on every channel is set at 5 kHz. Data collected are the position and velocity of the wedge, including the time-varying pressure from the different transducers. Yettou et al. (2006)

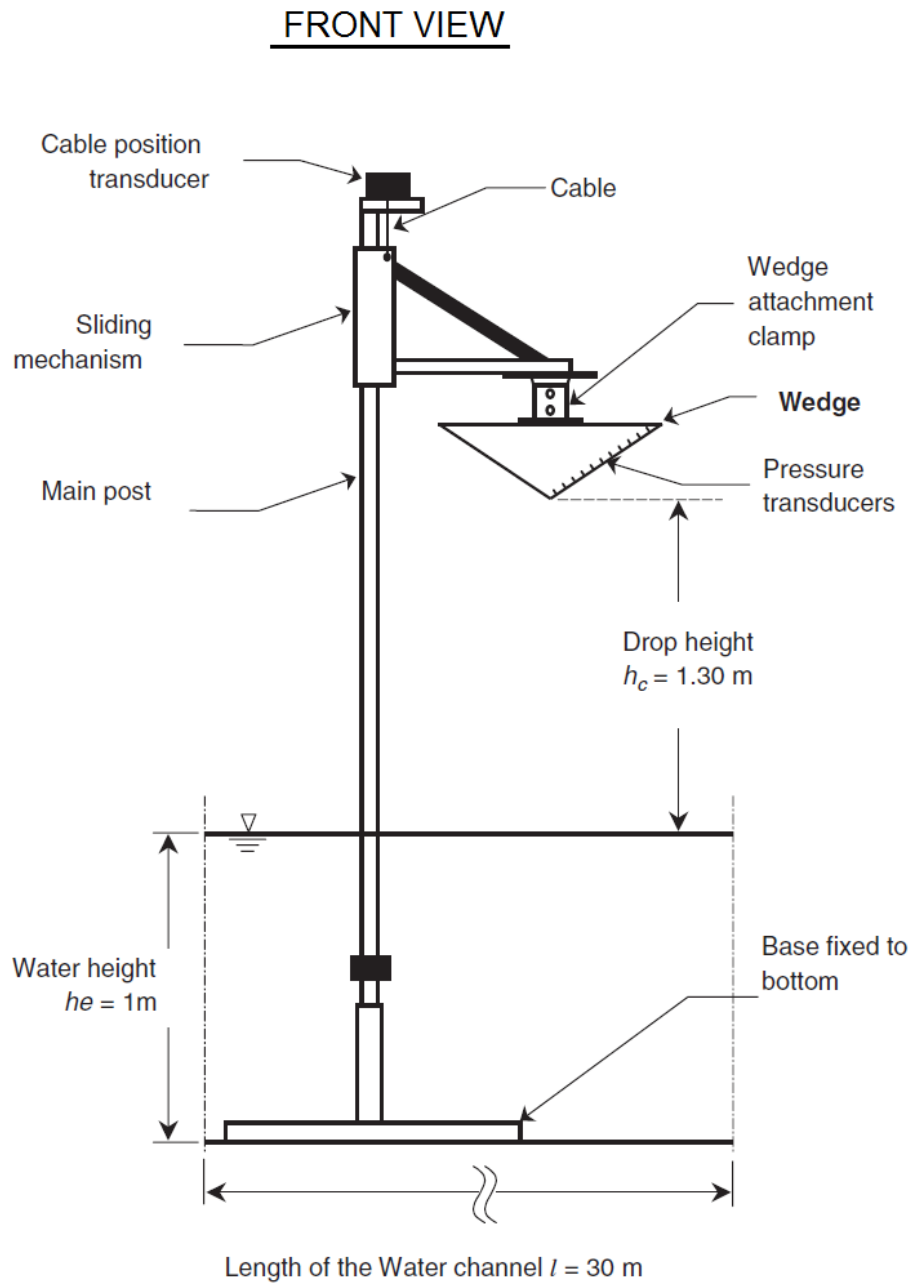


Figure 4.1: Diagram of the experimental set-up. Yettou et al. (2006)

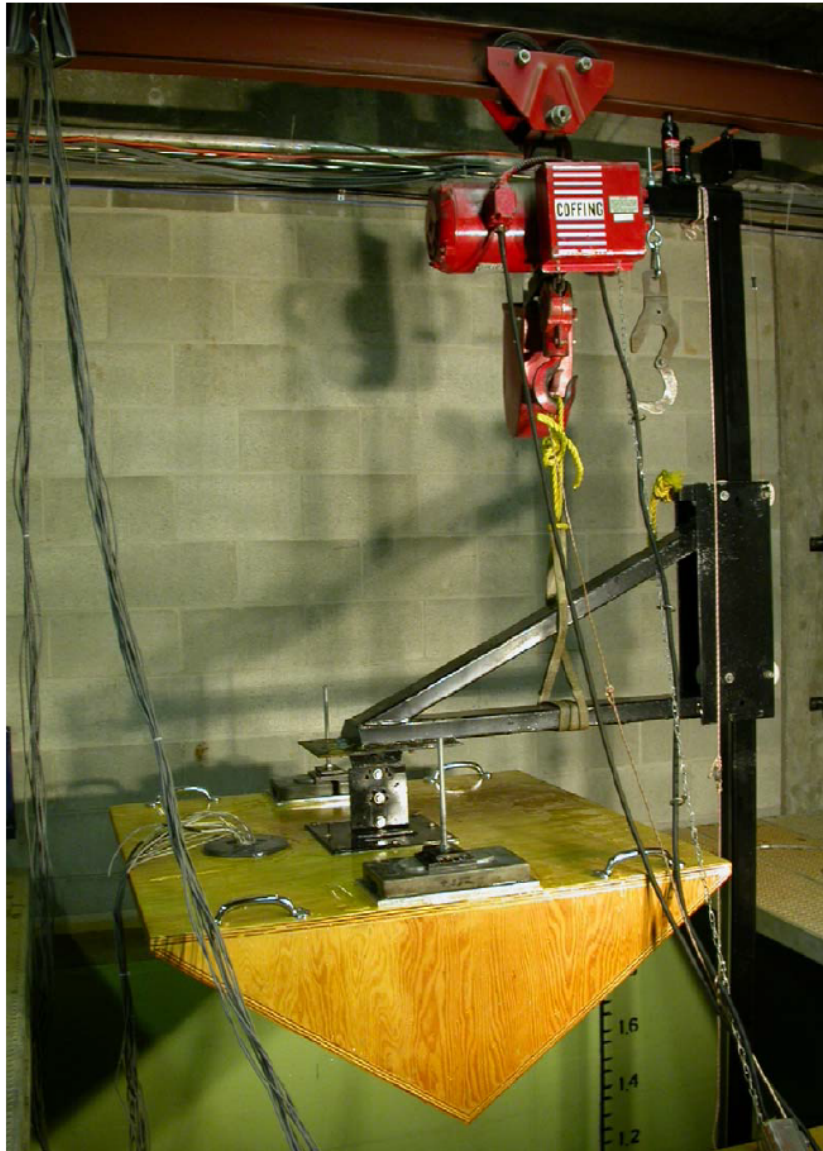


Figure 4.2: Image of the experimental set-up installed in the water channel. Yettou et al. (2006)

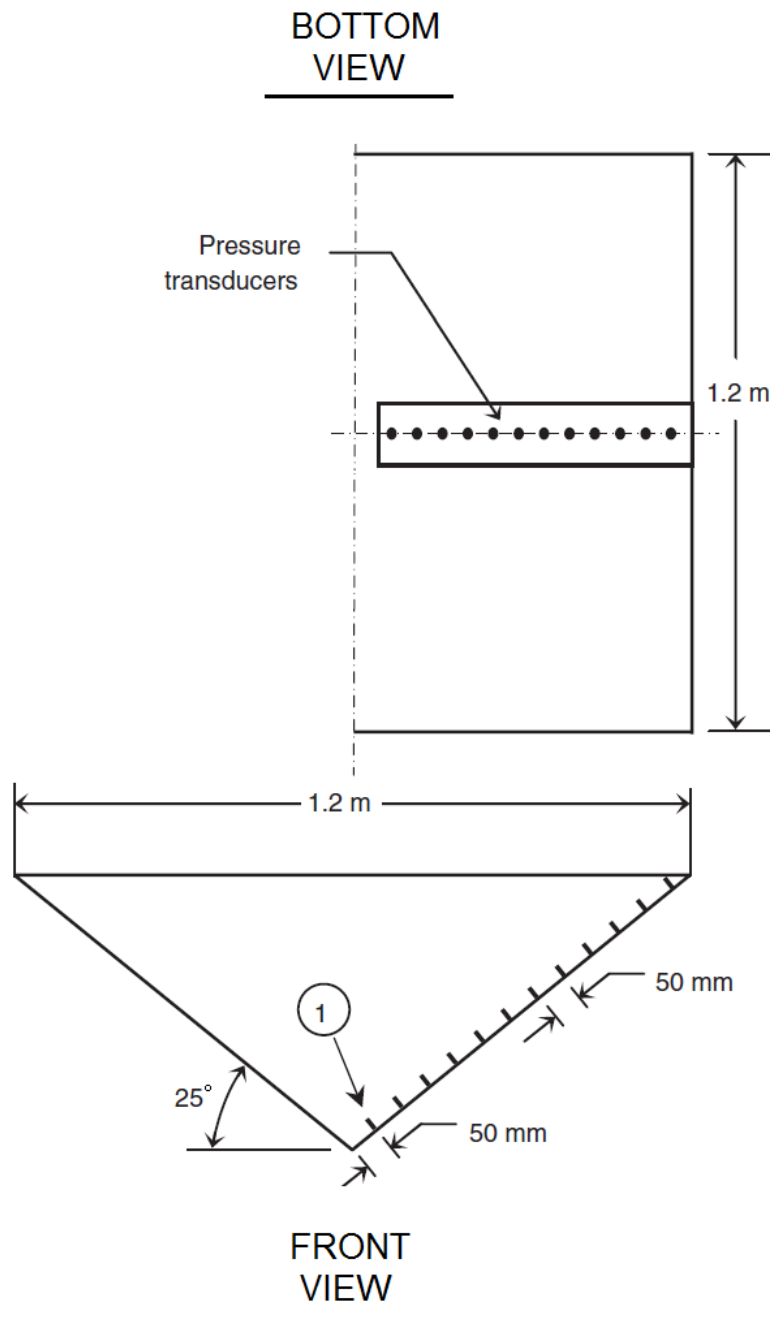


Figure 4.3: Position of the twelve transducers along the wedge's median. Yettou et al. (2006)

4.2 SOLUTION IN STAR-CCM+

The water entry of a free-falling three-dimensional rigid wedge is simulated and studied in STAR. The simulation is set up to replicate the experiment described in Section 4.1. The wedge, with deadrise angle $\alpha = 25^\circ$, is dropped from a height 1.3 m into a basin 1 m deep, 2 m wide and 30 m long (see Figure 4.1). Its top square section measures 1.2 m \times 1.2 m and the total mass equals 94 kg. As for the water entry of two-dimensional wedges described in Chapter 3, a laminar flow model is considered sufficient¹. Due to the symmetric water entry and the symmetry along the median of the wedge where the transducers are located, only one quarter of the wedge is modeled. A body-fixed mesh is used and the vertical motion of the wedge is achieved by using the *DFBI-Rotation and Translation* model in STAR². Hence, the mesh and wedge falls together influenced by gravity and air resistance only, whereas the free surface is fixed in a local coordinate system, not allowed to move. Capturing of the high local slamming pressures is achieved by grid refinements at the wedge apex and walls, including the transducers surface. To ensure stability in the solution a time step is chosen such that the maximum Courant number at critical regions is approximately equal to 0.5.

All simulations of the 3-D rigid wedge are run on an AMD computer cluster with a total of 32 cores, each at 2.40 Ghz. Where the wedge is studied for 2 seconds (real time), at highest resolution of grid size and time step, a computational time of 2 days is recorded.

MODELING

The wedge and water basin geometries are created in STAR's own CAD environment. As illustrated in Figure 4.4, due to symmetry, only one quarter of the experimental set-up needs to be modeled.

The basin's length is not modeled to its full length. This is due to the fact that the slamming which is to be investigated will be unaffected by the walls at the far end. In conversations with Peric (2012) a total basin length of 10 m was concluded sufficient. Due to the symmetry condition a 5 m long domain is therefore modeled. Figure 4.5 and 4.6 shows the quarter wedge and water basin created in STAR, front and top view respectively. Figure 4.5 is seen in connection with Figure 4.1; Figure 4.6 with Figure 4.4.

As there exist a symmetry plane about the median of the wedge (see Figure 4.4), only one half of the transducer is modeled. The transducers are modeled as patches on the wedge bottom boundary, hence there exist no irregularities on the wedge surface caused by the presence of the transducers³. The pressure is obtained by taking a *surface average* over the half-transducer. This will yield the same result as if the whole transducer, together with half-wedge and water basin geometry, were to be modeled.

¹A laminar flow model is considered sufficient as the water entry of the wedge is characterized by high local slamming pressures. A study on laminar vs. turbulent flow is described later in this chapter.

²The 6-DOF DFBI model in STAR-CCM+ is used to simulate the motion of a rigid body in response to pressure and shear force exerted by the fluid.

³Information on how the transducers were placed in the experimental work of Yettou et al. (2006) has not been obtained.

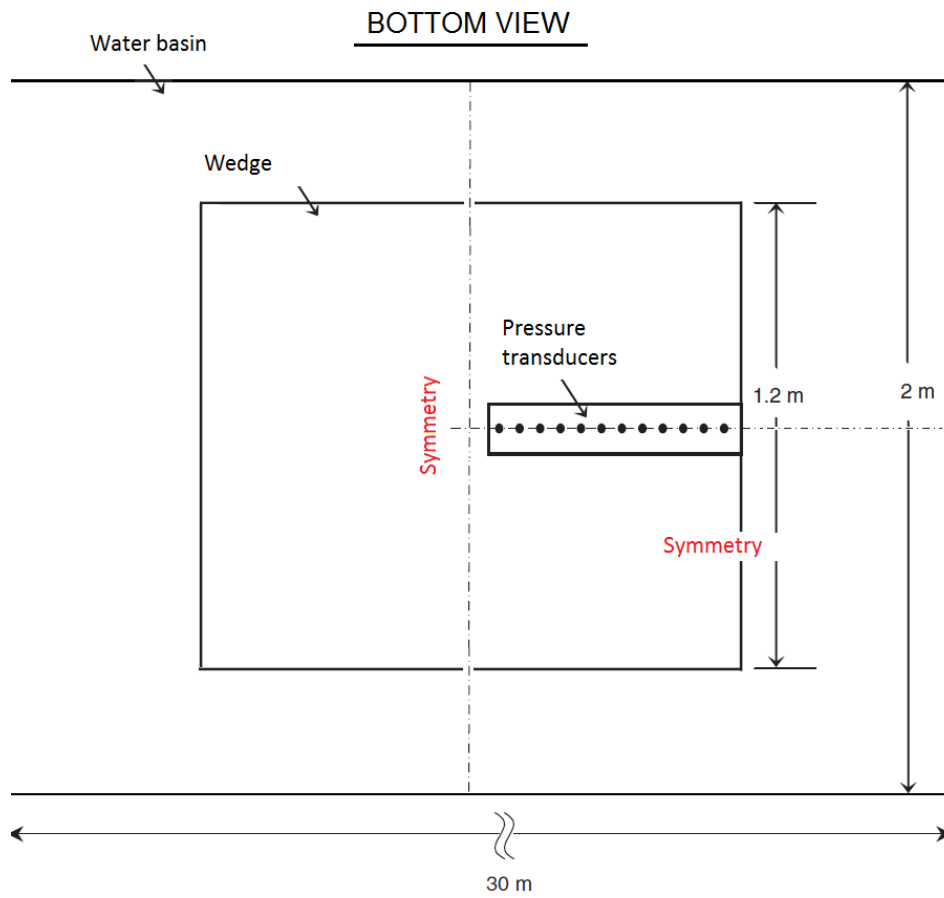


Figure 4.4: The symmetric conditions applied when modeling the geometry in STAR.

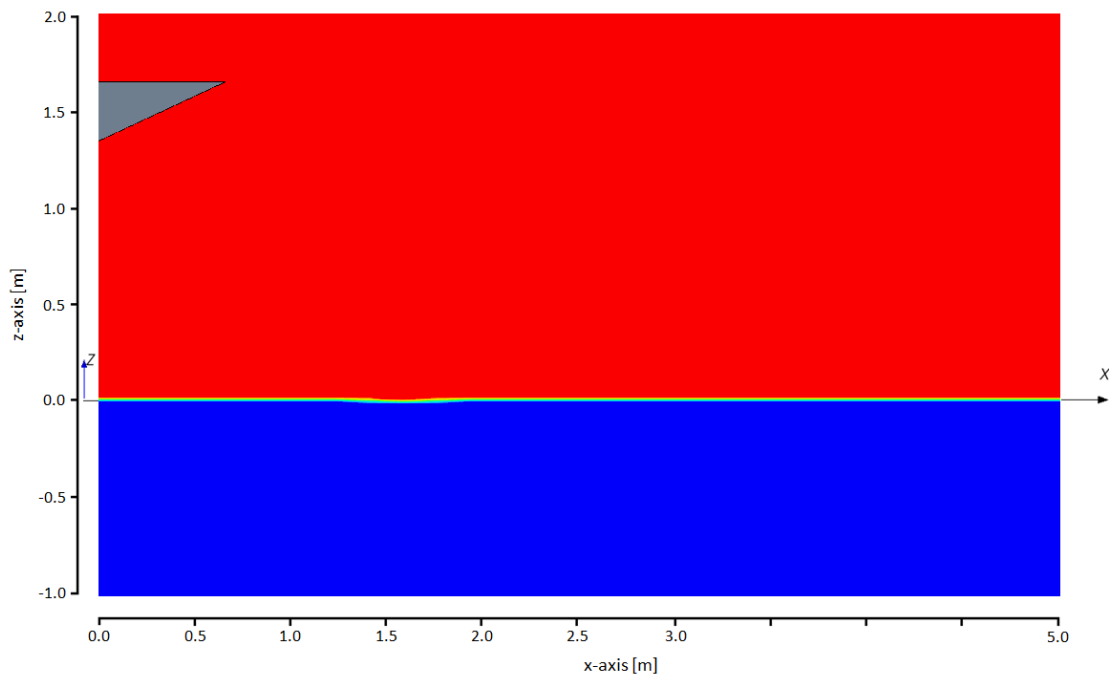


Figure 4.5: Front view of the quarter wedge and water basin modeled in STAR.

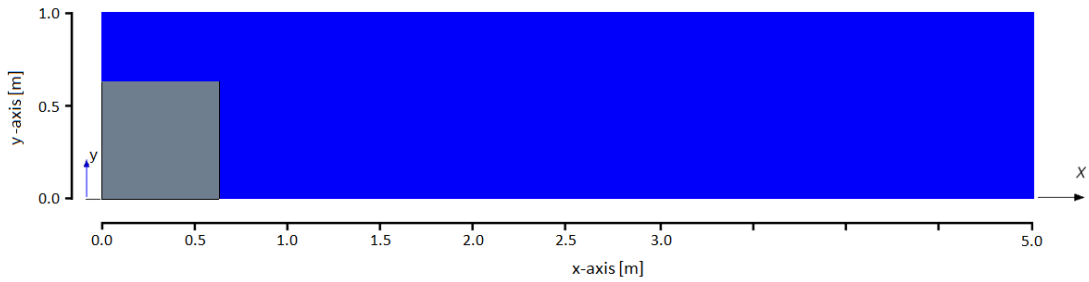


Figure 4.6: Top view of the quarter wedge and water basin modeled in STAR.

DISCRETIZATION OF TIME AND SPACE

When modeling the wedge water entry in STAR, the effect on the result of domain and grid size, including time step, needs to be considered. All the three parameters will influence the slamming pressures on the wedge bottom and therefore a systematic study is performed to obtain a proper solution. In the convergence study only one of the transducer, the one closest to the wedge apex, is studied. For each simulation the maximum pressure p_{\max} and the surface averaged pressure over the 19 mm diameter p_{ave} transducer are logged. Figure 4.7 shows the time history for the maximum pressure p_{\max} and averaged pressure p_{ave} at the transducer closest to the wedge apex at impact to $t = 0.05$ s after impact.

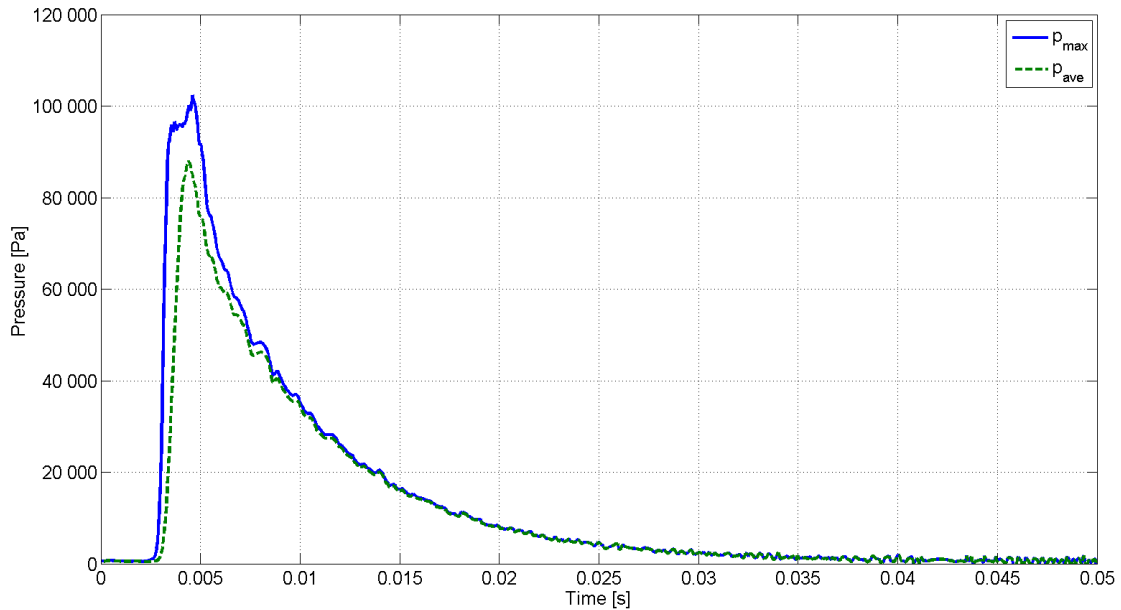


Figure 4.7: Time history for the maximum pressure p_{\max} and averaged pressure p_{ave} at the transducer closest to the wedge apex at impact to $t = 0.05$ s after impact.

Domain size

In the case for the three-dimensional water entry, only one domain size is considered. This follows from the study conducted in Chapter 3 where a minimal change in results are found from choosing reasonable domain sizes. *Reasonable* in this context means

choosing a domain such that the simulation, in a best manner, resembles the experiment which it is to replicate. The domain size for the simulation has been chosen together with Peric (2012) and is presented in Table 4.1. A visualization can be seen in Figure 4.5 and Figure 4.6.

Table 4.1: The domain used in the three-dimensional water entry study. The coordinates are seen in connection with Figure 4.5 and Figure 4.6.

	x_{\min}	x_{\max}	y_{\min}	y_{\max}	z_{\min}	z_{\max}	<i>Cells</i>
Domain	0.0	5.0	0.0	1.0	-1.0	2	325 090

Grid size

A sufficient grid resolution is needed to capture the local slamming pressures which arises during water entry. In the free-fall wedge experiment conducted by Yettou et al. (2006), slamming pressures are found by using pressure transducers. To make sure STAR resolves the slamming pressures correctly, the grid size needs to be small in the critical regions, i.e. the modeled pressure transducers. This implies that refinements only needs to be done at and in the vicinity of the transducers and not on the whole wedge bottom surface (resulting in lower computational time). If the grid is chosen too coarse STAR is not able to recreate the transducers boundaries, and the area over which the pressure is averaged will be wrong. This effect of grid size on the transducer geometry can be seen in Figure 4.8, where the bottom left shows a coarse grid with 5 mm wide cells and the bottom right is fine with a width of 1.25 mm.

When changing the grid size one must also make sure that the time step is chosen such that stability is conserved. A too high time step will make the solver "jump" cells, causing an unstable solution. Therefore, a decrease in cell size results in choosing a smaller time step. As the number of cells is increased, and the time step lowered, the accuracy of the prediction of the pressure along the transducers increases. However, such an increase in accuracy also leads to an increase in computational time.

In the grid size study, four different grid sizes are tested. The grids number of cells and cell width are shown in Table 4.2.

Table 4.2: The four different grids used in the grid size analysis. Δx_{\min} and Δz_{\min} denotes the extent of smallest cells.

	Cells	Δx_{\min} [m]	Δz_{\min} [m]	$\frac{\Delta x_{\min}}{\Delta z_{\min}}$	Time step [Δs]
Grid 1	132 811	0.01000	0.01000	1.00	0.00010
Grid 2	154 812	0.00500	0.00500	1.00	0.00010
Grid 3	202 955	0.00250	0.00250	1.00	0.00005
Grid 4	325 090	0.00125	0.00125	1.00	0.00005

Of all the twelve transducers only one, the one closest to the wedge apex, is considered. The compared values at the transducer's boundary for each grid are the maximum pressure p_{\max} , the surface averaged pressure over the 19 mm diameter p_{ave} transducer, the pressure coefficient at maximum pressure $C_{p_{\max}} = (p_{\max} - p_0)/(0.5\rho V^2)$ and the pressure coefficient at the surface averaged pressure $C_{p_{\text{ave}}} = (p_{\text{ave}} - p_0)/(0.5\rho V^2)$. The comparison of values is shown in Table 4.3.

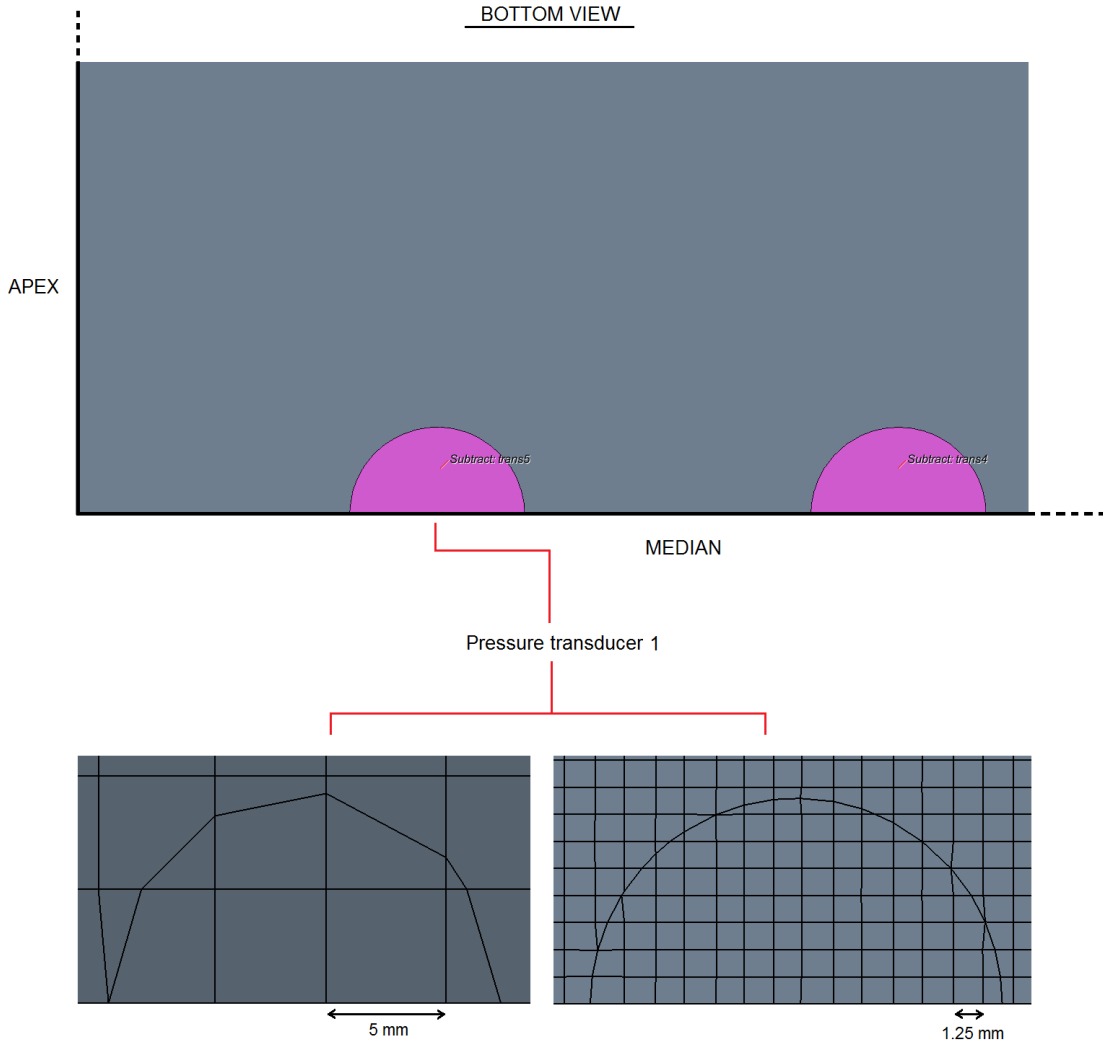


Figure 4.8: The effect of grid size on the transducer geometry. Bottom left shows a coarse grid with 5 mm wide cells, while the bottom right is fine with a width of 1.25 mm.

Table 4.3: The effect of grid size at the transducer's boundary on the maximum pressure p_{\max} , the surface averaged pressure over the 19 mm diameter p_{ave} , the pressure coefficient at maximum pressure $C_{p_{\max}} = (p_{\max} - p_0)/(0.5\rho V^2)$ and the pressure coefficient at the surface averaged pressure $C_{p_{\text{ave}}} = (p_{\text{ave}} - p_0)/(0.5\rho V^2)$.

	p_{\max} [Pa]	p_{ave} [Pa]	$C_{p_{\max}}$ [-]	$C_{p_{\text{ave}}}$ [-]
Grid 1	88 097	65 964	8.01	6.24
Grid 2	83 447	73 218	7.57	6.84
Grid 3	94 129	87 997	8.50	7.82
Grid 4	102 405	87 936	9.29	7.92

The tabulated data from Table 4.3 are plotted in Figure 4.9 and Figure 4.10. By studying the two plots it is seen that a grid containing smaller cells have the effect of predicting higher pressures. The irregularity for $\Delta x_{\min} = 0.01$ m for p_{\max} and $C_{p_{\max}}$ is due to pressure spikes caused by numerical errors. This irregularity does not occur for p_{ave} and $C_{p_{\text{ave}}}$ (at $\Delta x_{\min} = 0.01$ m), as the pressures are averaged over the surface.

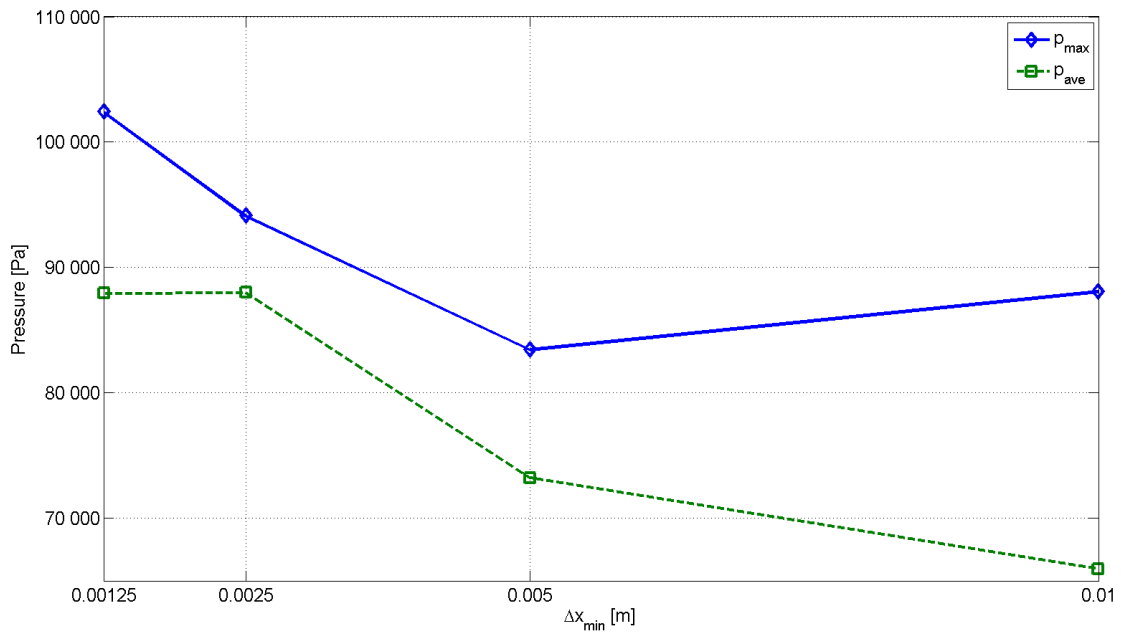


Figure 4.9: The effect of grid size at the transducer's boundary on the maximum pressure p_{\max} and the surface averaged pressure over the 19 mm diameter p_{ave} .

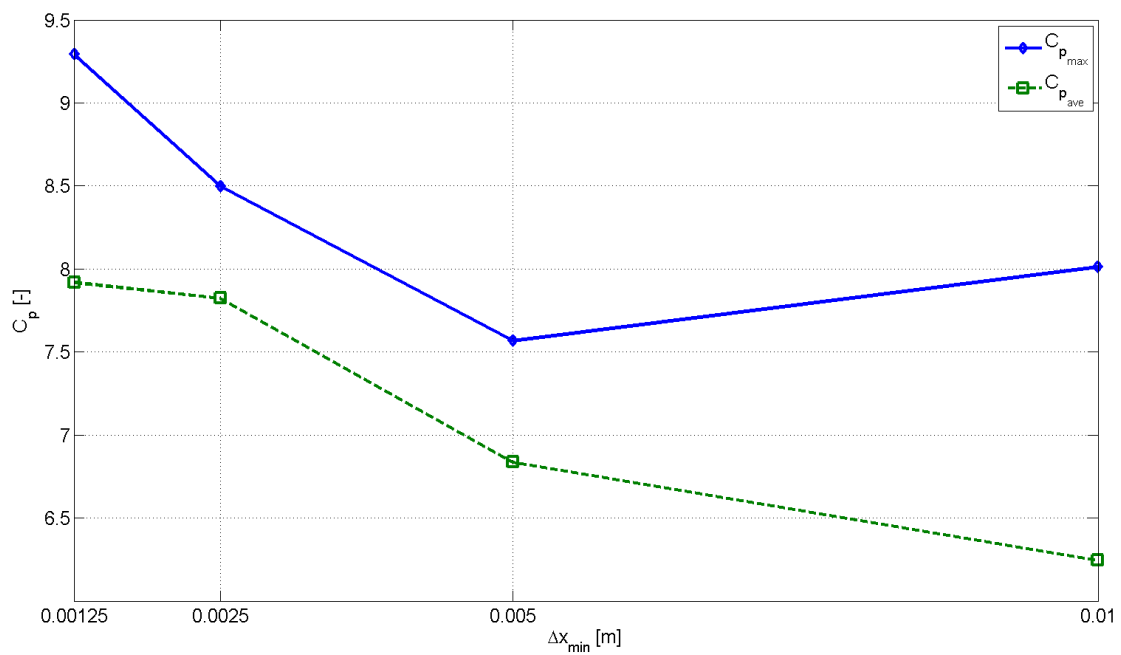


Figure 4.10: The effect of grid size at the transducer's boundary on the pressure coefficient at maximum pressure $C_{p_{\max}} = (p_{\max} - p_0)/(0.5\rho V^2)$ and the pressure coefficient at the surface averaged pressure $C_{p_{\text{ave}}} = (p_{\text{ave}} - p_0)/(0.5\rho V^2)$.

Time step

When decreasing the cell size one must also decrease the time step. In this way the pressure values that occur in the cell can be captured by the solver. Following, the effect of choice of time step on the maximum pressure p_{\max} and the surface averaged pressure over the 19 mm diameter p_{ave} transducer is studied. The coefficients $C_{p_{\max}}$ and $C_{p_{\text{ave}}}$ are also included.

In the grid size study the time step is altered from each simulation to achieve stability. In the time step study only one of the grid is chosen; Grid 2 from Table 4.2. Four different time steps are studied. Their influence on the different pressure values are shown in Table 4.4.

Table 4.4: The effect of time step at the transducer's boundary on the maximum pressure p_{\max} , the surface averaged pressure over the 19 mm diameter p_{ave} , the pressure coefficient at maximum pressure $C_{p_{\max}} = (p_{\max} - p_0)/(0.5\rho V^2)$ and the pressure coefficient at the surface averaged pressure $C_{p_{\text{ave}}} = (p_{\text{ave}} - p_0)/(0.5\rho V^2)$.

Time step [Δs]	p_{\max} [Pa]	p_{ave} [Pa]	$C_{p_{\max}}$ [-]	$C_{p_{\text{ave}}}$ [-]
0.00100	58 960	57 471	5.75	5.61
0.00050	66 668	62 931	6.12	6.00
0.00010	83 447	73 218	7.57	6.84
0.00005	95 621	80 783	8.72	7.49

The tabulated data from Table 4.4 are plotted in Figure 4.11 and Figure 4.12. By studying the two plots it is seen that choosing a smaller time step leads to a prediction of both higher maximum pressure p_{\max} and average pressure p_{ave} on the transducer's surface.

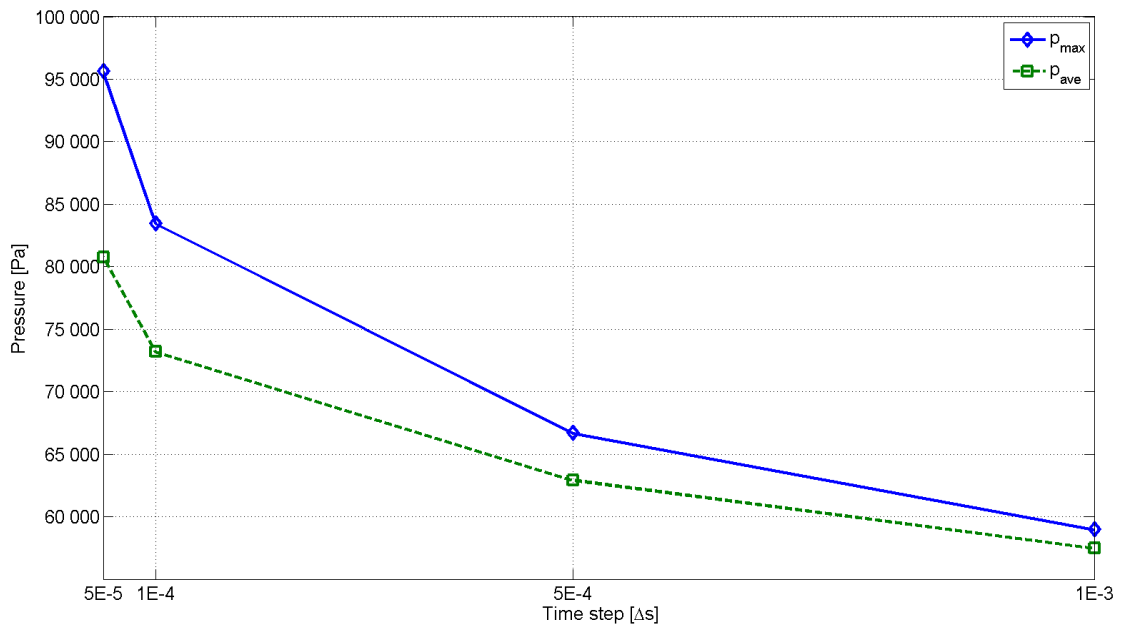


Figure 4.11: The effect of time step on the maximum pressure p_{\max} and the surface averaged pressure over the 19 mm diameter p_{ave} .

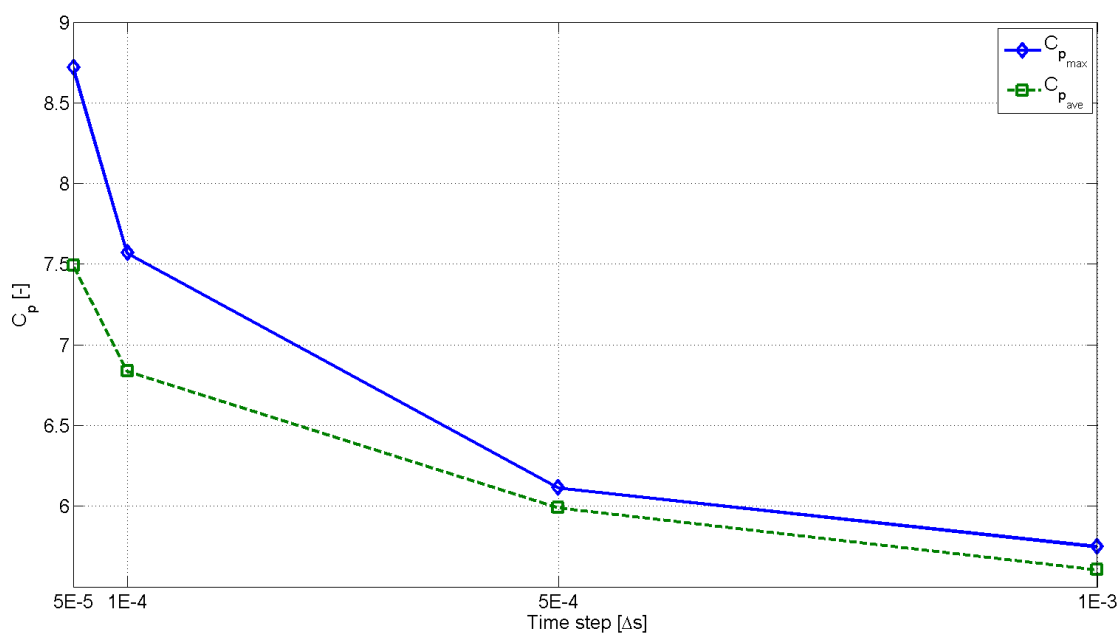


Figure 4.12: The effect of time step on the pressure coefficient at maximum pressure $C_{p_{max}} = (p_{max} - p_0)/(0.5\rho V^2)$ and the pressure coefficient at the surface averaged pressure $C_{p_{ave}} = (p_{ave} - p_0)/(0.5\rho V^2)$.

LAMINAR VERSUS TURBULENT FLOW

As in Chapter 3, it is necessary to decide on which flow model to use when studying the wedge water entry. For the two-dimensional case it is found that a laminar model is sufficient to describe the slamming pressures. An equal study is performed for the three-dimensional case to decide on type of flow model needed.

For the free-falling three-dimensional rigid wedge, the water impact velocity is calculated to approximately 5 m/s. This implies a Reynolds number at approximately $6E^6$ ($Re = \rho UL/\mu$). For flow past a flat plate, the transition from laminar to turbulent begins at $Re = 5E^5$. This implies that the effect of turbulence on the slamming pressure has to be determined.

To investigate the dependence of flow model on the solution two difference turbulence models are chosen to close the Navier-Stokes equations: the $k-\varepsilon$ model and the $k-\omega$ model. The two approaches are compared with a laminar solution and all three solutions are run using Grid 4 with time step equal to 0.00005 s (ref. Table 4.2). The values studied in each simulation are the maximum pressure p_{max} , the surface averaged pressure over the 19 mm diameter p_{ave} transducer, the pressure coefficient at maximum pressure $C_{p_{max}} = (p_{max} - p_0)/(0.5\rho V^2)$ and the pressure coefficient at the surface averaged pressure $C_{p_{ave}} = (p_{ave} - p_0)/(0.5\rho V^2)$. The Wall $y+$ value is also included (for details about Wall $y+$ see Johannessen (2011)). Comparison of values is shown in Table 4.5.

Table 4.5: The effect of choice of flow model on the maximum pressure p_{\max} , the surface averaged pressure over the 19 mm diameter p_{ave} , the pressure coefficient at maximum pressure $C_{p_{\max}} = (p_{\max} - p_0)/(0.5\rho V^2)$ and the pressure coefficient at the surface averaged pressure $C_{p_{\text{ave}}} = (p_{\text{ave}} - p_0)/(0.5\rho V^2)$. The Wall $y+$ value is also included.

	p_{\max} [Pa]	p_{ave} [Pa]	$C_{p_{\max}}$ [-]	$C_{p_{\text{ave}}}$ [-]	Wall $y+$
$k-\varepsilon$ model	101 667	89 288	9.13	7.95	253.40
$k-\omega$ model	101 212	89 353	9.08	7.97	251.91
Laminar model	104 084	88 598	9.21	7.91	-

The tabulated data from Table 4.5 are plotted in Figure 4.13 and Figure 4.14. By studying the two plots it is seen that choice of turbulence model has close to no influence on the pressure values. The laminar model gives an increase of about 3% for the maximum pressure p_{\max} and a decrease of about 1% for the surface average pressure p_{ave} , compared to the two turbulence models.

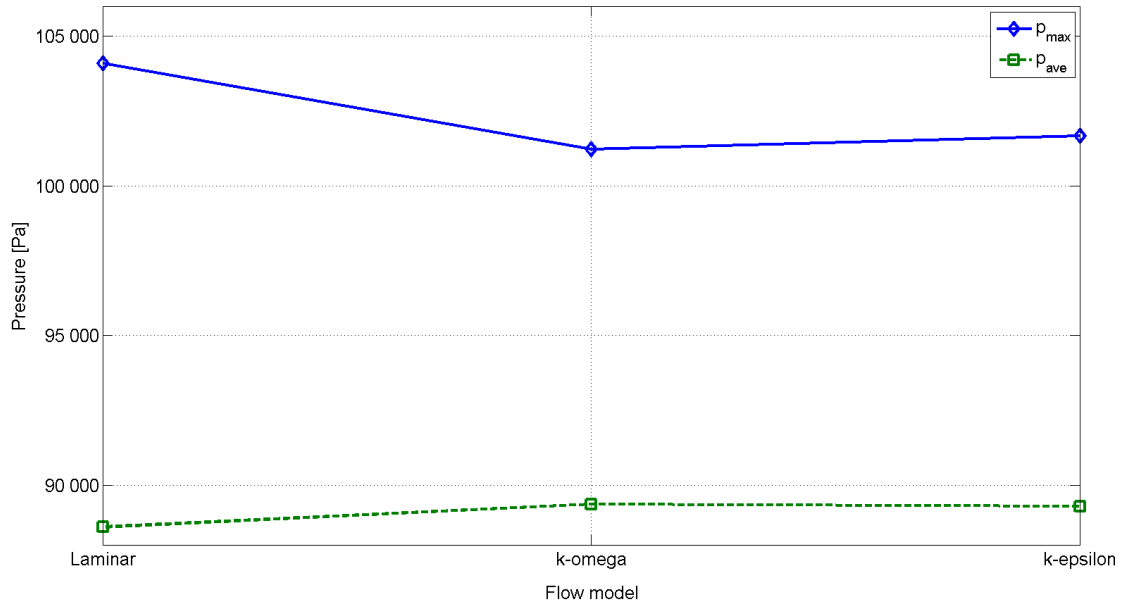


Figure 4.13: The effect of choice of flow model on the maximum pressure p_{\max} and the surface averaged pressure over the 19 mm diameter p_{ave} transducer.

INFLUENCE OF NUMERICAL PARAMETERS

When setting up a CFD simulation in STAR a number of input parameters needs to be chosen. A study is performed to decide on which values to apply to obtain the most satisfactory result. The study is performed systematically by altering the different parameters, one at a time, and noting the effect on the result. As there exist a rather large amount of input parameters which can be varied in a simulation, only two are explained further in this section.

Two input parameters which are seen to influence the solution in the three-dimensional rigid wedge water entry, are the *Under-Relaxation Factor* (URF) and the *Maximum Inner Iterations* (MII). The URF is a parameter chosen in the *Pressure Solver*. The

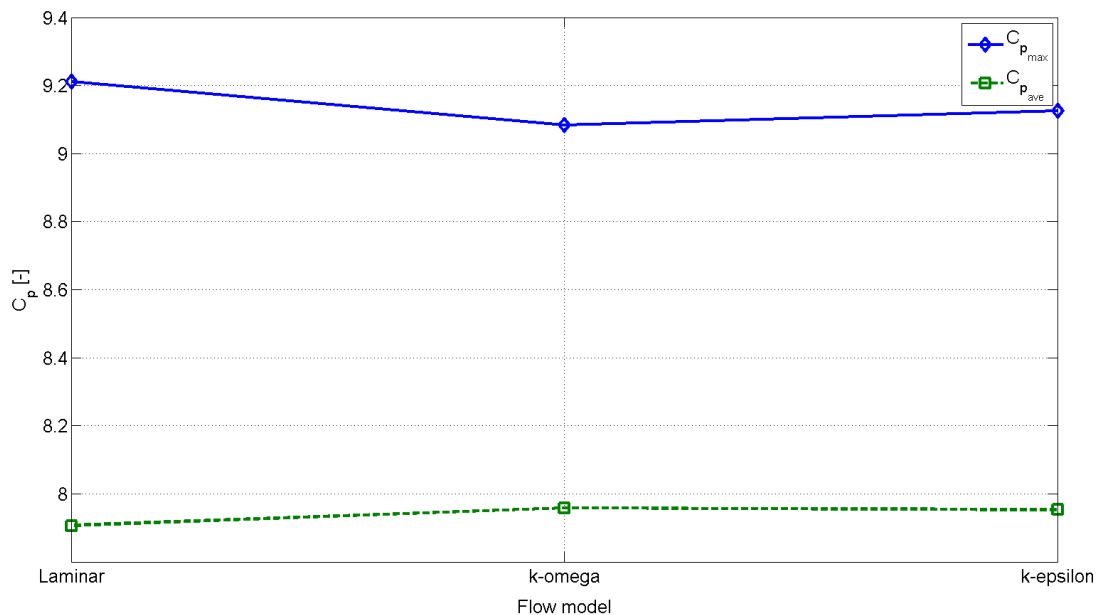


Figure 4.14: The effect of choice of flow model on the pressure coefficient at maximum pressure $C_{p_{max}} = (p_{max} - p_0)/(0.5\rho V^2)$ and the pressure coefficient at the surface averaged pressure $C_{p_{ave}} = (p_{ave} - p_0)/(0.5\rho V^2)$.

pressure solver controls the URF and algebraic multigrid parameters for the pressure correction equation (the algebraic multigrid methods solves the discrete linear system iteratively (for details see CD-adapco (2011)). More specifically, it solves the discrete equation for the pressure correction, and updates the pressure field. The URF property in the pressure solver governs the extent to which the old solution is supplanted by the newly computed solution. The parameter is chosen between 0 to 1. If the URF is chosen close to 0, the value of the next iteration will be governed by the value computed by previous iteration, and not the current. Likewise, if the URF is chosen close to 1, the next iteration will be governed by the value computed by current iteration and not the previous. As an mathematical illustration let the URF for pressure be denoted ω_p . Further, let p_t^n be the pressure value of the previous iteration, and p_t^{new} be the value computed during the current iteration. Then the update is controlled as follows: $p_t^{n+1} = \omega_p p_t^{new} + (1 - \omega_p) p_t^n$. The URF can be set for pressure and velocity and is adjusted to control the convergence of the solution. It is a generally accepted rule of thumb that under-relaxation factors for velocity and pressure should add up to 1. If the residuals are converging quite well it is acceptable to try to increase the URF (this will reduce computational time). In the study on choice of URF for the wedge water entry, the URF for both pressure and velocity are systematically varied: 0.1-0.4 for pressure and 0.6-0.9 for velocity. The choice of values is done in agreement with Peric (2012) and Bjelke-Mørch (2012). It is found that as time step and cell size are decreased, a decrease in URF for pressure is required to obtain a stable solution. A value of 0.1 for pressure is found sufficient to obtain stability in the pressure field.

The *Maximum Inner Iterations* (MII) stopping criterion is based on the number of inner iterations executed by the solver for each time step. Smaller physical time steps generally mean the solution is changing less from one time step to the next, so that fewer inner iterations are required to achieve convergence in the solution. The maximum inner iterations value must be selected carefully: if the value is too low, the solution will not

converge within a time step; if it is too high the solution will take a long time to complete. For a given problem there will be an optimal balance of time step, under-relaxations factors and the inner iteration to achieve the desired convergence level. In the three-dimensional rigid wedge water entry case a maximum number of 15 inner iterations is found sufficient to obtain stability and convergence in the solution. In Table 4.6, a selection of parameters tested in the convergence study is listed. Further study of the set-up and simulation can be done in *wedge3d.sim* found in the folder *wedge3D-rigid* in the attached ZIP-file.

Table 4.6: Parameters tested in the convergence study for the three-dimensional wedge. The final chosen values are also included.

	Parameter	Tested	Chosen
<i>Physics</i>			
Segregated Flow	Convection	1st-/2nd-order	2nd-order
Volume of Fluid	Convection	1st-/2nd-order	2nd-order
<i>Solver</i>			
Implicit Unsteady	Temporal Discretization	1st-/2nd-order	1st-order
6-DOF Solver	Number of Iterations	6,8,10,15	6
Segregated Flow	Under-Relaxation: Velocity	0.6, 0.7, 0.8, 0.9	0.7
Segregated Flow	Under-Relaxation: Pressure	0.1, 0.2, 0.3, 0.4	0.1
<i>Stopping Criteria</i>			
Iterations	Number of Inner Iterations	5,8,10,15,20	15

4.3 RESULTS

From the grid size study it is found that a decrease in cell size results in an increase in slamming pressures. Grid 4 (ref. Table 4.2) with a minimum size of 0.00125 m in x and z -direction is therefore chosen in the final study. A time step equal to 0.00005 s is applied to achieve a stable solution. Little difference in the result is found by choice of flow model. A laminar model is therefore applied to reduce the computational time. Through the *input parameters* study it is found that convergence and stability in the solution is found by applying an under-relaxation factor for velocity and pressure of 0.7 and 0.1, respectively. The free surface is inspected to ensure that a reasonably sharp interface is predicted with a rapid variation of volume fraction across 2 to 3 cells only. Figure 4.15 illustrates the free surface mid-way through the simulation for Grid 4. The volume fraction is deemed acceptable with clear identification both of the wedge water jet and the free surface.

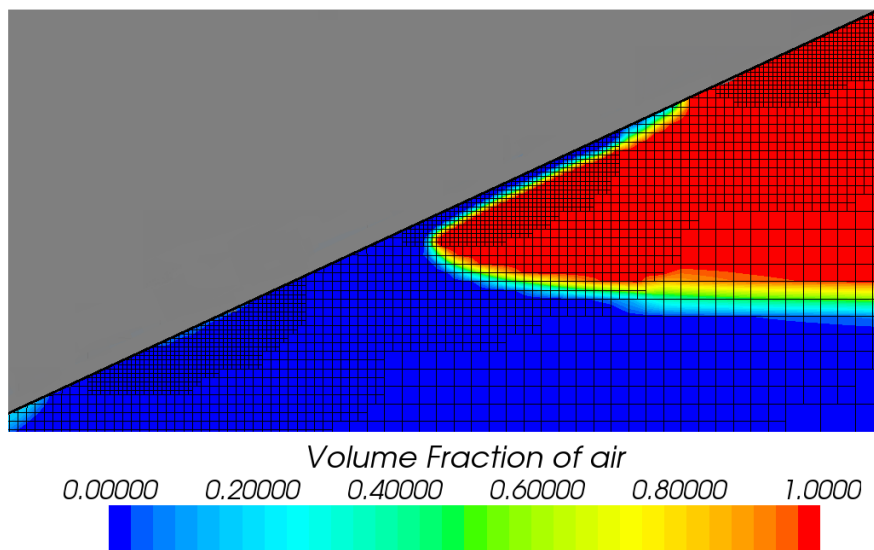


Figure 4.15: The free surface mid-way through the simulation for Grid 4. Notice the volume fraction between water and air across the cells.

RAW DATA ANALYZES

From its initial position - 1.3 m above the mean water level, the wedge's displacement is studied. Figure 4.16 shows displacement curves from the simulation in STAR and the experimental work conducted by Yettou et al. (2006). A decent agreement is seen all the way to $t \approx 1.5$ s, although the curves reveal an earlier impact at 1.3 m at $t = 0.5$ s for the wedge in the experimental study. By studying the figure it is noted that the zone of interest, i.e. the wedge slamming, is limited to a period lasting only about 50 ms. This implies that a good refinement in time step is needed to be able to study the slamming phenomena. Figure 4.17 shows the velocity of the wedge from its initial position to 1.5 s after impact. Results from both the simulation in STAR and the work by Yettou et al. (2006) are included. For the experimental data, the wedge velocity is obtained from the derivation and low pass filtering of the displacement data. The small oscillations are related to the vibration of the cord. Again, it is seen that the zone of interest is limited to small period of time. The velocity-time history plot reveals a decent agreement between the two results, though a higher impact velocity is seen for the experimental data (i.e. the reason for the earlier impact of the wedge as seen from the displacement curves).

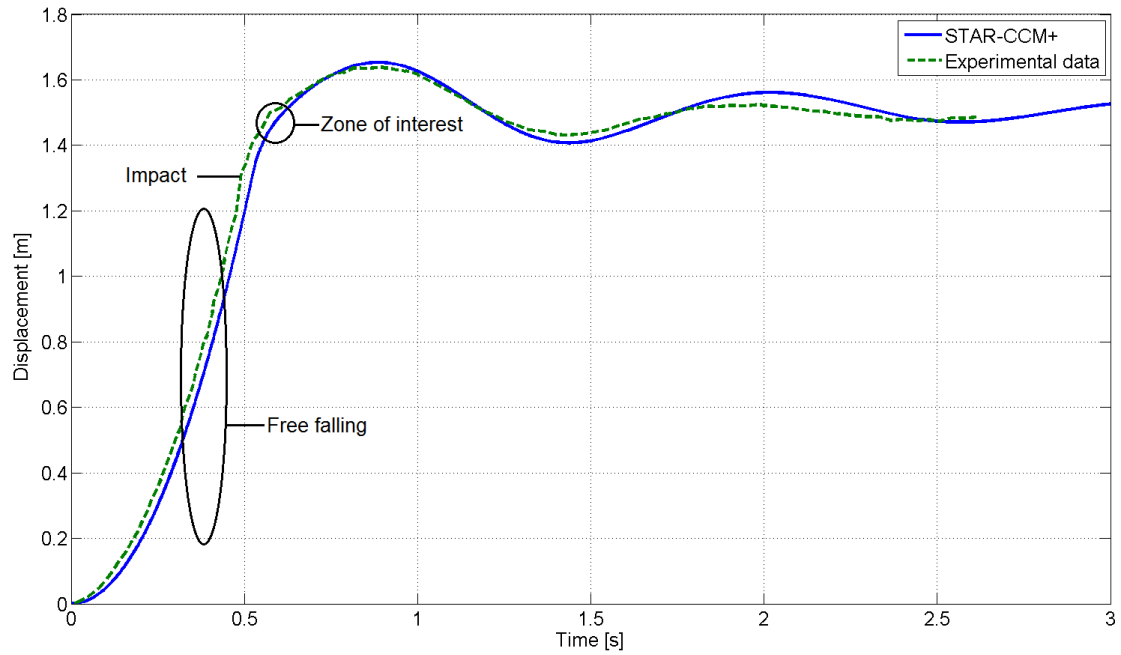


Figure 4.16: The wedge's displacement recorded by Yettou et al. (2006) together with the displacement predicted in STAR-CCM+.

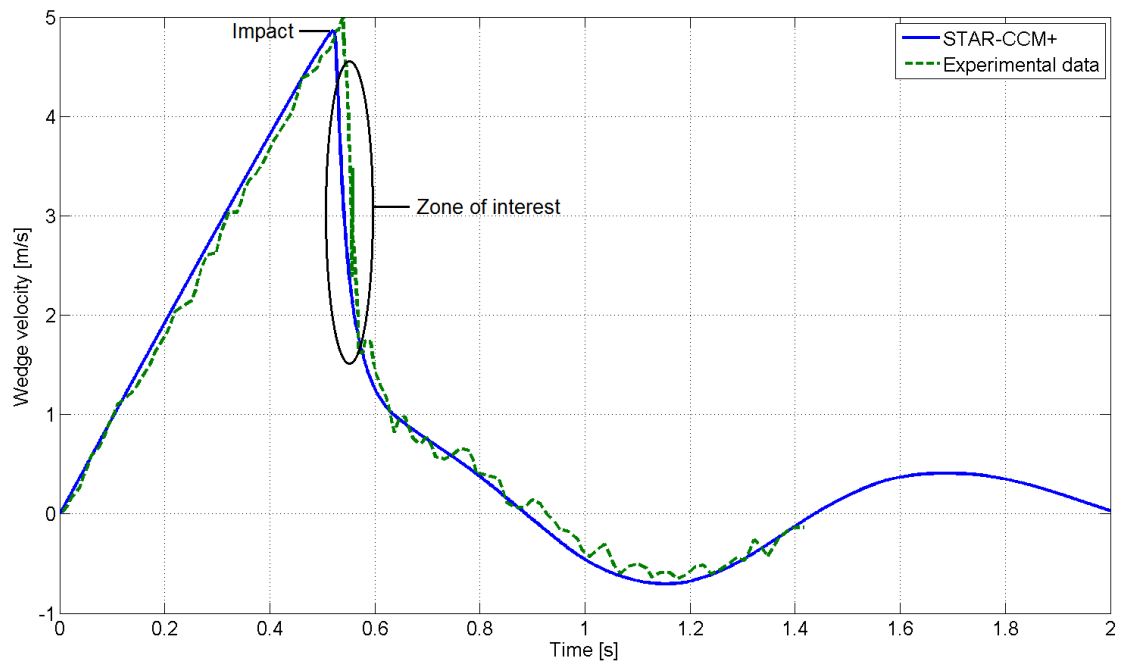


Figure 4.17: The wedge's velocity recorded by Yettou et al. (2006) together with the velocity predicted in STAR-CCM+.

Figure 4.18 shows the time history for the pressure measurements for all 12 transducers. Presented are pressures recorded by Yettou et al. (2006) and the maximum pressure p_{\max} and the surface averaged pressure over the 19 mm diameter p_{ave} transducer predicted in STAR-CCM+. The vertical axes of each curve are respectively scaled to show maximum detail. Transducer no. 1 is the first to contact the water and its peak pressure is located on the time scale at roughly $t = 3$ ms. Note that at this moment, all the other transducers are not yet in contact with the water. The peak pressure for each transducer appears sequentially at a later time during the penetration process of the wedge. Table 4.7 presents the surface averaged pressure p_{ave} , maximum pressure p_{\max} and peak pressures measured in the experiment for all the 12 transducers. The peak pressure's occurrence in time is also included.

Table 4.7: Surface averaged pressure p_{ave} , maximum pressure p_{\max} and peak pressures measured in the experiment for all the 12 transducers. Each peak pressure occurrence in time is included.

Trans.	$p_{\text{ave}} - STAR$		$p_{\max} - STAR$		$p_{\text{peak}} - Exp.$	
	p [Pa]	t [ms]	p [Pa]	t [ms]	p [Pa]	t [ms]
1	87 940	2.85	102 400	3.05	128 800	2.85
2	85 890	5.90	98 590	5.50	125 100	5.13
3	71 300	9.25	82 520	8.45	99 410	9.33
4	58 320	12.90	64 300	12.20	87 490	13.14
5	44 160	17.20	51 210	16.50	67 980	17.48
6	33 440	22.35	37 070	21.00	50 950	23.24
7	25 860	28.00	28 900	27.10	42 060	28.80
8	19 420	34.35	21 310	32.90	32 610	37.52
9	14 790	42.05	16 180	40.00	27 710	43.90
10	11 440	50.85	12 360	48.40	19 930	51.88
11	8 634	60.30	9 343	58.60	16 890	61.52
12	6 793	70.90	7 330	69.70	13 240	70.76

By studying Figure 4.18 and Table 4.7 it is seen that both the surface averaged pressure p_{ave} and the maximum pressure p_{\max} predicted in STAR are lower than what is found in the experimental study. This discrepancy can be seen in connection with the wedge velocity plotted in in Figure 4.17. Here, we note that the wedge velocity predicted in STAR does not reach the maximum of 5 m/s (as is the case in the experiment). This causes STAR to predict a lower slamming pressure, as the slamming pressure is depending on the impact velocity of the wedge. The reason for this under prediction of wedge velocity in STAR is peculiar. It seems that there may exist a too high air resistance influencing the wedge's acceleration. The mass and initial drop height of the wedge are equal to that of Yettou et al. (2006), hence this discrepancy should not exist.

For a wedge that penetrates the water at a constant velocity (ref. Chapter 3), the magnitude of the spatial pressure distribution does not change over time. For the case of a free-falling wedge, a rapid decrease in velocity is experienced. The result in Figure 4.18 show that this deceleration generates spatial pressure distribution that changes shape with the penetration depth. From a sharp peak seen for transducer 1 at $t \approx 3$ ms, the peak becomes more and more rounded and the peak amplitude decrease drastically.

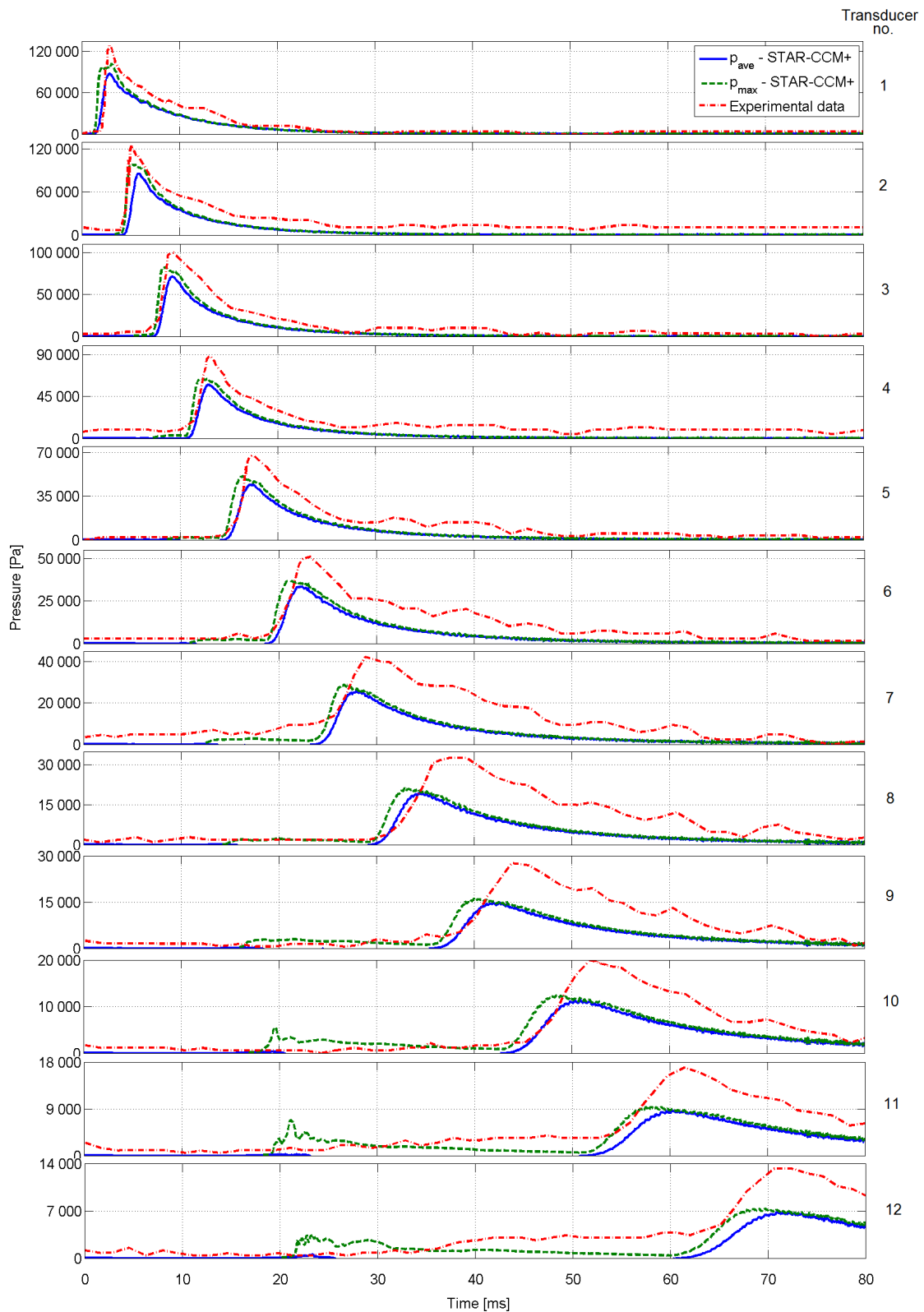


Figure 4.18: Pressure time variation for all 12 transducers for one drop. Presented are pressures recorded by Yettou et al. (2006) and the maximum pressure p_{\max} and the surface averaged pressure over the 19 mm diameter p_{ave} transducer predicted in STAR-CCM+.

In Figure 4.19, the time variation of the peak pressure for the surface averaged pressure p_{ave} , the maximum pressure p_{max} and the peak pressure from the experimental study (left axis) are plotted together with the quadratic velocity v^2 (right axis) of the wedge. For the pressure curves, each marker denotes the transducers 1 to 12, 1 being the one with the highest pressures. The pressure axis is scaled with a factor $A = 6895$ to make comparison easier. It is interesting to note that the pressures behavior is similar to the quadratic velocity curve, proving that the pressure is proportional to the velocity squared. By studying the figure, it is also seen here that the velocity and pressure on each transducer predicted in STAR are underestimated compared to what is found in the experimental study by Yettou et al. (2006).

The influence on the penetration velocity of the mass, the drop height and the deadrise angle of the wedge can be estimated by several simplified analytical models all based on the momentum theorem and the principle of the added mass as developed by Von Karman (1929). In a single approach Wagner (1936) also included the effect of the water splash on the wedge walls (Payne (1988) and Korobkin and Pokhnachov (1988)). Zhao et al. (1996) also added an empirical term to take into account the three-dimensional effect associated with non-infinitely-long body (Mei (1998)). A comparison of the mentioned models and the results obtained through STAR and the experimental study on the deceleration of the wedge shortly after impact is shown in Figure 4.20. Again, it is seen that the impact velocity predicted in STAR is lower than the velocity found by Yettou et al. (2006) in the experimental work. The analytical models coincide quite well with the experimental data, predicting the impact velocity at about 5 m/s.

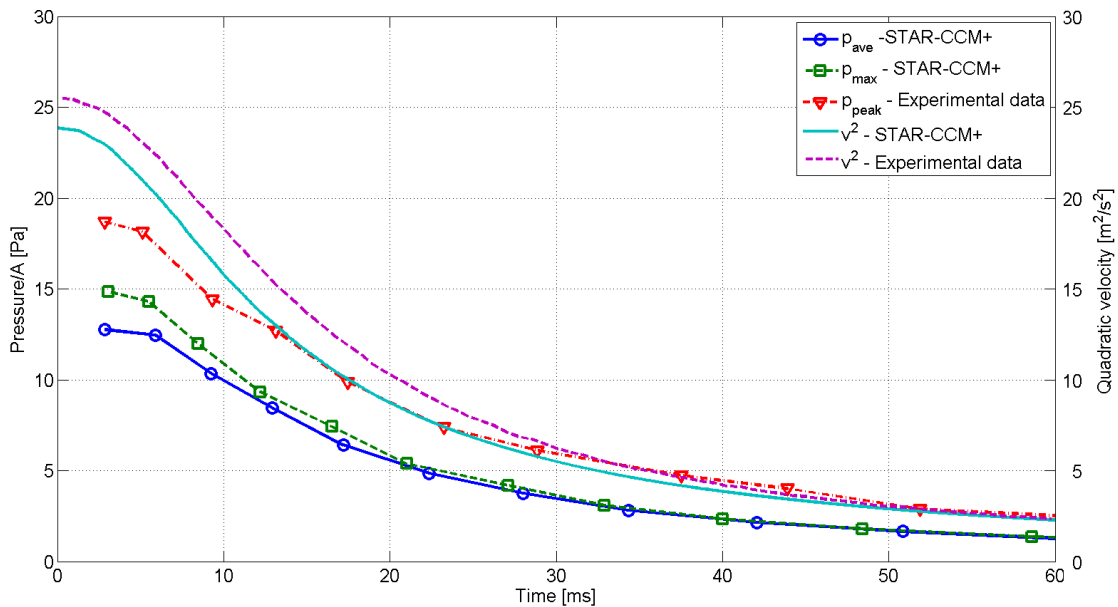


Figure 4.19: The time variation of the peak pressures for the surface averaged pressure p_{ave} , the maximum pressure p_{max} and the peak pressure from the experimental study (left axis) plotted together with the quadratic velocity (right axis) v^2 of the wedge. For the pressure curves, each marker denotes the transducers 1 to 12, 1 being the one with the highest pressures. The pressure axis is scaled with a factor $A = 6895$ to make comparison easier.

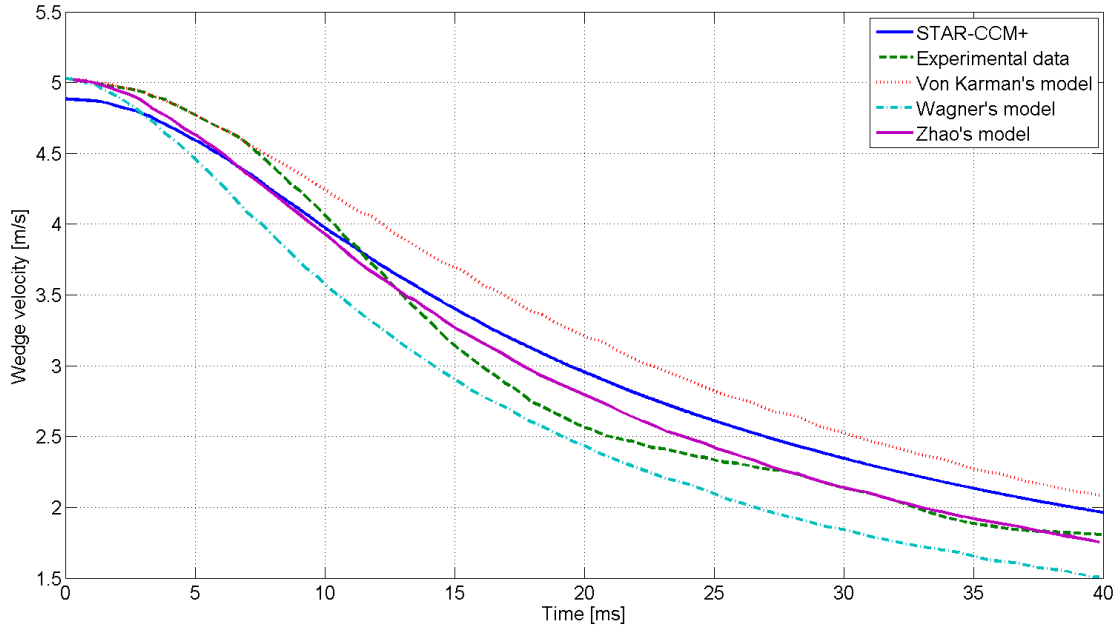


Figure 4.20: Comparison of the analytical models of Von Karman (1929), Wagner (1936) and Zhao et al. (1996), together with the results obtained through STAR and the experimental study, on the deceleration of the wedge shortly after impact.

NON-DIMENSIONAL STUDY

To better describe and compare the results from the numerical prediction in STAR and the experimental work conducted by Yettou et al. (2006), a non-dimensional study is performed. As for the two-dimensional case in Chapter 3, two parameters used to describe the hydrodynamic behavior of the wedge's impact are the dimensionless entry depth $Z = h / \int V(t)dt$ and the pressure coefficient $C_p = p / (0.5\rho V(t)^2)$. Here, ρ is the mass density of the fluid, $V(t)$ is the wedge velocity, t is the time, p is the fluid pressure and h is the vertical height, relative to the apex of the wedge, of a point on the wedge surface as shown in Figure 4.21.

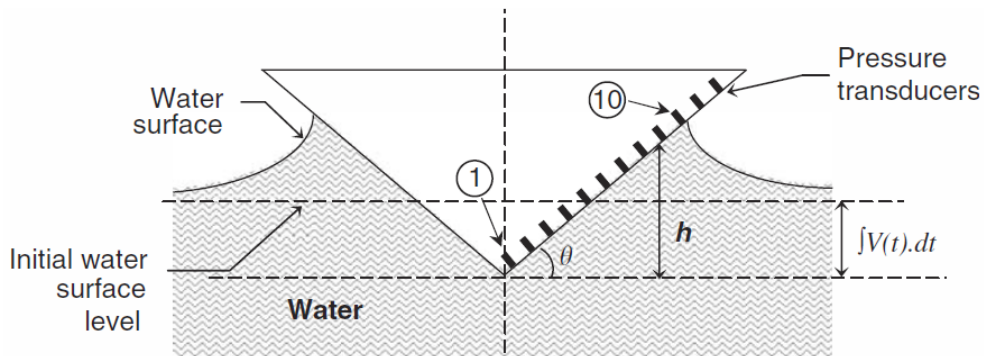


Figure 4.21: The parameters describing the impact of the wedge in water. Yettou et al. (2006)

In the case of a wedge that penetrates the fluid at constant velocity (ref. Chapter 3), it is demonstrated that C_p depends only upon the shape of the wedge. For the free-falling case, however, the velocity varies and hence it is interesting to examine the variation of C_p to analyze the results.

The pressure coefficient C_p and the dimensionless entry depth $Z = h / \int V(t)dt$ for a free-falling wedge will be time-dependent (hence, integration is needed). Therefore, for simplicity, only three time frames are calculated: $t = 9.4, 17.6$ and 22.8 ms. For each time frame, the pressure coefficient is calculated for each transducer in contact with water. By studying Figure 4.18 it is seen that for the mentioned time frames the number of transducers in contact with water are 3, 5 and 6, respectively.

The values C_p and Z for the three time frames are calculated for the surface averaged pressure p_{ave} , the maximum pressure p_{max} and the peak pressure from the experimental study. The results are listed in Table 4.8. The tabulated data together with Mei's model are illustrated in Figure 4.22 to 4.24. Note that for each plot, the markers denotes the transducers on the wedge bottom; 1 (at the apex) being the one to the far left and the last one (not in contact with water) to the far right in the plot. For the experimental study it is seen that the distribution profile of the pressure coefficient estimated at each pressure transducer tends to keep the same shape for the three time frames with a $C_{p_{max}}$ in the order of 11. Similarly, the maximum value for the dimensionless entry depth Z_{max} is also constant at about 1.5. The quantity Z_{max} corresponds to the last transducer in contact with the water during the entry phase. By studying the results obtained through STAR, it seen that the values of C_p are underestimated at each transducer for both the surface averaged pressure p_{ave} and the maximum pressure p_{max} . The discrepancy tends to increase with increasing time frame, i.e. the further the wedge dives through the water. The dimensionless entry depth Z , however, is in good agreement with the experimental data.

As mentioned the Mei model prediction is also plotted in Figure 4.22 to 4.24 (Mei (1998)). It is worthwhile to stress that this model takes into account that the wedge moves at a constant impact velocity. Despite the important difference compared to the situation of a free-falling wedge, the Mei model seem to succeed in predicting the maximum values of the pressure coefficient $C_{p_{max}}$ and the dimensionless depth Z_{max} .

Table 4.8: The values C_p and Z for the surface averaged pressure p_{ave} , the maximum pressure p_{max} and the peak pressure from the experimental study for the three time frames $t = 9.4, 17.6$ and 22.8 ms.

$t = 9.4$ ms						
Trans.	$p_{ave} - STAR$		$p_{max} - STAR$		$p_{peak} - Exp.$	
	C_p [-]	Z [-]	C_p [-]	Z [-]	C_p [-]	Z [-]
1	4.07	0.49	4.20	0.49	5.33	0.49
2	5.49	0.98	6.04	0.98	6.25	0.98
3	6.29	1.47	9.89	1.47	11.32	1.47
4	-0.07	1.55	0.34	1.55	0.04	1.52
$t = 17.6$ ms						
Trans.	$p_{ave} - STAR$		$p_{max} - STAR$		$p_{peak} - Exp.$	
	C_p [-]	Z [-]	C_p [-]	Z [-]	C_p [-]	Z [-]
1	2.18	0.29	2.21	0.29	5.73	0.30
2	2.54	0.58	2.67	0.58	5.22	0.60
3	3.48	0.87	3.74	0.87	6.18	0.91
4	5.54	1.17	6.14	1.17	7.19	1.22
5	8.08	1.46	9.71	1.46	11.06	1.53
6	-0.09	1.55	0.41	1.55	0.06	1.54
$t = 22.8$ ms						
Trans.	$p_{ave} - STAR$		$p_{max} - STAR$		$p_{peak} - Exp.$	
	C_p [-]	Z [-]	C_p [-]	Z [-]	C_p [-]	Z [-]
1	1.44	0.24	1.45	0.24	5.97	0.25
2	1.62	0.48	1.70	0.48	5.20	0.49
3	2.19	0.72	2.34	0.72	5.25	0.74
4	3.28	0.96	3.55	0.96	5.55	0.98
5	5.41	1.20	5.94	1.20	7.74	1.22
6	8.77	1.44	9.54	1.44	10.67	1.47
7	-0.08	1.48	0.50	1.48	0.08	1.48

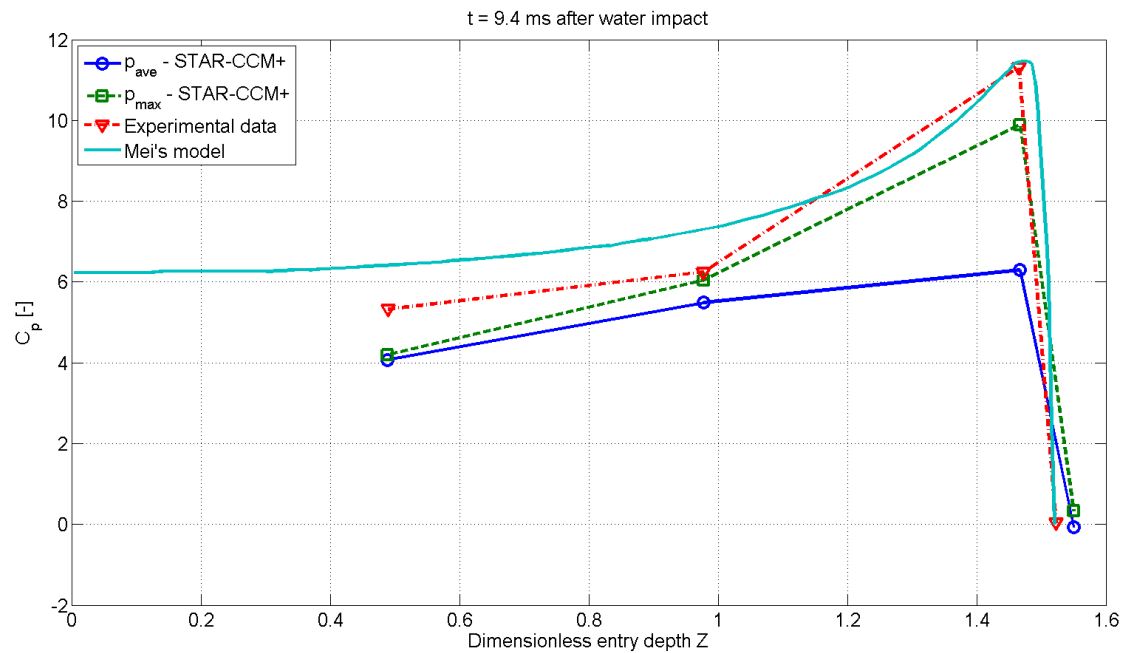


Figure 4.22: Comparison of the pressure coefficient C_p in function of the dimensionless entry depth Z for the surface averaged pressure p_{ave} , the maximum pressure p_{max} and the peak pressure from the experimental study at $t = 9.8$ ms after water impact. The markers denotes the transducers on the wedge bottom; 1 (at the apex) being the one to the far left and the last one (not in contact with water) to the far right in the plot. Mei's model for constant velocity water entry is also included.

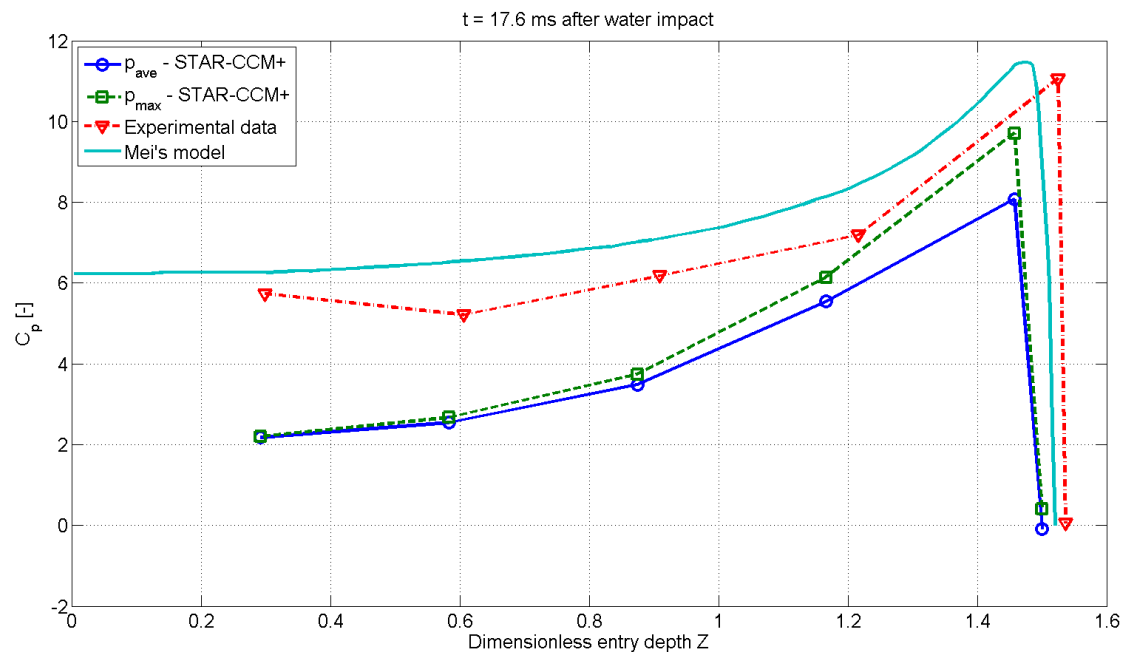


Figure 4.23: Comparison of the pressure coefficient C_p in function of the dimensionless entry depth Z for the surface averaged pressure p_{ave} , the maximum pressure p_{max} and the peak pressure from the experimental study at $t = 17.6$ ms after water impact. The markers denotes the transducers on the wedge bottom; 1 (at the apex) being the one to the far left and the last one (not in contact with water) to the far right in the plot. Mei's model for constant velocity water entry is also included.

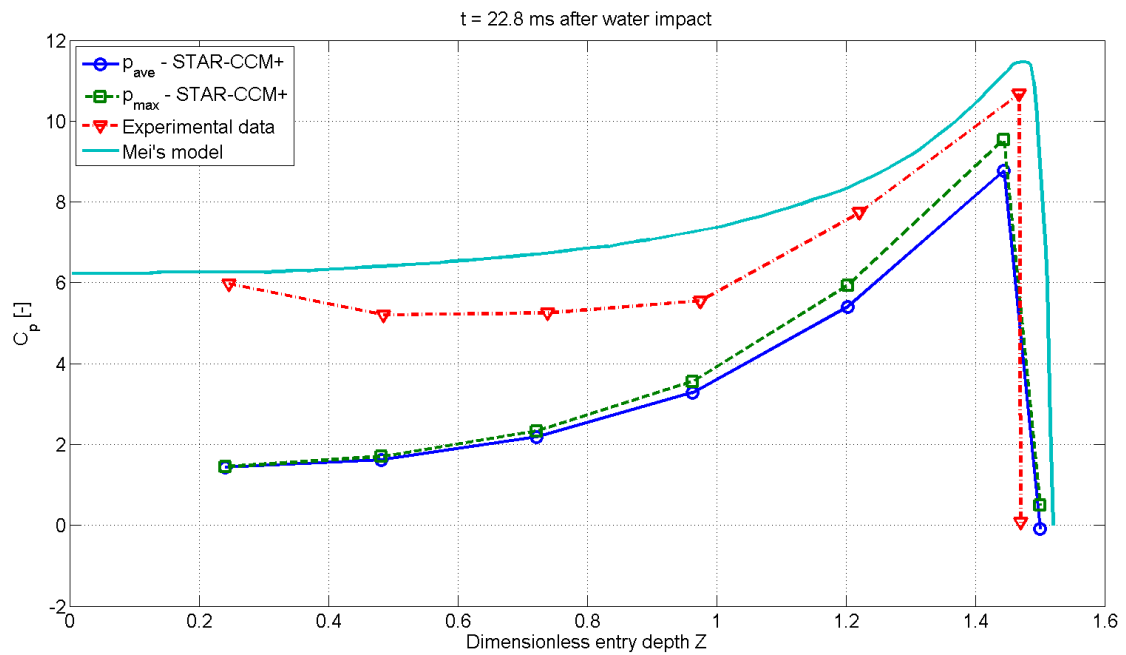


Figure 4.24: Comparison of the pressure coefficient C_p in function of the dimensionless entry depth Z for the surface averaged pressure p_{ave} , the maximum pressure p_{max} and the peak pressure from the experimental study at $t = 22.8$ ms after water impact. The markers denotes the transducers on the wedge bottom; 1 (at the apex) being the one to the far left and the last one (not in contact with water) to the far right in the plot. Mei's model for constant velocity water entry is also included.

HYDROELASTIC IMPACT OF THREE-DIMENSIONAL WEDGES

The dynamic interaction between a structure and fluid is referred to as hydroelasticity (also often called fluid-structure interaction FSI). In general, a dynamic structural response arises if the duration of the impact load is comparable to, or shorter than, the relevant natural period of the structure. For instance, for bow flare slamming on ships, the duration of the slamming load will often be long compared to the short natural period of the hull plating. In such cases, a quasi-static approach is applicable when studying the problem at hand. On the other hand, slamming pressures on the wet deck of a catamaran may give rise to a dynamic structural response in the local plating since the rise time of the pressure is shorter than the plating natural period. Cases where the duration of the impact load is much shorter than the natural period of the structure is referred to as *hydroelastic slamming*.

In marine applications, hydroelasticity is of major interest. This follows from the mutual interaction between structural deformation and fluid particle motion which leads to a "two-way" coupling of the two interfaces (structure and fluid). In these cases the impact-induced pressure and the impact dynamics can highly differ from a quasi-static solution. Following, the analysis of these types of scenarios can be challenging for several reasons. For example, for a wedge during impact, the free-surface is characterized by a thin water jet with velocities that are much larger than the wedge velocity. This leads to a stretching of the free surface leading to an extremely advanced topology. Overturning of the free surface, where it in the end reconnects with itself, makes the task of tracking the free surface practically impossible. This, together with the relative large change in loading which occur as the wedge is deformed, gives rise to complex physical problems.

Research on the phenomena of hydroelastic slamming has up to now mainly dealt with two-dimensional simple problems. Here, solutions combining potential theory for fluids and traditional solution for structure are usually used. Due to its previous mentioned complexity, not much research has been dedicated to the hydroelasticity with three-dimensional impacts. However, recent development in computing technology is making it possible to study the hydroelastic effect for realistic problems by using numerical modeling techniques.

This chapter will present the use of the CFD-software STAR-CCM+ to study free-falling three-dimensional elastic wedges penetrating the free surface. The wedges are of approximately the same geometry as the one studied in Chapter 4, making it possible (to some extent) to compare and evaluate the results from the FSI study. It is stressed

that the FSI study performed in this chapter is conducted to test STAR's possibilities and limitations when it comes to elastic bodies interacting with a fluid. No verification or validation with existing theory or experimental data will be performed. A qualitative assessment of the results will however be carried out. Maki et al. (2010), Panciroli et al. (2011), Aarsnes (2011), Luo et al. (2011)

5.1 FLUID-STRUCTURE INTERACTION IN STAR-CCM+

This section is aimed to describe the various techniques and considerations for fluid-structure interaction (FSI) cases, and how these are dealt with in STAR.

FSI problems in STAR are solved using the finite volume stress capabilities. As an alternative, FSI problems can also be modeled by coupling between STAR to a third party code, whereby STAR solves the fluid domain and the third party code solves for the structure. An example of a third party code which can be used is Abaqus, where the fluid domain from STAR and the structural domain in Abaqus are interconnected using SIMULIA Co-Simulation Engine (CSE).

In this thesis, the FSI study is done solely by the use of STAR, i.e. no third party interaction. In the following, some classifications of the interactions and the capabilities that are needed to address FSI problems in STAR are given. Much of the presented material is a result of CD-adapco (2011) and conversations with Mueller (2012) and Voronkov (2012).

FSI COUPLING

Fluid-structure interaction (FSI), broadly speaking, is the thermo-dynamical interaction of a fluid and a solid structure. The interactions can be grouped into distinct categories:

- "One-way" interactions
- "Two-way" interactions

One-Way Interactions

A case where the fluid may impart some action on the structure but the response of the structure to the fluid loading does little to affect the fluid motion, is referred to as a "one-way" interaction. Take for example a fluid heating a stiff, supported structure. The heating will produce thermal loads and deformations in the solid material, but these deformations will most likely not lead to any significant change in the flow patterns of the fluid. The problem involves a two-way exchange of heat, however, the mechanical exchange is only one way, making it sufficient to compute the temperature in the fluid and solid domains in separate simulations, and then compute the stresses in another simulation using the results of the temperature computed in the previous simulation.

Two-Way Interactions

A case where the fluid motion and pressure affects the displacement and deformation in the structure is referred to as a "two-way" interaction. Consequently the response of the structure has a significant effect on the fluid flow. Traditionally, FSI implies two-way coupling of a fluid and a deformable structure, such that the deformation and rigid body DOF are significantly coupled with the fluid. Further, there are classifications of the degrees of coupling, ranging from "weak" or "loose" coupling to "strong" coupling.

In some FSI problems, the coupling can be regarded as "weak", and a "loose" coupling algorithm can be employed to find the solution. Consider a wedge penetrating the surface with a constant velocity. Depending on the wedge plate thickness, there will be structural deformation or bending of the walls due to the steady-state flow. The deformation can significantly alter the flow patterns around the structure, which, in turn, again affect the deformation. If one is searching for a steady-state condition, one is interested in the shape the structure takes under the steady condition. As time goes, the structure and fluid domain will reach a steady state, where the structure material

point velocities are zero. Here, the structure imparts no motion on the fluid, hence the coupling is "weak." One can also state that it is almost "one-way" since the primary influence of the structure on the fluid is via its velocity, which in steady state is zero. In general, weak coupling implies that the response times of the structure to a disturbance in the fluid are slow, compared to the fluid. Or vice-versa, the response times in the fluid to a disturbance in the solid are slow, compared to the solid.

For a "strong" coupling, the physical coupling is two-way and the coupling between the codes is pronounced. This is often associated with "dynamic" problems where the hydrodynamic loads and the structural velocities change dramatically (as is the case for the water entry of a wedge studied in this chapter). In strong coupling algorithm, the fluid and structure solvers may be resident in the processor memory at the same time and data is passed at regular intervals from the memory used by the structure solver to/from the memory used by the fluid solver. Data between the solvers may be necessary to exchange more than once per time step, depending on the actual strength of the coupling. This implies a deeper communication between the structural and fluid codes and is known by various names: "implicit", "iterative staggered", "iterative successive substitution", or "multiple iterative coupling". When dealing with a light or compliant structure which interacts with a relatively heavy, almost incompressible fluid, an implicit coupling is usually necessary. As an example, a steel structure in water may be strongly coupled if the structure is relatively light compared to the fluid it displaces, again as the case for the water entry of a wedge.

MESH EVOLUTION

When simulating a FSI case, STAR is required to account for the changes of shape for the solid structure. This problem can be solved by various strategies, and in this thesis a *morphing* of the fluid and structure domain is used.

Morphing is the deformation of the fluid grid by moving the fluid vertices in such a manner as to conform to the solid structure and maintain a reasonable quality fluid grid. This is done by altering the cell shape and at the same time ensuring that all cells maintains the same neighboring cell. To account for the arbitrary motion of the fluid mesh, STAR uses a "space conservation law" to conservatively and accurately express the transport motion.

When dealing with FSI there exist two meshes: one for the fluid domain and one for the structural domain. One challenge in FSI lays therefore the difference in the resolution between the fluid and the structure mesh. This difference in mesh is often due to the difference in physical processes in the fluid and the structure. If the two meshes are constructed solely in STAR, the meshes can be made conformal at the fluid-structure interface. This means that the vertex positions on the fluid surface match the vertex positions on the surface of the structure. In the thesis, this is the method applied.

FINITE VOLUME STRESS

To simulate fluid-structure interaction (FSI) within STAR, the *solid stress model* (or "FV stress") is used. Depending on the case at hand, the displacement of the solid domain can either be large or small. At small displacement it is assumed that the displacements are relatively small compared to the cell size, e.g. problems involving high frequency vibrations. In this thesis, where wedge water entry is studied, one says that the solid displacement is large, globally but also locally. Therefore, in the study

involving FSI of the wedge, STAR's *large displacement* model is used.

When dealing with FSI within STAR there are two models which are crucial to activate: the *solid stress* model (where *solid displacement motion* is enabled) in the solid continuum, and the *morphing motion* for the fluid continuum (in the fluid region one must make sure that the mesh morpher motion is enabled such that the fluid domain will morph according to the solid stress displacement).

COMPRESSIBLE FLUID

When modeling water, it may be useful to set the water as compressible by employing the *user-defined density* model. This will increase both numerical stability and accuracy, particularly when the flow is internal to the structure. The compressibility of the fluid is defined by the earlier explained *field functions*. A definition of the ones needed is given in detail in section 5.2. It should be noted that the choice of whether or not to use compressible water depends on the physics and appropriate time scales. Details will not be given here, other than to say that if the physical relevant times scales are of the same order as the sound transit times, then it is necessary to accurately account for the exact nature of the fluid compressibility. The effect of compressible contra incompressible fluid is studied later in section 5.2.

5.2 SOLUTION IN STAR-CCM+

The water entry of free-falling three-dimensional elastic wedges are simulated and studied in STAR. Four different wedges are modeled. Three of the wedges are of equal geometry but different in material properties; glass-reinforced plastic (GRP), aluminum and stainless steel (UNSS30200). The fourth wedge is also made by stainless steel but the wedge walls are thinner compared to the three other wedges. The different material properties are chosen to study the effect of choice of material on the wedge's response as it enters the water. Similarly, the difference in geometry is chosen to study the effect of plate thickness. The "outer" geometry of the wedges is all the same, and only the "inner" geometry is altered to produce the one thin wedge. Further, the "outer" geometry is chosen to replicate the geometry of the three-dimensional wedge studied in Chapter 4. Also, the thickness of the wedges is chosen such that the weight of the wedges is approximately the same as the case for the wedge in the previous chapter. In this way, one is able (to some extent) to compare the results from the FSI study with the one in Chapter 4, and hence conclude if the behavior of the elastic wedges are somewhat realistic (and again, conclude if STAR can be used to study problems concerning hydroelastic slamming).

All wedges are modeled with a deadrise angle $\alpha = 25^\circ$. The drop height is set to 1.3 m, same as for the case in Chapter 4. As for the water entry of two and three-dimensional wedges described in the previous chapters, a laminar flow model is considered sufficient (a laminar vs. turbulent flow study is not done for the elastic wedges). To be able to compare results with those found in Chapter 4, the pressure at transducer 1 (50 mm from the wedge apex, ref. Chapter 4) is recorded. The *solid displacement* model together with a morphing mesh as explained in section 5.1 are used to simulate the free-falling motion of the wedge. To ensure stability in the solution a time step is chosen such that the maximum Courant number at critical regions is approximately equal to 0.5.

All simulations of the 3-D elastic wedges are run on an AMD computer cluster with a total of 24 cores, each at 2.40 Ghz. The wedges are studied for 1 second (real time) and a computational time varying from 8 to 20 hours is recorded.

It should be noted that due to the lack of time, no convergence study on grid size, time step or influence of numerical parameters is conducted. The set-up of the FSI simulations are done based on the experience collected through the studies performed in Chapter 3 and 4, together with conversations with Voronkov (2012) and Mueller (2012). This section will, however, summarize some of the modeling aspects, including choice of grid size, time step and numerical parameters. Lastly, a study on compressible versus incompressible fluid will be presented.

MODELING

The wedge and fluid domain are created in STAR's own CAD environment. As the elastic behavior of the whole wedge is of interest, no symmetry conditions are applied to simplify the wedge geometry (i.e. the wedge is modeled in full). Four wedges are modeled with width \times depth equal to 1.2 m \times 0.05 m. The fluid and air domain is modeled with width \times height \times depth equal to 6 m \times 5 m \times 0.05 and a symmetry condition on the fluid domain's front and back is applied to obtain a quasi-2-D solution (an ok simplification as the transducers in the experiment from Chapter 4 are located at the wedge's median, resulting in close to no side flow at impact).

Properties for the four wedges are shown in Table 5.1. In Figure 5.1, the geometry for the wedge made of GRP is shown. Figure 5.2 shows the front view of the same wedge together with the fluid and air domain.

Table 5.1: Properties of the four wedges modeled in the FSI study.

<i>Material</i>	<i>Thickness [mm]</i>	<i>Density [$\frac{kg}{m^3}$]</i>	<i>Young's modulus [MPa]</i>	<i>Weight [kg]</i>
GRP	10	1800	36 000	2.18
Al	10	2702	68 000	3.27
Steel	10	8055	193 000	9.75
Steel	4	8055	193 000	3.99

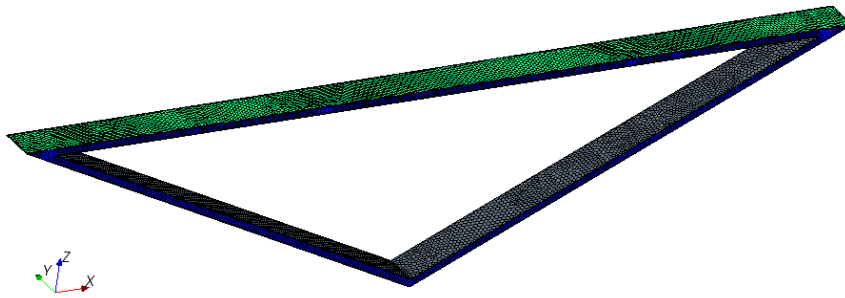


Figure 5.1: The geometry for the wedge made of GRP modeled in STAR.

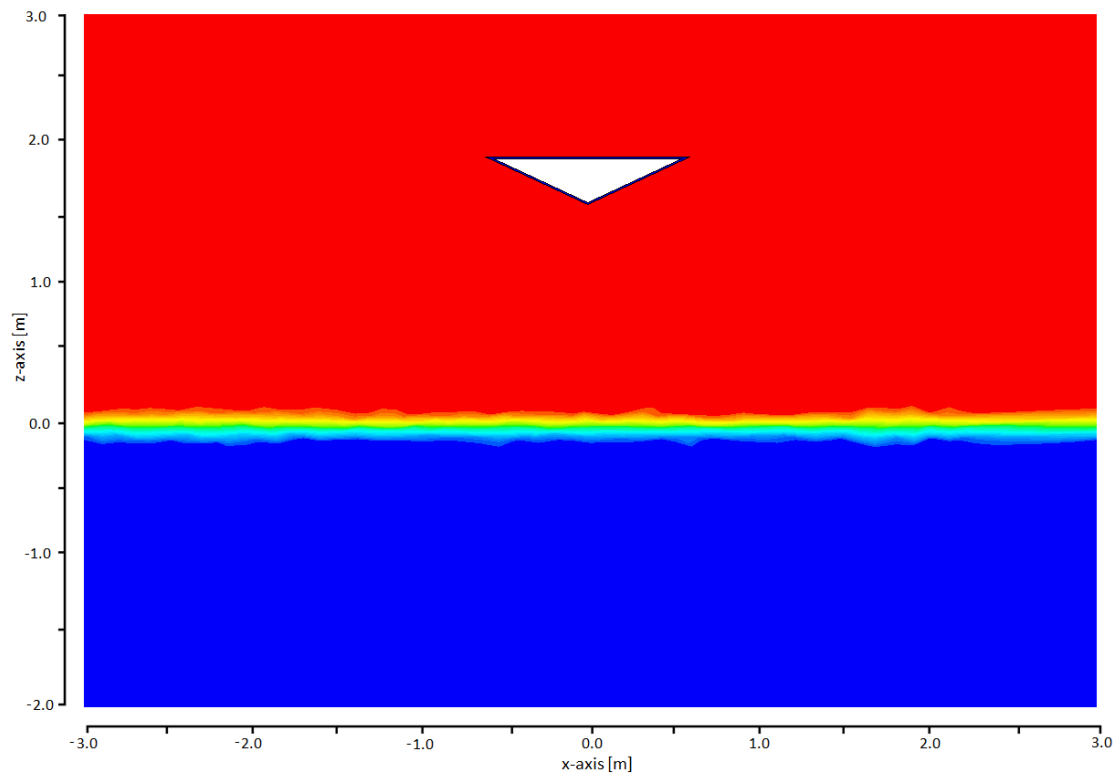


Figure 5.2: Front view of the wedge made of GRP together with the fluid and air domain.

The boundary conditions are set as follows:

- Symmetry: at the domain's and wedge's front and back.
- Velocity inlet: at the domain's bottom and side walls.
- Pressure outlet: at the domain's top.
- Contact interface: between the wedge walls and the fluid/air domain.

DISCRETIZATION OF TIME AND SPACE

When modeling the wedge water entry in STAR, the effect of choice of domain and grid size, including time step, on the results needs to be considered. However, as earlier mentioned, due to the lack of time, this is not done for the FSI case. The following will therefore only present the chosen domain and grid size, together with the selected time step. Some remarks on choice of meshing models are also given.

Domain size

Only one domain size is considered. The choice of size follows from the study performed in the previous chapters together with guidance given by Voronkov (2012). Dimensions of the domain are seen in Table 5.2. A visualization is seen in Figure 5.2.

Table 5.2: The domain used in the FSI study. The coordinates are seen in connection with Figure 5.2.

	x_{\min}	x_{\max}	y_{\min}	y_{\max}	z_{\min}	z_{\max}
Domain	-3.0	3.0	-0.025	0.025	-2.0	3.0

Grid size

In Chapter 3 and 4 the *trimmer* meshing model is used on the whole fluid domain. When FSI is studied, one is required to use morphing, and hence a trimmer model is not (always) ideal. Various approaches can be used when generating a mesh for a FSI case. In this thesis, three meshing models are used: the embedded thin mesher, the polyhedral mesher and the surface remesher. When dealing with FSI, there exists two physics continuum: one for the domain and one for the wedge. Following, two mesh continua can be generated: one for the domain and one for the wedge. As discussed in section 5.1, one challenge lies in the resolution between the fluid and the wedge mesh. In this thesis this problem is overcome by the use of the thin meshing model. This model allows the use of only one mesh, both for the domain and the wedge, by ensuring a conformal mesh at the fluid-structure interface. The model also performs a meshing of the wedge with thin layers, such that stresses within the solid can be correctly solved. An illustration of the grid generated by the three models is shown in Figure 5.3. Notice how the thin mesher makes the cells on the wedge rectangular. Notice also that the vertex positions on the fluid surface match the vertex positions on the surface of the wedge (white circle in the bottom picture).

As opposed to the grids used in the previous chapters, no grid refinements are done for the FSI study. There are two reasons for this. The first is caused by the limitations in constructing interfaces between the fluid and wedge domain. The transducers on the wedge bottom modeled in Chapter 4 requires patches to be created on the wedge surface. For the FSI study these needs also to be created in the fluid domain, as there needs to be an interface between the wedge and domain at each transducer surface. This

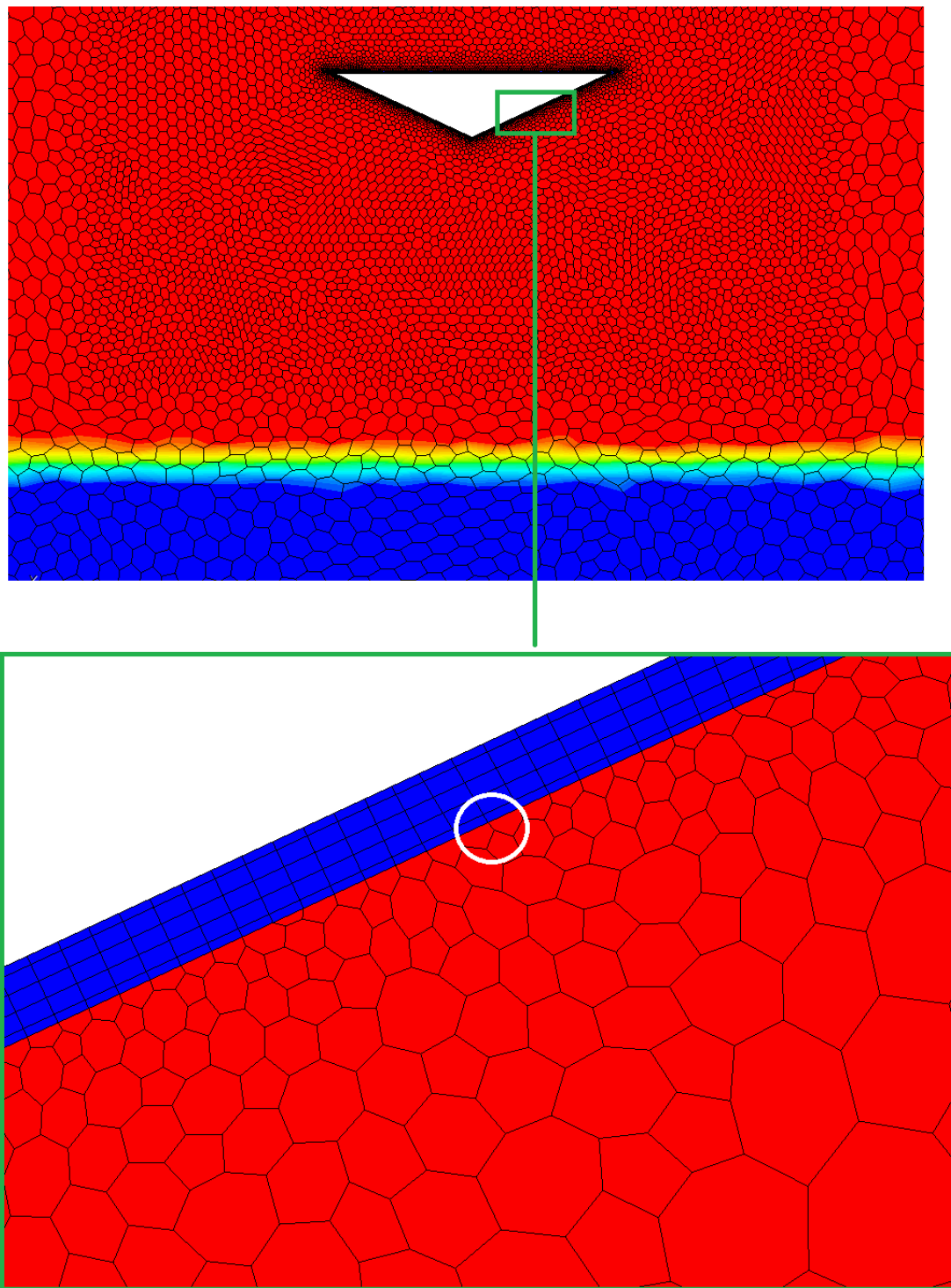


Figure 5.3: The grid used in the FSI study. Notice that the vertex positions on the fluid surface match the vertex positions on the surface of the structure (white circle in the bottom picture).

operation, of multiple interfaces is seen to confuse STAR and therefore no transducers are created on the wedge surface. This again implies that no local refinements of the

type seen in Figure 4.8 in section 4.2 in the previous chapter, is applied¹.

To be able to record the pressure at the first transducer, a pressure probe is used. The probe is placed at the same place as the transducer closest to the wedge apex. The probe follows the motion of the cell face it was originally located at and records the maximum pressure at this cell as the simulation moves along. As the main object is to study slamming pressures at water impact, one would anyway expect the use of grid refinements in critical areas, such as in the vicinity of the probe. This is however not done due to reason number two: time. A dramatic increase in computational time is experienced as the cell number is increased. Hence, the local refinements are left out in all simulations concerning FSI.

As mentioned, no convergence study is performed by altering the grid size. In short, two different sizes are used: one for the three wedges with thickness equal to 10 mm (Grid 1) and one for the wedge with thickness equal to 4 mm (Grid 2). The reason for the two different grids is due to the automatic refinement created by the mesh models as the wedge gets thinner. Properties of Grid 1 and 2 are shown in Table 5.3. Note that the grids are made out of polyhedral cells and rectangular cells (ref. Figure 5.3). Their spatial extent are denoted Δx_{pol} and Δx_{rec} , respectively.

Table 5.3: The four different grids used in the grid size analysis. Δx_{\min} and Δz_{\min} denotes the extent of the smallest cells.

	Cells	$\Delta x_{pol_{\min}}$ [m]	$\Delta z_{pol_{\min}}$ [m]	$\Delta x_{rec_{\min}}$ [m]	$\Delta z_{rec_{\min}}$ [m]
Grid 1	86 253	0.0038	0.0034	0.0047	0.0024
Grid 2	87 165	0.0035	0.0030	0.0046	0.0005

Time step

No study on time step is performed. It is chosen based on experience from the previous chapters and guidance from Voronkov (2012). As a result, the time step in the FSI study for all simulations is set constant and equal to 0.0002 s.

CHOICE OF NUMERICAL PARAMETERS

When setting up a CFD simulation in STAR a number of input parameters needs to be chosen. No convergence study is done to decide on which values to apply to obtain the most satisfactory result. The choice of values are done based on experience and guidance from Voronkov (2012). Choices are presented in Table 5.4. Further study of the set-up and simulations can be done on the *.sim* files found in the folder *wedge3D_elastic* found in the attached ZIP-file.

COMPRESSIBLE VERSUS INCOMPRESSIBLE FLUID

As earlier stated, when modeling water, it may be useful to set the water as compressible by employing the *user-defined density* model. This will increase both numerical stability and accuracy, particularly when the flow is internal to the structure. The compressibility of the fluid is defined by use of the *field functions*. In this case, six field functions are needed to properly model the compressibility of water and air. The field function are each used in the material properties as density ρ , density pressure derivate $\frac{d\rho}{dp}$ and speed

¹It should be noted that the student has limited skills in the use of the software, hence others approaches may be applied to solve for this mismatch.

Table 5.4: Parameters chosen in the simulations for the FSI study.

	Parameter	Tested	Chosen
<i>Physics</i>			
	Segregated Flow	Convection	- 2nd-order
	Segregated Multiphase Temp.	Convection	- 2nd-order
	Volume of Fluid	Convection	- 2nd-order
<i>Solver</i>			
	Implicit Unsteady	Temporal Discretization	- 1st-order
	Segregated Flow	Under-Relaxation: Velocity	- 0.7
	Segregated Flow	Under-Relaxation: Pressure	- 0.1
	Segregated VOF	Under-Relaxation	- 0.4
	Segregated Energy	Under-Relaxation: Fluid	- 0.9
	Segregated Energy	Under-Relaxation: Solid	- 0.99
<i>Stopping Criteria</i>			
	Iterations	Number of Inner Iterations	- 10

of sound c . Their definitions are seen in Table 5.5. Note that the "assembly code" is the definition required in STAR.

Table 5.5: The different material properties defined in STAR to achieve compressibility in water and air.

Material property	Definition	Assembly code in STAR
<i>Speed of sound c</i>		
Air	$c_{air} = 331$	331
Water	$c_{water} = 1450$	1450
<i>Density pressure derivative $\frac{d\rho}{dp}$</i>		
Air	$\frac{d\rho_{air}}{dp} = \frac{1}{c_{air}^2}$	(/ 1 (pow \$ { c_{air} } 2))
Water	$\frac{d\rho_{water}}{dp} = \frac{1}{c_{water}^2}$	(/ 1 (pow \$ { c_{water} } 2))
<i>Density ρ</i>		
Air	$\rho_{air} = \rho'_{air} + \frac{p_{air}}{c_{air}^2}$	(+ 1.18415 (/ \$ { p_{air} } ... (pow \$ { c_{air} } 2)))
Water	$\rho_{water} = \rho'_{water} + \frac{p_{water}}{c_{water}^2}$	(+ 997.561 (/ \$ { p_{water} } ... (pow \$ { c_{water} } 2)))

The effect of compressibility is studied with respect to velocity, acceleration, displacement, slamming pressure and deflection of the wedge bottom. Two test cases are performed: one where the wedge is simulated in a compressible fluid/air environment, and one where the fluid/air environment is incompressible. In both cases the 10 mm steel wedge is used, dropped from an initial height of 1.3 m. The study is performed from the initial height of 1.3 m at $t = 0$ s and run for a total of 1 s. The wedge's impact with water is at $t = 0.52$ s. The slamming pressure is recorded by the pressure probe 50 mm up the wedge bottom's right side as seen in Figure 5.4. The deflection is measured half-way up the wedge bottom's right side, also seen in Figure 5.4. Notice from the figure that for the deflection, the coordinate system is defined with its origin half-way up the wedge side. Results are plotted in Figure 5.5 to 5.9

By studying the figures 5.5 to 5.9, no significant deviations are seen in the results for the compressible and incompressible domain. However, some discrepancy exists between the results obtained in STAR and what one should expect from theory. This is discussed in the following.

The wedge displacement curves are shown in Figure 5.5. Here, it is noticed that wedge displacement is slightly higher in the compressible domain. This is as expected, as the water is compressed as the wedge travels through it (i.e. the wedge is able to dive deeper into the fluid). The result is consistent when considering the wedge velocity plotted in Figure 5.6. Here, the velocity for the wedge simulated in the compressible environment is seen to decrease less after impact (compared to the velocity in the incompressible environment). Again, this is caused by the water that is "giving in" as the wedge travels through it. The difference in velocity is seen at $t = 0.55$ s all the way to $t = 1$ s.

What concerns discrepancy, some is seen for the acceleration in Figure 5.7. From Figure 5.6 one should expect that as the decrease in velocity in the compressible fluid is smaller than for incompressible fluid, this should also apply for the accelerations. However, by studying Figure 5.7, it is seen that the acceleration of the wedge is higher for the case with compressible fluid. This should not be the case. From the two latter figures, oscillating values are seen starting around $t = 0.6$ s. These oscillations are likely to originate from the deflection of the wedge bottom as it travels through the water.

The pressure-time history recorded by the pressure probe is seen in Figure 5.8. From the two graphs it is seen that compressible fluid tends to give slightly larger pressures than the incompressible fluid. This result is a little peculiar as one would expect higher pressures when the wedge hits an incompressible fluid. One explanation can be that large pressures arises inside the fluid as it is compressed, causing higher pressures to act on the pressure probe.

Figure 5.9 shows the deflection of the wedge bottom measured half-way up the wedge bottom (ref. Figure 5.4) in both a compressible and incompressible environment. A negative deflection is seen during the free-falling phase (this is likely due to the weight of the wedge), and at impact the wedge side is deflected inwards; as expected. For the compressible environment the wedge is seen to have a larger negative deflection prior to impact. Further, at and after impact, oscillations with approximately the same amplitude are seen for the two cases, first in-phase and then a "lag" for the case of compressibility.

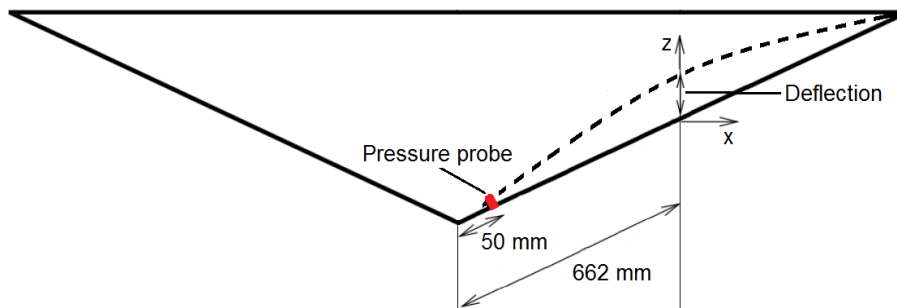


Figure 5.4: Location of pressure probe and measured deflection in the FSI study.

The discrepancy seen for accelerations and pressures should be examined further as suggested in section 6.4 in Chapter 6.

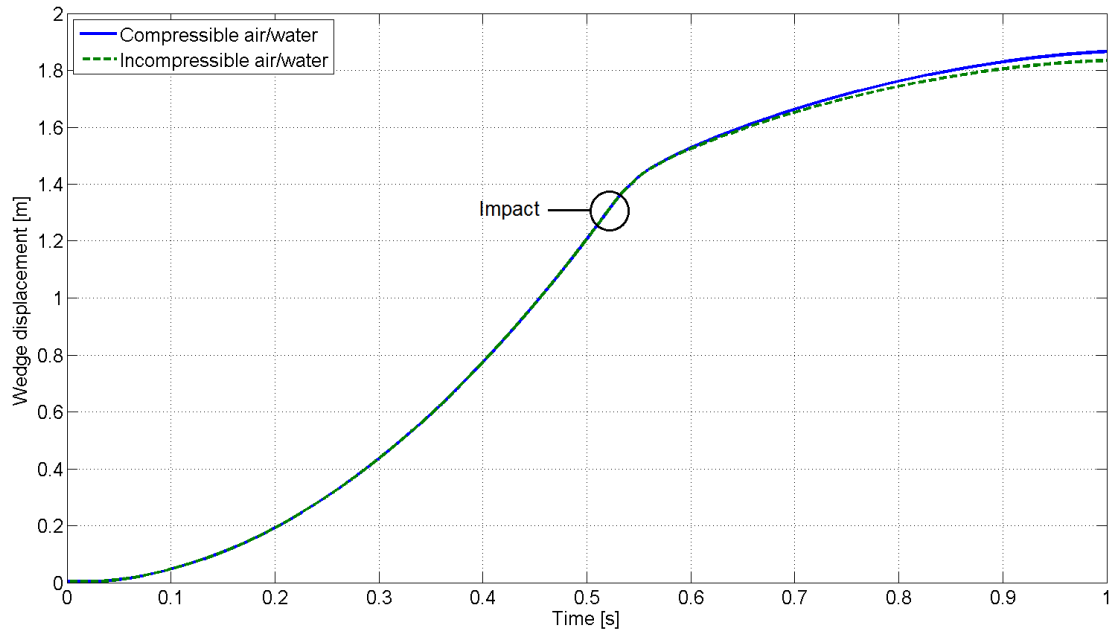


Figure 5.5: The wedge displacement predicted in STAR for the 10 mm elastic steel wedge simulated in a compressible and incompressible environment.

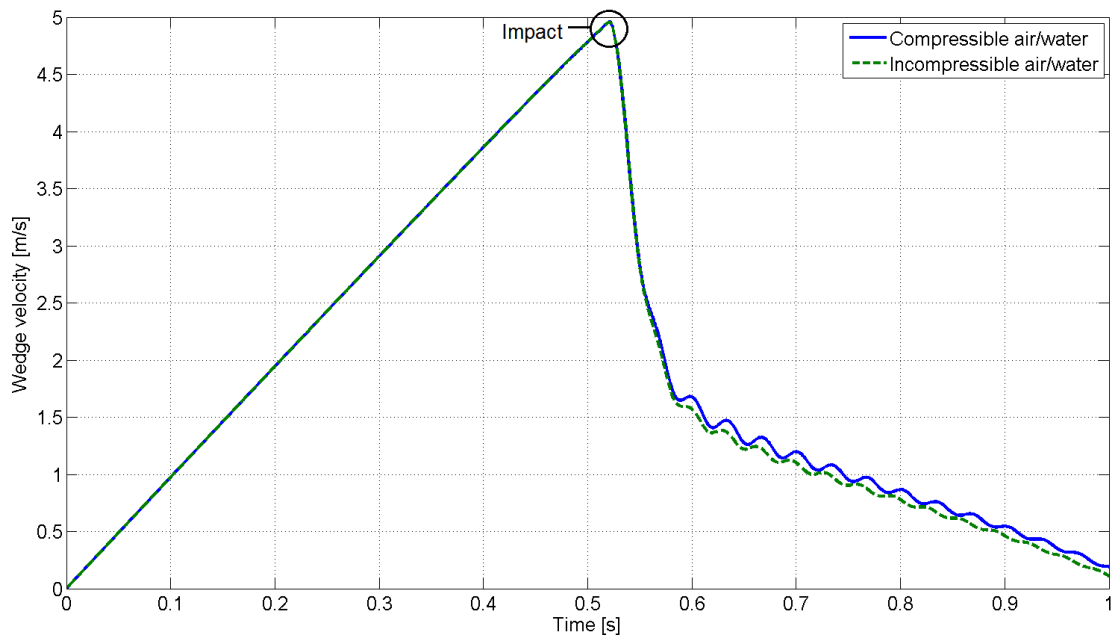


Figure 5.6: The wedge velocity predicted in STAR for the 10 mm elastic steel wedge simulated in a compressible and incompressible environment.

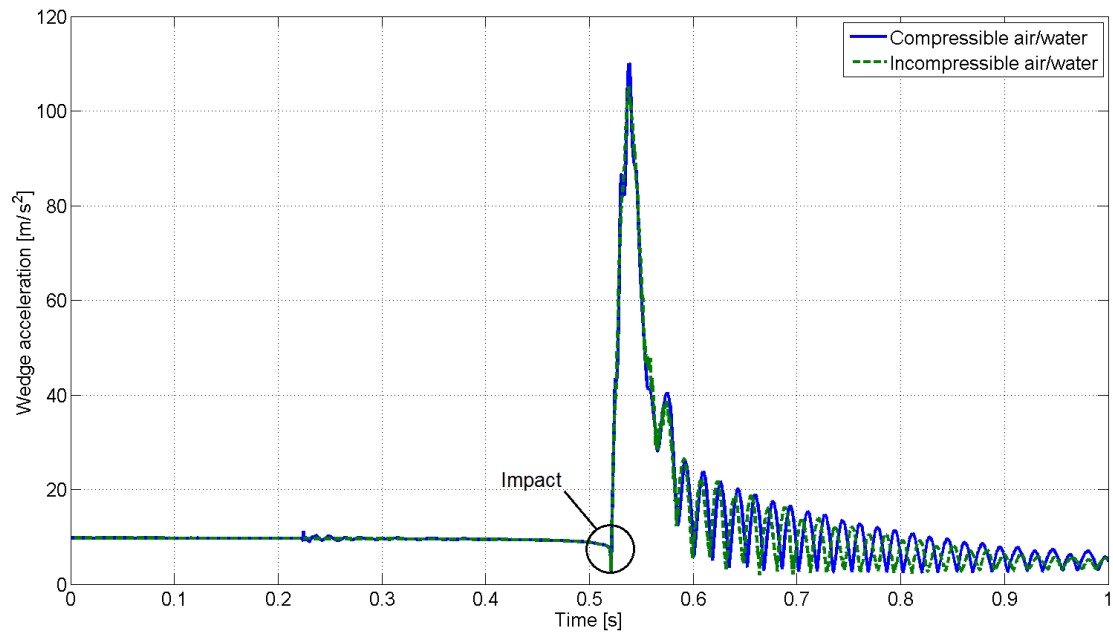


Figure 5.7: The wedge acceleration predicted in STAR for the 10 mm elastic steel wedge simulated in a compressible and incompressible environment.

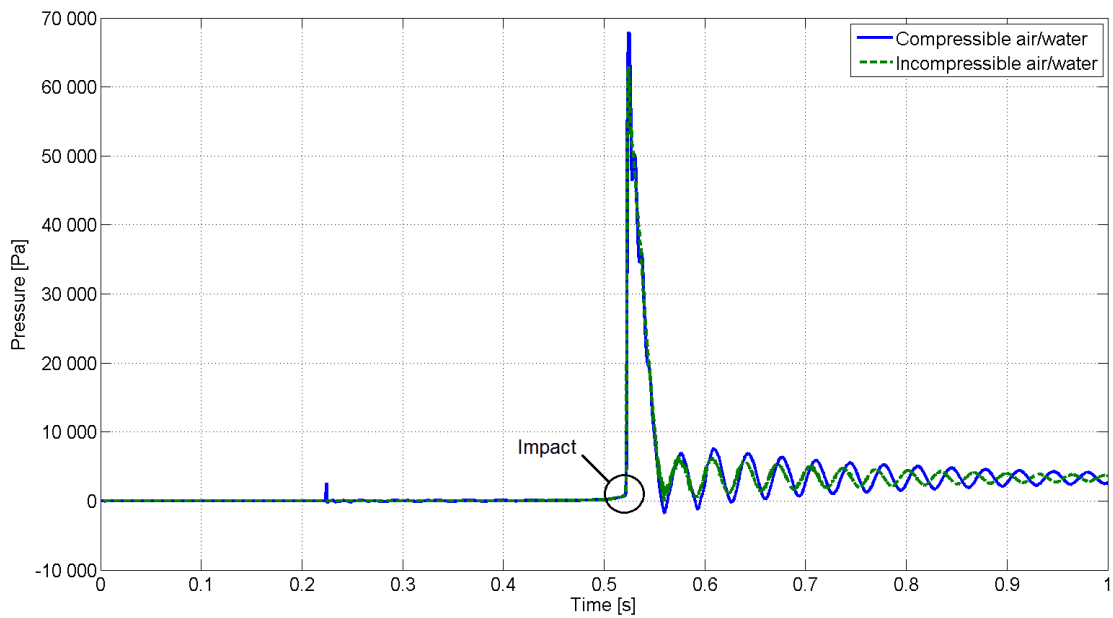


Figure 5.8: The pressure predicted in STAR for the 10 mm elastic steel wedge simulated in a compressible and incompressible environment. Pressure is measured by the pressure probe, 50 mm from the wedge apex.

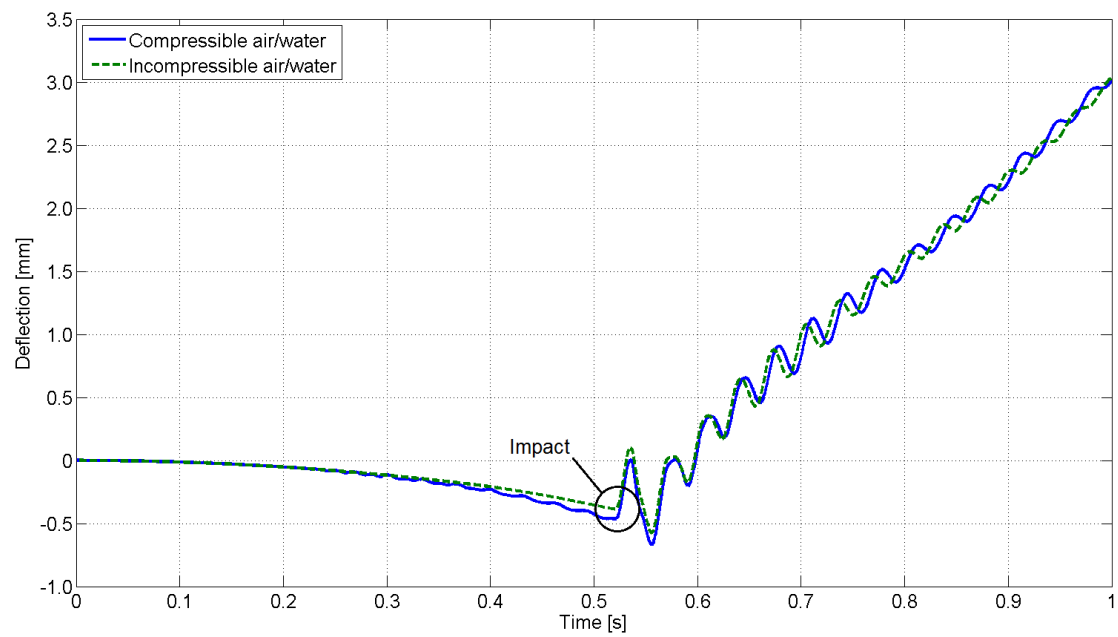


Figure 5.9: The deflection predicted in STAR for the 10 mm elastic steel wedge simulated in a compressible and incompressible environment. Deflection is measured half-way up from the wedge apex.

5.3 RESULTS

From the compressible versus incompressible fluid study, little difference is found in choice of fluid model. Use of compressible water and air seems to give slighter higher pressures and is therefore applied for all simulations. The domain is kept constant with dimensions as shown in Table 5.2 and Figure 5.2. Two different morphing grids are applied with properties as shown in Table 5.3. The time step for all simulations is set constant and equal to 0.0002 s. Numerical parameters are chosen as seen in Table 5.4. The simulation is inspected 0.8 s after impact to ensure a reasonable sharp interface is predicted with a rapid variation of volume fraction across 2 to 3 cells only. Figure 5.10 shows the solution of the 4 mm thick steel wedge at this time instant. It's noticed that the sharp interface requirement is to some extent acceptable. However, one should do refinements at the free surface and the wedge's upper corners to obtain a better resolution of the water jet. Figure 5.10 is also inspected to verify the deflection of the elastic wedge.

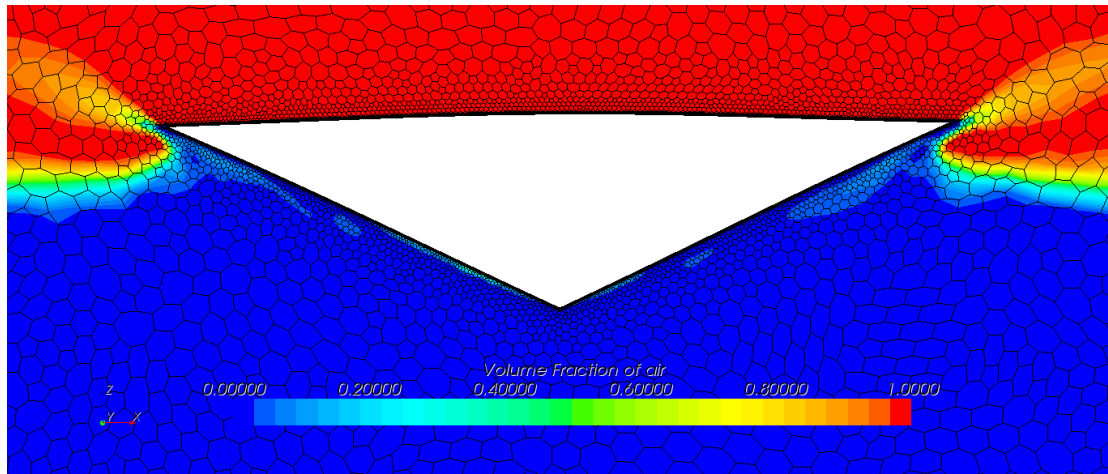


Figure 5.10: The 4 mm thick steel wedge at $t = 0.8$ s after water impact. Notice the volume fraction of the free surface and the deflection of the elastic wedge top and sides.

RAW DATA ANALYZES

The behavior of four different elastic wedges is studied. Their properties are shown in Table 5.1. For each simulation the recorded values are: wedge displacement, wedge velocity, wedge acceleration, the pressure 50 mm from the wedge apex (ref. Figure 5.4), the deflection of the wedge bottom (half-way up) and the Von Mises stress within the wedge. The study is performed from $t = 0$ s (where the wedge is released) to $t = 1$ s. The results are shown in Figure 5.11 to Figure 5.17. The maximum values in the given time domain is given in Table 5.6. Pressure and deflection is measured at locations seen in Figure 5.4.

From its initial position, 1.3 m above the mean water level, the displacements of the four wedges are studied. The displacements curves are plotted in Figure 5.11. From the curves it is seen that the steel wedge of 10 mm thickness is the one diving deepest into the water. The second largest is the 4 mm steel wedge, then the aluminum wedge, and lastly, the wedge constructed by GRP. The results are consistent with what is seen for the velocity plotted in Figure 5.12, i.e. higher impact velocity result in higher penetration depth. The difference in velocity is seen in connection with the weight of the wedges which is seen in Table 5.1. The larger the weight of the wedge is, the less the wedge will be influenced by the air resistance. From this it follows that the impact

Table 5.6: Maximum values of displacement, velocity, acceleration, slamming pressure, deflection and Von Mises stresses for the four different elastic wedges.

	<i>GRP 10 mm</i>	<i>Al 10 mm</i>	<i>Steel 10 mm</i>	<i>Steel 4 mm</i>
Displacement [m]	1.55	1.60	1.87	1.77
Velocity [m/s]	4.61	4.75	4.96	4.80
Acceleration [m/s ²]	149.4	141.4	110.1	145.6
Pressure [Pa]	46 000	54 700	67 720	66 530
Deflection [mm]	6.16	2.88	3.01	13.91
Von Mises stress [MPa]	4.24	5.93	12.12	19.31

velocity will be highest for the 10 mm steel wedge. Following, this wedge will have a higher velocity than the other wedges; seen all the way from $t = 0.55$ s. Notice also the slight different in time of impact due to the difference in velocity. Some discrepancy is seen for the 4 mm steel wedge at $t = 0.71$ s. This is likely caused by numerical errors. The oscillations seen for all the velocities at $t \geq 0.6$ s likely caused by vibrations in the wedge and instability in the solution.

At water impact the wedges will experience large decelerations caused by the density of water. The magnitude of the acceleration is, in contrast to the velocity, decreasing with the increasing weight of the wedge. This is as expected as the larger the weight of the wedge is, the longer time it will take to slow it down (i.e. a lower deceleration). Accelerations for the four wedges are seen in Figure 5.13. Here, the difference in accelerations is clearly seen for the GRP wedge (smallest mass) and the 10 steel wedge (largest mass). Some discrepancy is seen for the aluminum wedge and the 4 mm steel wedge; as the weight of the aluminum wedge is smaller, one would expect the acceleration to be higher than for the 4 mm steel wedge. The difference is however small and may be caused by the deflection of the thin steel wedge (4 mm compared to the aluminum's 10 mm). The oscillations seen for all the accelerations at $t \geq 0.54$ s are likely caused by vibrations in the wedge and instability in the solution.

Figure 5.14 shows a better resolution of the accelerations at $t = 0$ to $t = 0.2$ s. As seen, the initial acceleration for all wedges are equal to 9.81 m/s^2 . However, as the wedge starts to fall, the air drag influences the wedge accelerations, causing a decrease in acceleration determined by the wedge mass. This again affects the impact velocity of the wedge, as seen in Figure 5.12. (The peak amplitude at $t = 0.065$ is caused by a numerical error.)

In the elastic wedge study (FSI), pressure is captured by a pressure probe placed at the wedge bottom 50 mm from the wedge apex (ref. Figure 5.4). As seen in the previous chapters for the rigid wedges, the slamming pressure is dependent on the impact velocity of the wedge. This consistent with what is found in the results for the elastic wedges presented in Figure 5.15. Here, it is seen that the wedge with highest velocity (the 10 mm steel wedge, i.e. largest mass), is the one experiencing the highest impact pressure. Similar, the wedge with the lowest velocity (the GRP wedge, i.e. lowest mass), experiences the lowest impact pressure. It is noted that although the impact velocities are approximately the same for the elastic wedges as for the rigid wedge in Chapter 4, the peak pressures are not. For the rigid wedge a peak pressure of 128 000 Pa is recorded at transducer 1, while the peak pressure at the pressure probe in the FSI study is found at 68 000 Pa for the 10 mm steel wedge. This difference is caused

by difference in grid size and time step. As earlier stated, due to lack of time, no grid refinements around the critical areas are done for the four elastic wedges. Following, STAR will not be able to capture the slamming pressures, due to their small extent in space and time. As the grid size and the time step is decreased one would expect an increase in peak pressure recorded by the probe on the elastic wedge. The oscillations around zero for all the pressures at $t \geq 0.56$ s are due to the variation of pressure (under and over) in the fluid.

As the elastic wedge penetrates the water, the hydrodynamical forces exerted on the wedge will cause the wedge sides and top to deflect. In this study, deflection is measured at the wedge right-hand side as illustrated in Figure 5.4. The results are plotted in Figure 5.16.

The deflection of the wedge's sides is dependent on the wedge's thickness and Young's modulus (as given in Table 5.1). From the deflection curves, it is seen that this holds for the three wedges of thickness 10 mm. Of the three, GRP is the one with lowest Young's modulus and hence, its deflection is largest. Of aluminum and steel, aluminum has the lowest Young's modulus, and therefore, will deflect the most (some inconsistency is seen at $t > 0.95$ s. Further, it is seen that the steel wedge with 4 mm thickness (i.e the thinnest wedge) is the one experiencing the highest deflection; 14 mm at $t = 0.98$ s.

Some different behavior of the deflection is seen prior to impact for the four wedges. Both the 10 mm steel wedge and the GRP wedge seem to have negative deflection as they travel through the air. The 4 mm steel wedge and the aluminum have, however, a positive deflection. The reason for this behavior is for the student unknown. Further, the oscillations seen for all deflections at $t \geq 0.56$ s are either caused by the small vibrations or numerical errors.

The deflection of the wedge gives rise to internal strains and stresses. The stresses are dependent on the wedge's Young's modulus and deflection (strains). The higher the Young's modulus, the harder it is to deflect the wedge. It follows that for given deflection for two materials (equal in geometry), the material which possesses the highest Young's modulus will experience the highest stresses. In Figure 5.17, the maximum Von Mises stresses in each of the four elastic wedges are plotted. The stresses dependence on Young's modulus is illustrated when considering the 10 mm aluminum and steel wedge. From the previous figure, Figure 5.16, the two wedges are seen to have approximately the same deflection. Their Young's modulus, however, differs a lot: 68 000 MPa for aluminum and 193 000 Mpa for steel. This causes higher internal stresses in the steel wedge, in fact, almost by a factor of 2 compared to the aluminum wedge. The GRP wedge, which experience a slighter higher deflection, experience the lowest internal stresses. This is due to the GRP material, which has the lowest Young's modulus of the three different materials. The wedge which experience the highest stresses are the 4 mm steel wedge, caused by the large deflection (14 mm) seen in Figure 5.16 and the high Young's modulus (193 000 Mpa). The oscillation of stresses are caused by the dynamic response of the wedge.

It should be stresses that structural effects caused by deflection of a material are many, and that the student sees it beyond the scope of this thesis to further investigate such effects.

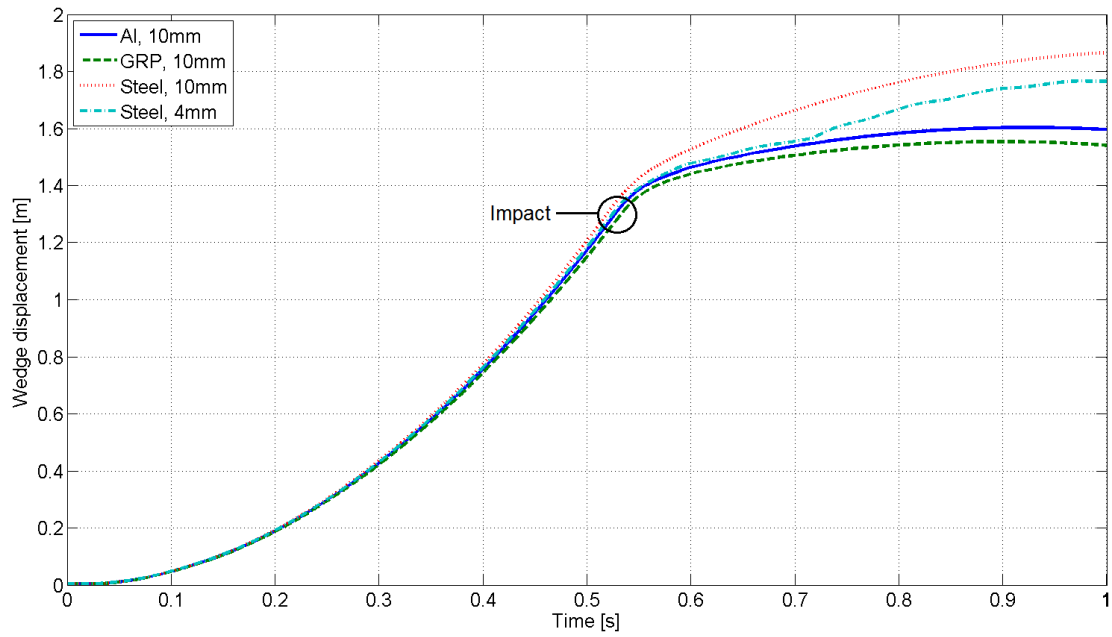


Figure 5.11: The displacement predicted in STAR for the four different elastic wedges.

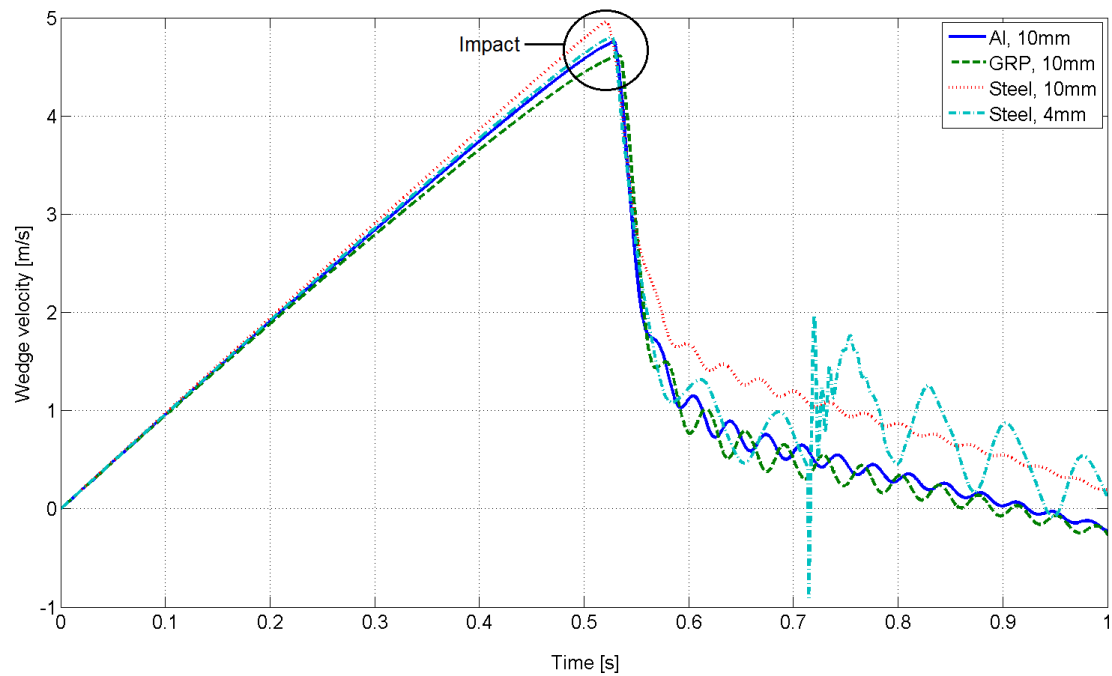


Figure 5.12: The velocity predicted in STAR for the four different elastic wedges.

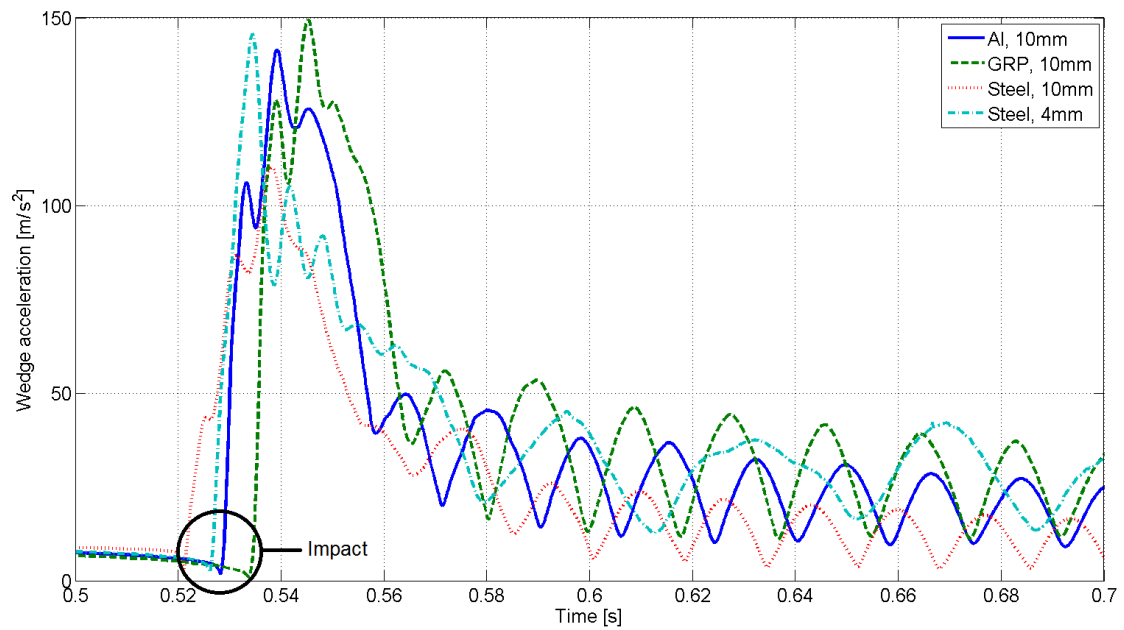


Figure 5.13: The accelerations predicted in STAR for the four different elastic wedges.

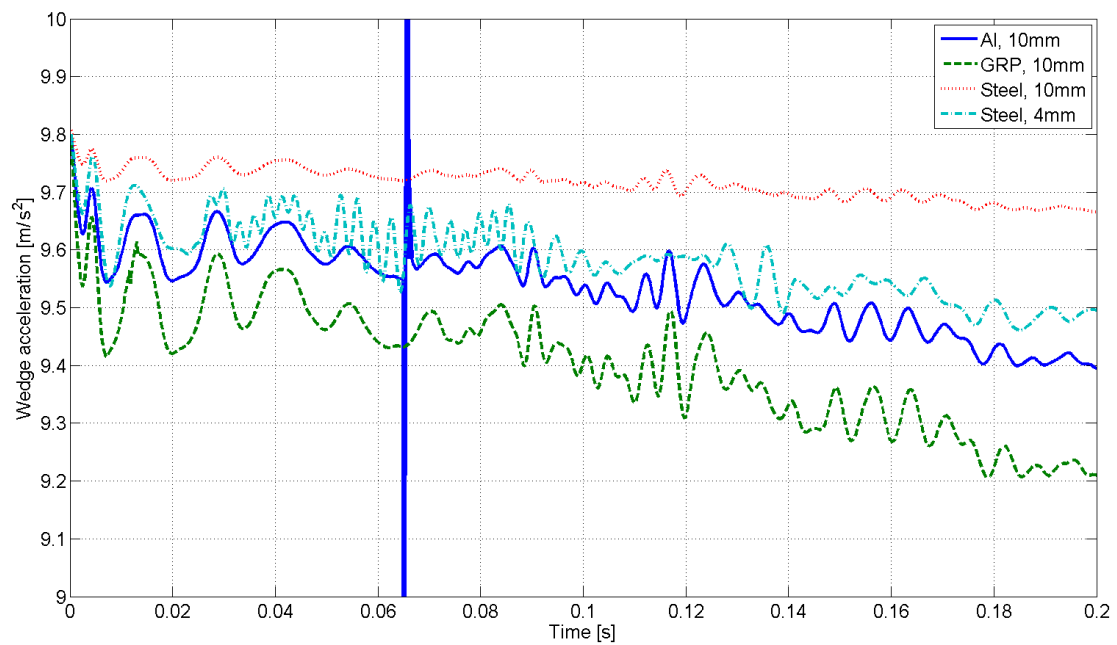


Figure 5.14: The effect of air resistance on the acceleration of the four different elastic wedges.

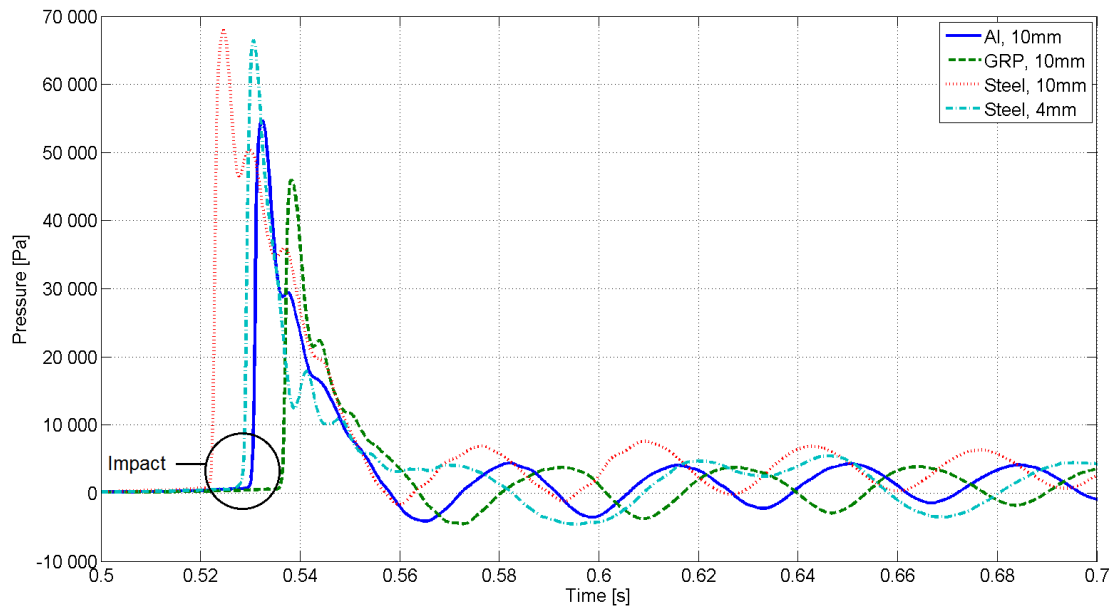


Figure 5.15: The pressure predicted in STAR for the four different elastic wedges. The pressure is measured by the probe 50 mm away from the wedge apex (ref. Figure 5.4).

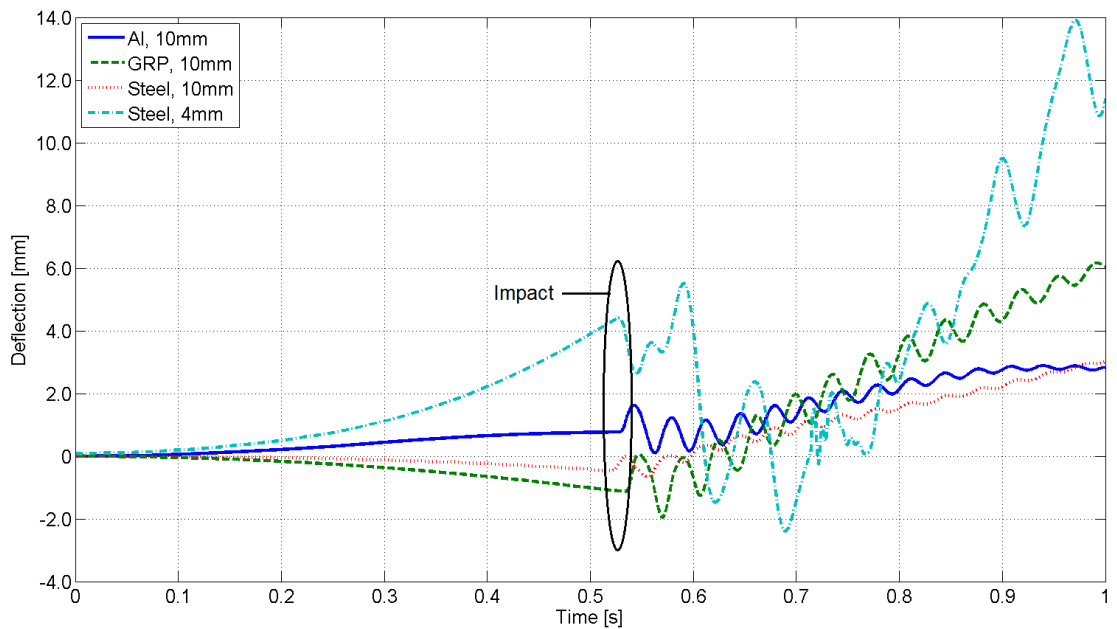


Figure 5.16: The deflection half-way up the wedge bottom predicted in STAR for the four different elastic wedges. Point of measurement is seen in Figure 5.4.

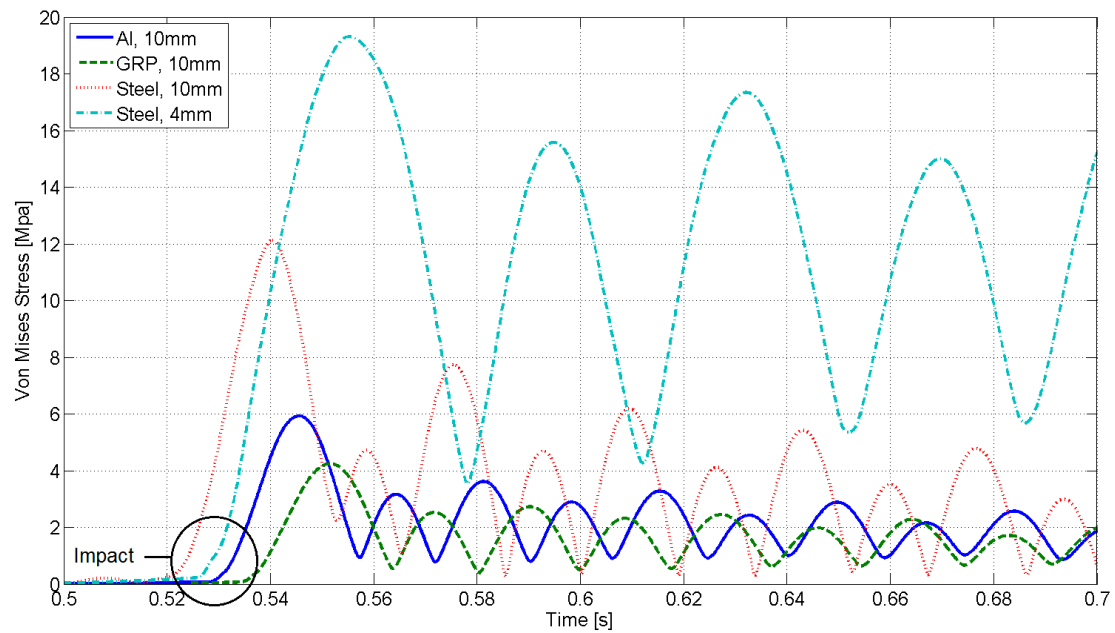


Figure 5.17: The von Mises stresses predicted in STAR for the four different elastic wedges.

CONCLUSIONS

The water entry of two and three-dimensional rigid and elastic wedges is studied using the CFD-software STAR-CCM+. In the two-dimensional study (Chapter 3), 2-D rigid wedges with constant vertical velocity and varying deadrise angles (4 to 81 degrees) are studied with respect to various slamming parameters presented by Zhao and Faltinsen (1992). The three-dimensional study is done for free-falling rigid and elastic wedges. Here, displacements, velocities, slamming pressures, accelerations, deflection and stresses are analyzed and compared to experimental data and theoretical models (comparisons are done only for the 3-D rigid wedge).

6.1 WATER ENTRY OF TWO-DIMENSIONAL WEDGES

For the case of 2-D rigid wedge water entry, it is found that STAR is able to solve the slamming pressures on the wedge bottom in a satisfactory manner. The solution is compared and verified with a similarity solution, an asymptotic solution and a boundary element method (BEM) presented in Zhao and Faltinsen (1992). In the comparison, good agreement is found with respect to the dimensionless slamming parameters $C_{p_{\max}}$, z_{\max}/Vt , $\Delta S_s/c$ and $F_3/(\rho V^3 t)$. The consistency in the results applies for all deadrise angles. It is noticed that the slamming pressures are strongly dependent on the deadrise angle; from 300 Pa for the 81° wedge to 275 000 Pa for the 4° wedge. In addition, it is seen that better resolution in grid size and time step is needed as the deadrise angle is decreased.

6.2 WATER ENTRY OF A THREE-DIMENSIONAL WEDGE

In the three-dimensional case, a 3-D wedge equal to that of the experimental study by Yettou et al. (2006) is modeled. Same wedge mass and initial drop height is applied, and recorded data are the wedge displacement, the wedge velocity and pressure on twelve pressure transducers. It is found that STAR predicts a lower impact velocity than what is found in the experimental study, and following too low pressures at the pressure transducers. This discrepancy is most likely caused by some added resistance in air (a phenomena not studied further). The difference is however moderate, and STAR is able to predict the displacement- and velocity-time history of the wedge in a satisfactory manner. A non-dimensional study also reveals too low values of the pressure coefficient C_p . An odd result as the coefficient takes into account the pressure/velocity-ratio.

It is important to note that the difference in pressure for the twelve transducers is also caused by the uncertainties connected to the experimental study. It is close to impossible to get an accurate reading of the pressure in an experimental set-up, and hence one cannot conclude that the pressures found by Yettou et al. (2006) are the ones that are correct.

It is noted that the reason for the discrepancy lies in the prediction of motion through air - not in the simulation of impact and motion in water. It should also be stressed that initial conditions in numerical calculations can be tricky when dealing with objects of large mass falling a relatively small distance (as is the case for the three-dimensional wedge).

Lastly, one should note that refinements in grid size and time step are not of great importance if only displacements and velocities are to be studied.

6.3 HYDROELASTIC IMPACT OF THREE-DIMENSIONAL WEDGES

A study on water entry of four different elastic wedges is performed to explore STAR's possibilities and limitations related to fluid-structure interaction (FSI). No verification or validation with existing theory or experimental data is performed. However, a qualitative assessment of the results with respect to the expected behavior of the wedges is carried out.

It is seen that the mass of the wedge influences the impact velocities and pressures as expected, i.e. a wedge with larger mass experiences larger velocity and hence larger impact pressure. The magnitude of decelerations on impact is found to increase with decreasing wedge mass; also as expected. Further, deflection of the wedge bottom is studied and here the results indicate larger deflections for lower values of the Young's Modulus and plate thickness (as expected). The Von Mises stresses are also recorded and found acceptable with respect to wedge deflection and Young's Modulus.

In the FSI study, some attention is directed to compressible versus incompressible water and air. Here, some peculiar results are noticed on wedge acceleration and impact pressures. This should be studied further according to section 6.4.

6.4 SUGGESTIONS FOR FURTHER STUDY

Regarding the verification for the use of STAR-CCM+ to predict performance of free-fall lifeboats, following improvements in studies for the three-dimensional rigid and elastic wedges are suggested:

For the 3-D rigid wedge:

- Investigate wedge acceleration and air drag in the free-falling phase.
- Experiment with the effect of different drop heights/impact velocities on slamming pressures and motion in water.

For the 3-D elastic wedge:

- Perform grid size and time step refinements and study the effect of this on the wedge's velocity, displacement, acceleration, slamming pressure, deflection and stresses.
- Investigate the effect of compressible and incompressible water in more detail by altering properties in the compressible model.
- Do a non-dimensional derivation of the pressure coefficient C_p and study this parameter as a function of wedge material (i.e. study the effect of wedge deflection on the pressure distribution).
- Obtain experimental, numerical and/or analytical studies on elastic wedge water entry and compare these results with predictions in STAR.

RECOMMENDATIONS FOR FURTHER WORK: LIFEBOAT WATER ENTRY

In the previous chapters studies on water impact of 2-D and 3-D wedges are performed to verify the CFD-software STAR-CCM+. The software is showing good ability to predict the wedge's displacements and velocities, the two most important parameters characterizing the lifeboats performance. As a conclusion, one can say that STAR is suitable to predict a free-fall lifeboat water entry.

As of today, several companies in the Norwegian maritime industry are using STAR to its full, and to a certain degree, basing some/much of their new designs on results obtained through simulations by the software¹. Free-fall lifeboats and their importance for the offshore industry as mentioned in Chapter 1 has made STAR an important tool when studying performance of different free-fall lifeboat designs.

As an aim, this chapter is to provide some recommendations for how STAR can be used when studying the free-fall lifeboat's water entry. The chapter will mainly focus on the procedure of the set-up of a lifeboat simulation. The procedure and comments are based on experience obtained through numerous conversations with Norschau (2012), Larsen (2012) and Bjelke-Mørch (2012). Details found in Mørch et al. (2008) CD-adapco (2011) are also included.

7.1 MODELING AND MESHING

As the STAR's CAD environment it limited to simple modeling, advanced third-party CAD software has to be applied when modeling the free-fall lifeboat. In such cases, SolidWorks or Catia are good tools which offer the option to export the geometries in different formats importable by STAR. A starting point for the meshing process is therefore to import some kind of surface data. The surface data can be in the form of either a geometry or a mesh description. During this process, the user can specify whether to import the data as regions or to import the data as parts. The resulting imported surface can be checked for errors and fixed by the *surface repair tool* if required.

When dealing with third-party modeling, communication between the STAR user and the CAD user is crucial to obtain a good model. Often, when the 3-D model is imported in STAR, mismatch in geometry surface occur. For instance, this can be surface mismatches or intersecting parts. This forces the user of STAR to repair the

¹DNV, Bergen Group, STX OSV, Norsafe and Schat-Harding are some of the companies which bases some/much of their new design on STAR-CCM+.

surface such that the geometry consists of **one closed surface**. If the guidelines for the design are not made perfectly clear between the modeler and the analyst, the design of the model might be changed during this repair process. In addition, working with the surface repair tool may consume a considerable amount of hours, causing frustration for both the STAR analyst and the client buying the service.

When the surface import is completed, meshing of the free-fall lifeboat and air/fluid domain is performed. In STAR, three different approaches are commonly used when studying launching of lifeboats:

- If there are no waves present and the fluid domain is infinite, a moving grid as utilized and explained in Chapter 4 can be applied. This type of grid requires adaption of boundary conditions in each time step since the boundary positions changes, and the grid needs to be fine in a larger region in order to capture the free surface properly.
- In some applications where only two linear and one rotational motion is activated (which is usually the case when studying free-fall lifeboat's water impact), the solution domain can be split into two parts with a cylindrical sliding interface. Here, the lifeboat is located inside a cylindrical region, which rotates with it, while the rest of the grid is performing only the translation motions.
- A third possibility is to use overlapping or "overset" grids, where a background grid is adapted to the free surface and outside boundaries (like sea bed, oil platform or marine vessel), while the overlapping grid is attached to the lifeboat and moves with it without deformation. In the case for an overlapping grid, the grid quality is easier to control and the grid motion is easier to handle. However, a more complex solution method is required to account for coupling of the background and overlapping grid solutions.

When setting up the chosen mesh model, one must use local grid refinements to adequately account for effects of design details at bow, stern and canopy. Refinements should also be applied at regions where large curvature is encountered. As done in the studies in the previous chapters, anisotropic refinements should be performed in selected directions, especially at the free surface where a vertical (and horizontal, to some extent) refinement is needed to obtain an adequate resolution of the generated waves.

7.2 PHYSICAL MODELS AND INITIAL CONDITIONS

The regions with their respective boundaries are specified as velocity inlet, pressure outlet, symmetry plane and wall condition in much the same way as explained in all of the previous chapters. Note that for a free-fall lifeboat a symmetry condition is often applied along the center line (only half the lifeboat is modeled).

When the regions are set, a physics continuum must be defined. For a free-fall lifeboat analysis, the simulation will model the behavior of two fluids (water and air) within the same continuum. This is done by applying the Volume of Fluid (VOF) model (explained in section 2.2, Chapter 2) and activating the Eulerian Multiphase model. The physics models which are to be selected include:

- Three-dimensional
- Implicit unsteady

- Multiphase Mixture
- Volume of Fluid (VOF)
- Laminar
- Gravity

It's recommended to tick the "Auto-select recommended models" box. In this way STAR will choose the additional models that are suitable together with the already chosen models. Notice that for the lifeboat simulation a laminar flow model is applied. This assumption is acceptable as only the simulation of water entry and impact forces are of interest². Simulation of lifeboat cases over a longer distance would require a turbulence model.

After choosing the different physics models, initial conditions for the simulation need to be set. When a lifeboat is launched from a ramp it undergoes three stages before it hits the water: a translational acceleration down the ramp, an angular acceleration as the COG passes the edge of the ramp, and lastly, a downward acceleration before the lifeboat hits the water. Due to its complexity and costs in computational time, free fall lifeboat drops are rarely simulated from its initial position on a ramp located at a host structure. An often used approach is therefore to start the coupled simulation of fluid flow and flow-induced motion at the last and third stage, i.e. when the lifeboat is in the free falling phase. By using the 6-DOF *DFBI Rotation and Translation* model, the initial conditions for this phase are set. These conditions include position of COG, together with horizontal, vertical and angular velocities. Each of the initial values can be obtained by geometrical considerations and the various equations of rigid motion (details are found in DNV-OS-E (2010)). If the simulation is to include wind, one must adjust for the effect of wind on the lifeboat's motion in air. A kinematic model for rigid body motions which also includes the effect of head wind has been developed by Mørch et al. (2008). The method applies Runge-Kutta of 3rd order to solve the velocities and the trajectory of the moving lifeboat.

7.3 SOLVER PARAMETERS AND SETTINGS

When the needed conditions are applied (both initial and boundary) the solver settings must be set such to obtain a stable and converging solution. As the simulation is transient, one must specify the time step, the maximum number of inner iterations that is permitted in each time step, and the overall physical time for which a solution should be obtained.

The time step which is to be selected is dependent on the phenomena one wishes to study. As seen in Chapter 5, a time step of the order E^{-4} is sufficient when studying velocities and displacements. However, if slamming pressures are of interest, one must reduce the time step to the order of E^{-5} , ref. Chapter 4. As the two most important parameters when deciding upon the lifeboat's design are the velocities and displacement, a time step at the order E^{-4} is therefore recommended. However, as stated in section 2.1 in Chapter 2, the time step must also be chosen in accordance to the grid size such that the Courant-Friedrichs-Levi condition (2.1) holds, i.e. $CFL < 1$. If accurate wave propagation is to be simulated one must choose a 2nd order time discretization in the *Implicit Unsteady* solver settings.

²A study on laminar versus turbulent flow model for wedge water entry are seen in both Chapter 3 and Chapter 4.

A numerical solution is achieved through iterations, and the rate of which the result improves from one iteration to another is important. To choose the appropriate number of iterations in the solver one must study the residuals at simulation start-up. For a free fall lifeboat simulation it is desirable that the drop in residuals for the relevant equations are of the order E^2 . However, convergence can also be obtained at E^1 . Again, this can be determined by studying the solution. As a rule of thumb, number of iterations for a lifeboat simulation is set from 10-15.

7.4 MISCELLANEOUS

In STAR, one is able to prepare the post-processing before starting the simulation. This has the benefit that one can study scenes and plots as the simulation is running, and if necessary, make changes to grid size, time step and/or numerical parameters (etc.).

As mentioned, parameters as displacement and velocity are important when studying lifeboat performance. This implies that when setting up a lifeboat simulation in STAR, one should prepare reports, monitors, plots and scenes for these scalars. When dealing with different lifeboat designs, one study would be to compare the horizontal displacement and velocity, at say, midway through the submerged phase. This will give an indication on which lifeboat has the best change to move away from the host structure, should an accident occur.

Another aspect when studying free fall lifeboats are the accelerations felt by the occupants at water impact. There exist regulations on the magnitude of these accelerations, known as the CAR-value³, and one must make sure that this value is within a reasonable limit. Accelerations are largest at the lifeboats bow and stern, and hence reports, monitors and plots should be created at these locations prior to simulation start.

Details on how the different design parameters influences a free fall lifeboat's performance are found in Johannessen (2011). It is strongly recommended that the reader study this thesis before a further study on the use of STAR to predict performance of lifeboat designs is initiated.

³Details concerning the CAR-value is found in Johannessen (2011).

References

- Aarsnes, J. M. (2011). *Lecture Notes: Hydroelasticity*, Norwegian Institute of Science and Technology, Department of Marine Technology, 2011.
- Armand, J. and Cointe, R. (1986). *Hydrodynamic impact analysis of a cylinder*, In *Proc. Fifth Int Offshore Mech. and Arctic Engng Symp., Tokyo, Japan*, Vol. 1, pp. 609-634. ASME, 1986.
- Bjelke-Mørch, H. (2012). *Conversations with Hans Jørgen Bjelke-Mørch*, CFD Marin, Spring 2012.
- CD-adapco (2011). *USER GUIDE STAR-CCM+ Version 7.02.008*, CD-adapco, 2011.
- CD-adapco (2012). *The Virtual Wave Basin*, <http://www.cd-adapco.com/events/workshops/7014000000MVJ7AAG>. [Online; accessed May 3rd - 2012].
- Cointe, R. (1991). *Free surface flows close to a surface-piercing body*, In *Mathematical Approaches in Hydrodynamics* (ed. T. Miloh), pp 319-334. Soc. Ind. Appl. Maths, Philadelphia, USA, 1991.
- Day, D. A. (2010). *NM422/NM402/NM915 - Theory & and practice of Marine CFD*, The University of Strathclyde, 2010.
- Dejhalla, R. and Prpic-Orsic, J. (2006). *A review of the State-of-the-Art in Marine Hydrodynamics*, University of Rijeka, Department of Naval Architecture and Ocean Engineering, 2006.
- Demirdzic, I. and Muzaferija, S. (1995). *Numerical Method for Coupled Fluid Flow, Heat Transfer and Stress Analysis using Unstructured Moving Mesh with Cells of Arbitrary Topology*, In *Comput. Methods Appl. Mech. Engrg.*, 125:235-255, 1995.
- DNV-OS-E (2010). *Design of free fall lifeboats*, Offshore Standard - DNV-OS-E406, DNV, 2010.
- Dobrovol'skaya, Z. (1969). *On some problems of similarity flow of fluid with a free surface*, In *J. Fluid Mech.* 36, pp 805-829, 1969.
- Faltinsen, O. M. (2012). *Conversations with Odd Magnus Faltinsen*, Professor at the Norwegian Institute of Science and Technology, Department of Marine Technology, Spring 2012.
- Ferziger, J. and Peric, M. (2003). *Computational Methods for Fluid Dynamics*, Springer, Berlin, 3rd edition, 2003.
- Gorski, J. (2001). *Present state of numerical ship hydrodynamics and validation experiments*, 20th International Conference on Offshore Mechanics and Arctic Engineering, June 3-8, Rio de Janeiro. OMAE2001/OFT-1350, 2001 .

- Howison, S. D., Ockendon, J. R. and Wilson, S. K. (1991). *Incompressible water-entry problems at small deadrise angles*, In *J. Fluid Mech.* 222, pp 215-230, 1991.
- Hughes, O. (1972). *Solution of the wedge entry problem by numerical conformal mapping*, In *J. Fluid Mech.* 56, pp 173-192, 1972.
- Johannessen, S. R. (2011). *Hydrodynamic loads and response to free fall lifeboats*, Project Thesis, Norwegian University of Science and Technology, Department of Marine Technology, 2011.
- Kopperstad, A. (2011). *Hydrodynamiske beregninger med bølgeoverflate*, NTNU - Department of Marine Technology, 2011.
- Korobkin, A. and Pokhnachov, V. (1988). *Initial stage of water impact*, Annual Review of Fluid Mechanics 20, 1988 .
- Larsen, T. (2012). Conversations with Thomas Larsen, CFD Marin, Spring 2012.
- Luo, H., Wang, H. and Soares, C. (2011). *Comparative study of hydroelastic impact for one free-drop wedge with stiffened panels by experimental and explicit finite methods*, Proceedings of the ASME 2011 30th International Conference on Ocean, Offshore and Arctic Engineering, OMAE2011, June 19-24, Rotterdam, The Netherlands, 2011.
- Maki, K. J., Lee, D., Troesch, A. W. and Vlahopoulos, N. (2010). *Hydroelastic impact of a wedge-shaped body*, Department of Naval Architecture and Marine Engineering, University of Michigan, 2600 Draper Dr., Ann Arbor, MI 48109-2145, United States, 2010.
- Mei, X. (1998). *On the water impact of arbitrary two-dimensional sections*, Master's Thesis, Department of Ocean Engineering, MIT, Cambridge, MA, 1998.
- Mørch, H. J., Enger, S., Peric, M. and Schreck, E. (2008). *Simulation of lifeboat launching under storm conditions*, 6th International Conference on CFD in Oil & Gas, Metallurgical and Process Industries, SINTEF/NTNU, Trondheim, Norway, 10-12 June, 2008.
- Mueller, A. (2012). Conversations with Alan Mueller, CD-adapco, Spring 2012.
- Muzaferija, S. and Peric, M. (1999). *Computation of Free Surface Flows Using Interface-Tracking and Interface-Capturing Methods*, In *Nonlinear Water Wave Interaction*. WIT Press, Southampton, 1999.
- Norschau, K. (2012). Conversations with Karl Marius Norschau, Meyer Norschau Design, Spring 2012.
- OLF (2010). *About the lifeboat project*, <http://www.olf.no/en/Activities/HSE-and-operation>. [Online; accessed 10-September-2011].
- Panciroli, R., Abrate, S., Minak, G. and Zucchelli, A. (2011). *Hydroelasticity in water-entry problems: Comparison between experimental and SPH results*, Università di Bologna, Mechanical Engineering Department DIEM, Viale del Risorgimento 2, 40136 Bologna, Italy, 2011.
- Payne, P. (1988). *Design of high-speed boats*, Vol. 1: Planing. Fishergate Inc, 1988.
- Peric, M. (2012). Conversations with Milovan Peric, CD-adapco, Spring 2012.

-
- Pettersen, B. (2011). Lectures given in the course TMR 15 - Numerical Methods by Bjørnar Pettersen, Professor at the Norwegian Institute of Science and Technology, Department of Marine Technology, Hydrodynamics, Fall 2011.
- Ransau, S. (2011). *Lecture notes for the course: Numerical Methods in Marine Hydrodynamics*, Norwegian University of Science and Technology, Department of Marine Technology, 2011.
- Von Karman, T. (1929). *The impact on seaplane floats during landing*, Technical Notes, National Advisory Committee for Aeronautics, 1929.
- Voronkov, O. (2012). Conversations with Oleg Voronkov, CD-adapco, Spring 2012.
- Wagner, H. (1932). *Über stoss- und Gleitvorgänge and der Oberfläche von Flüssigkeiten*, In *Z. Angew. Math. Mech.* 12 (4), pp 192-235, 1932.
- Wagner, H. (1936). *Phenomena associated with impacts and sliding on liquid surfaces*, Translation of *Über stoss- und Gleitvorgänge and der Oberfläche von Flüssigkeiten*, Zeitschrift Für Angewandte Mathematik Und Mechanik, NACA Library, Langley Aeronautical Laboratory, 1936.
- Watanabe, T. (1986). *Analytical expression of hydrodynamic impact pressure by matched asymptotic expansion technique*, In *Trans. West-Japan Soc. Naval Arch.*, No. 71, pp 77-85, 1986.
- Werenskiold, P. (2011). Conversations with Per Werenskiold, Naval Architect MSc. Fall.
- Xing-Kaeding, Y. (2006). *Unified approach to ship sea-keeping and maneuvering by a RANSE Method*, Dissertation, TU Hamburg-Harburg, 2006.
- Yettou, E.-M., Desrochers, A. and Champoux, Y. (2006). *Experimental study on the water impact of a symmetrical wedge*, In *Fluid Dynamic Research* 38, pp 47-66, 2006.
- Zhao, R. and Faltinsen, O. (1992). *Water entry of two-dimensional bodies*, In *J. Fluid Mech.* (1993), vol. 246, pp 593-612, 1992.
- Zhao, R., Faltinsen, O. and Aarsnes, J. (1996). *Water entry of arbitrary two-dimensional sections with and without flow separation*, In *Proceedings of the 21st Symposium on Naval Hydrodynamics*, Trondheim, Norway. National Academy Press, Washington DC, 1996.